



2010

TRANSITIONAL FLOW PREDICTION OF A COMPRESSOR AIRFOIL

Vivek Hariharan

University of Kentucky, vivek.hariharan@uky.edu

[Click here to let us know how access to this document benefits you.](#)

Recommended Citation

Hariharan, Vivek, "TRANSITIONAL FLOW PREDICTION OF A COMPRESSOR AIRFOIL" (2010). *University of Kentucky Master's Theses*. 44.

https://uknowledge.uky.edu/gradschool_theses/44

This Thesis is brought to you for free and open access by the Graduate School at UKnowledge. It has been accepted for inclusion in University of Kentucky Master's Theses by an authorized administrator of UKnowledge. For more information, please contact UKnowledge@sv.uky.edu.

ABSTRACT OF THESIS

TRANSITIONAL FLOW PREDICTION OF A COMPRESSOR AIRFOIL

The steady flow aerodynamics of a cascade of compressor airfoils is computed using a two-dimensional thin layer Navier-Stokes flow solver. The Dhawan and Narasimha transition model and Mayle's transition length model were implemented in this flow solver so that transition from laminar to turbulent flow could be included in the computations. A method to speed up the convergence of the fully turbulent calculations has been introduced. In addition, the effect of turbulence production formulations and including streamline curvature correction in the Spalart-Allmaras turbulence model on the transition calculations is studied. These transitional calculations are correlated with the low and high incidence angle experimental data from the NASA-GRC Transonic Flutter Cascade. Including the transitional flow showed a trendwise improvement in the correlation of the computational predictions with the pressure distribution experimental data at the high incidence angle condition where a large separation bubble existed in the leading edge region of the suction surface.

KEYWORDS: CFD, Turbomachinery, Flow Separation, Transition from Laminar to Turbulent Flow, Intermittency.

Vivek Hariharan

22nd June, 2010

TRANSITIONAL FLOW PREDICTION
OF A COMPRESSOR AIRFOIL

By

Vivek Hariharan

Dr. Vincent R. Capece

Director of Thesis

Dr. James M. McDonough

Director of Graduate Studies

22nd June, 2010

RULES FOR THE USE OF THESES

Unpublished theses submitted for the Master's degree and deposited in the University of Kentucky Library are as a rule open for inspection, but are to be used only with due regard to the rights of the authors. Bibliographical references may be noted, but quotations or summaries of parts may be published only with the permission of the author, and with the usual scholarly acknowledgments.

Extensive copying or publication of the thesis in whole or in part also requires the consent of the Dean of the Graduate School of the University of Kentucky.

A library that borrows this thesis for use by its patrons is expected to secure the signature of each user.

Name

Date

THESIS

Vivek Hariharan

The Graduate School
University of Kentucky
2010

TRANSITIONAL FLOW PREDICTION
OF A COMPRESSOR AIRFOIL

THESIS

A thesis submitted in partial fulfillment of the
requirements for the degree of Master of Science in
Mechanical Engineering in the College of Engineering
at the University of Kentucky

By

Vivek Hariharan

Lexington, Kentucky

Director: Dr. Vincent R. Capece, Associate Professor of Mechanical Engineering

Paducah, Kentucky

2010

Copyright © Vivek Hariharan 2010

This work is dedicated to my Amma (Mother) and Appa (Father) from whom I've learnt a lot about life and who taught me to be patient and work hard to stand on my own feet.

This work will always remind me of the strength and courage they've imparted to me.

ACKNOWLEDGEMENTS

I would like to take this opportunity to express my gratitude towards my advisor Dr. Vincent R. Capece for his time and support in carrying out this research project. This thesis could not have been made possible without his tremendous help and valuable comments.

In addition, I would like to thank Dr. Kozo Saito and Dr. Tingwen Wu for serving as members of my defense committee. I would also like to thank all my teachers for their support and guidance.

I would like to gratefully acknowledge the support of Qian Zhang of our research group in helping me in the initial phase to start with this research project and also for his support from time to time.

I would like to thank all my family members, especially Susheela Chitti, Usha Chitti, Murali Chitappa and Brinda Akka for their continued support, and without whom this Master's degree could not have been pursued. I would like to express my sincere gratitude towards them for having faith and confidence in me as I began my journey as a graduate student.

I also would like to thank my friends in India and Lexington, KY for their encouragement and support during my Master's work. Firstly, I would like to express my sincere gratefulness towards my close friends Seshadri and Sripathi for their ever-lasting moral support, kindness and words of wisdom. I would also like to thank Viji for having been on my side, for her encouraging words, for having had complete faith and trust in me, and for her care and support in times of need. I would also like to thank Anusha for

her support in my times of need. I would also like to thank Spandana for her encouraging words while I was writing my thesis. I would also like to thank Dharmendra and Jhon for their support and care during my thesis writing stage. I would also like to thank Tathagata and Devi for having been with me and being supportive until the beginning of my thesis writing stage. I would also like to extend my thankfulness towards Ms. Verronda for her kindness, care and support. In the end, I would like to express my sincere thanks to Gurdish for being extremely helpful and supportive, and for having given me company during my thesis writing stage. Though, this thesis has been the result of my hard work and dedication, it could not have been made possible without the support of all my friends.

Finally, I would like to express my deepest love and gratitude towards my parents, who inspired and instilled in me the confidence and courage to succeed in life. This thesis could not have been possible without their blessings. They both have been a tremendous source of knowledge and a source of strength in every dimension of life I have seen.

TABLE OF CONTENTS

Acknowledgements.....	iii
List of Tables.....	viii
List of Figures.....	ix
List of Symbols.....	xvi
List of Files.....	xxi
Chapter One: Introduction.....	1
Background.....	1
Literature Review.....	4
Objectives.....	6
Chapter Two: Geometry and Grid Generation.....	8
Cascade Geometry.....	8
Airfoil Geometry.....	9
Grid Generation.....	10
Different Types of Grids.....	11
Traditional H-grids and Sheared H-grids.....	13
C-grids.....	15
O-grids.....	16
Grids for Flat Plate Studies.....	17
Grids for NASA-PW Airfoil.....	18
Chapter Three: Turbulence and Transition Models.....	21
Turbulence.....	21
Baldwin-Lomax Algebraic Turbulence Model.....	21
Spalart-Allmaras One-Equation Turbulence Model.....	24
Boundary and Initial Conditions for the Spalart-Allmaras Turbulence Model.....	28
Inlet Turbulent Viscosity and Initial Condition.....	29
Streamline Curvature Correction.....	30

Transition from Laminar to Turbulent Flow.....	31
Mayle Transition Length Model.....	31
Dhawan and Narasimha Transition Model.....	33
 Chapter Four: Computational Model and Data-Theory Correlation.....	 35
NPHASE.....	35
Interaction of Transition Model with Flow Solver.....	36
Data-Theory Correlation.....	37
Flat Plate.....	38
NASA-PW Airfoil.....	41
Computational Procedures.....	41
 Chapter Five: Results.....	 42
Flat Plate.....	42
Laminar Flow.....	43
Turbulent Flow.....	47
Inlet Turbulent Viscosity and Initial Condition Study.....	52
Production Term Formulation Study in the Spalart-Allmaras Model.....	54
Streamline Curvature Correction Study.....	57
Transition.....	60
NASA-PW.....	64
Low Incidence Angle Condition.....	65
Fully Turbulent Flow.....	65
Baldwin-Lomax and Spalart-Allmaras Model.....	69
Inlet Turbulent Viscosity Study.....	73
Streamline Curvature Correction Study.....	76
Transition.....	81
Inlet Turbulent Viscosity Study.....	98
High Incidence Angle Condition.....	105
Fully Turbulent Flow.....	105
Baldwin-Lomax and Spalart-Allmaras Model.....	110
Inlet Turbulent Viscosity Study.....	114
Production Term Formulation Study in the Spalart-Allmaras Model.....	117
Streamline Curvature Correction Study.....	120

Transition.....	123
Inlet Turbulent Viscosity Study.....	133
Production Term Formulation Study in the Spalart-Allmaras Model.....	136
Streamline Curvature Correction Study.....	140
A Study of Inlet Turbulent Viscosity with Streamline Curvature Correction.....	146
Chapter Six: Summary and Conclusions.....	151
Summary.....	151
Conclusions.....	152
Future Work.....	157
Appendices	
Appendix A: Turbulent Flat Plate Experimental Data.....	158
Appendix B: Turbulent Flat Plate Simulations at a Higher Mach Number.....	160
References.....	163
Vita.....	166

LIST OF TABLES

Table 2.1	Airfoil and Cascade parameters (Buffum et al., 1998).....	9
Table 2.2	Flat plate airfoil grids.....	17
Table 2.3	NASA-PW airfoil grids.....	18
Table 3.1	Baldwin-Lomax turbulence model constants.....	23
Table 3.2	Spalart-Allmaras turbulence model constants.....	26
Table 5.1	Transitional flow parameters for the NASA-PW airfoil at the low incidence angle condition.....	90
Table 5.2	Transitional flow parameters for the NASA-PW airfoil at the low incidence angle condition for different values of inlet turbulent viscosity.....	100
Table 5.3	Transitional flow parameters for the NASA-PW airfoil at the high incidence angle condition.....	131
Table 5.4	Transitional flow parameters for the NASA-PW airfoil at the high incidence angle condition for different values of inlet turbulent viscosity.....	134
Table 5.5	Transitional flow parameters for the NASA-PW airfoil at the high incidence angle condition for different production term formulations in the SA model.....	138
Table 5.6	Transitional flow parameters for the NASA-PW airfoil at the high incidence angle condition with and without streamline curvature correction.....	142
Table 5.7	Transitional flow parameters for the NASA-PW airfoil at the high incidence angle condition for different values of inlet turbulent viscosity with streamline curvature correction.....	148

LIST OF FIGURES

Figure 2.1	Airfoil and cascade geometry.....	9
Figure 2.2	Chordwise distribution of y^+ over the NASA-PW airfoil surface (193 x 101 Grid).....	10
Figure 2.3	Example of a 3-D structured grid for an extruded NACA-0012 airfoil.....	12
Figure 2.4	Example of a 3-D unstructured grid for an extruded NACA-0012 airfoil.	13
Figure 2.5	An example of H-grid topology over a NACA-0012 airfoil.....	14
Figure 2.6	C-grid around a NACA-0012 airfoil.....	15
Figure 2.7	Example of O-grid around a NACA-0012 airfoil.....	16
Figure 2.8	Computational domain for the flat plate airfoil (238 x 164 Grid).....	18
Figure 2.9	Computational domain for the NASA-PW airfoil (193 x 101 Grid).....	19
Figure 2.10	Airfoil surface grid topology for the NASA-PW airfoil (193 x 101 Grid).	19
Figure 2.11	Grid topology in the leading edge region of the NASA-PW airfoil (193 x 101 Grid).....	20
Figure 2.12	Grid topology in the trailing edge region of the NASA-PW airfoil (193 x 101 Grid).....	20
Figure 3.1	Schematic diagram in a transitional flow with a separation bubble (Mayle, 1991).....	32
Figure 4.1	Example of the variation of the intermittency factor in the transition region over the suction surface of the NASA-PW airfoil (193 x 101 Grid).....	37
Figure 5.1	Example of flat plate lift coefficient convergence history for laminar flow.....	44
Figure 5.2	Example of the absolute value of the average density residual convergence history for laminar flow over a flat plate airfoil.....	45
Figure 5.3	Flat plate skin-friction coefficient for laminar flow.....	47
Figure 5.4	Example of flat plate lift coefficient convergence history for fully turbulent flow.....	48
Figure 5.5	Example of the absolute value of the average density residual convergence history for fully turbulent flow over a flat plate airfoil.....	49
Figure 5.6	Flat plate skin-friction coefficient for fully turbulent flow.....	50
Figure 5.7	Flat plate velocity distribution for fully turbulent flow.....	52

Figure 5.8	Flat plate skin-friction coefficient for fully turbulent flow with different values of the inlet turbulent viscosity and initial conditions.....	53
Figure 5.9	Flat plate velocity distribution for fully turbulent flow with different inlet turbulent viscosity values and initial conditions.....	54
Figure 5.10	Flat plate skin-friction coefficient for fully turbulent flow using different production term formulations in the SA model.....	56
Figure 5.11	Flat plate velocity distribution for fully turbulent flow using different production term formulations in the SA model.....	57
Figure 5.12	Flat plate skin-friction coefficient for fully turbulent flow with and without the streamline curvature correction.....	59
Figure 5.13	Flat plate velocity distribution for fully turbulent flow with and without the streamline curvature correction.....	60
Figure 5.14	Example of flat plate lift coefficient convergence history for turbulent and transition flow.....	61
Figure 5.15	Example of the absolute value of the average density residual convergence history for turbulent and transition flow over a flat plate airfoil.....	62
Figure 5.16	Flat plate skin-friction coefficient for transition from laminar to turbulent flow along the suction surface.....	64
Figure 5.17	Example of NASA-PW airfoil lift coefficient convergence history at the low incidence angle condition for fully turbulent flow.....	66
Figure 5.18	Example of the absolute value of the average density residual convergence history for the NASA-PW airfoil at the low incidence angle condition for fully turbulent flow.....	67
Figure 5.19	Surface pressure coefficient distribution for the NASA-PW airfoil at the low incidence angle condition for fully turbulent flow.....	68
Figure 5.20	Leading edge surface pressure coefficient distribution for the NASA-PW airfoil at the low incidence angle condition for fully turbulent flow.....	69
Figure 5.21	NASA-PW airfoil lift coefficient convergence history at the low incidence angle condition for fully turbulent flow with the BL model providing the initial conditions for the SA model.....	71
Figure 5.22	Surface pressure coefficient distribution for the NASA-PW airfoil at the low incidence angle condition for fully turbulent flow with the BL model providing the initial conditions for the SA model.....	72
Figure 5.23	Leading edge surface pressure coefficient distribution for the NASA-PW airfoil at the low incidence angle condition for fully turbulent flow with the BL model providing the initial conditions for the SA model.....	73

Figure 5.24	Surface pressure coefficient distribution for the NASA-PW airfoil at the low incidence angle condition for fully turbulent flow with different inlet turbulent viscosity values.....	75
Figure 5.25	Leading edge surface pressure coefficient distribution for the NASA-PW airfoil at the low incidence angle condition for fully turbulent flow with different inlet turbulent viscosity values.....	76
Figure 5.26	Surface pressure coefficient distribution for the NASA-PW airfoil at the low incidence angle condition for fully turbulent flow with and without the streamline curvature correction.....	78
Figure 5.27	Leading edge surface pressure coefficient distribution for the NASA-PW airfoil at the low incidence angle condition for fully turbulent flow with and without the streamline curvature correction.....	79
Figure 5.28	Streamlines in the leading edge region of the NASA-PW airfoil (193 x 101 Grid) at the low incidence angle condition for fully turbulent flow (a) without streamline curvature correction, and (b) with streamline curvature correction.....	80
Figure 5.29	Example of NASA-PW airfoil lift coefficient convergence history at the low incidence angle condition for turbulent and transitional flow.....	82
Figure 5.30	Example of the absolute value of the average density residual convergence history for the NASA-PW airfoil at the low incidence angle condition for turbulent and transitional flow.....	83
Figure 5.31	Contours of ρu for the NASA-PW airfoil (193 x 101 Grid) at the low incidence angle condition for transitional flow using fixed transition onset with $x_{LT} = 0.03$	85
Figure 5.32	Contours of ρu in the leading edge region of the NASA-PW airfoil (193 x 101 Grid) at the low incidence angle condition for transitional flow using fixed transition onset with $x_{LT} = 0.03$	85
Figure 5.33	Velocity vectors with ρu contours in the leading edge region of the NASA-PW airfoil (193 x 101 Grid) at the low incidence angle condition for (a) fully turbulent flow, and (b) transitional flow using fixed transition onset with $x_{LT} = 0.03$	86
Figure 5.34	Surface pressure coefficient distribution for the NASA-PW airfoil at the low incidence angle condition for transitional flow using fixed transition onset with $x_{LT} = 0.01$	91
Figure 5.35	Leading edge surface pressure coefficient distribution for the NASA-PW airfoil at the low incidence angle condition for transitional flow using fixed transition onset with $x_{LT} = 0.01$	92

Figure 5.36	Surface pressure coefficient distribution for the NASA-PW airfoil at the low incidence angle condition for transitional flow using fixed transition onset with $x_{LT} = 0.02$	93
Figure 5.37	Leading edge surface pressure coefficient distribution for the NASA-PW airfoil at the low incidence angle condition for transitional flow using fixed transition onset with $x_{LT} = 0.02$	94
Figure 5.38	Surface pressure coefficient distribution for the NASA-PW airfoil at the low incidence angle condition for transitional flow using fixed transition onset with $x_{LT} = 0.03$	95
Figure 5.39	Leading edge surface pressure coefficient distribution for the NASA-PW airfoil at the low incidence angle condition for transitional flow using fixed transition onset with $x_{LT} = 0.03$	96
Figure 5.40	Surface pressure coefficient distribution for the NASA-PW airfoil at the low incidence angle condition for transitional flow using Mayle's transition length model.....	97
Figure 5.41	Leading edge surface pressure coefficient distribution for the NASA-PW airfoil at the low incidence angle condition for transitional flow using Mayle's transition length model.....	98
Figure 5.42	Surface pressure coefficient distribution for the NASA-PW airfoil at the low incidence angle condition for transitional flow using fixed transition onset with $x_{LT} = 0.01$ for different inlet turbulent viscosity values.....	101
Figure 5.43	Leading edge surface pressure coefficient distribution for the NASA-PW airfoil at the low incidence angle condition for transitional flow using fixed transition onset with $x_{LT} = 0.01$ for different inlet turbulent viscosity values.....	102
Figure 5.44	Velocity vectors with ρu contours in the leading edge region of the NASA-PW airfoil (193 x 101 Grid) at the low incidence angle condition for the inlet turbulent viscosity value of 0.009 for (a) fully turbulent flow, and (b) transitional flow using fixed transition onset with $x_{LT} = 0.01$	103
Figure 5.45	Velocity vectors with ρu contours in the leading edge region of the NASA-PW airfoil (193 x 101 Grid) at the low incidence angle condition for the inlet turbulent viscosity value of 10.0 for (a) fully turbulent flow, and (b) transitional flow using fixed transition onset with $x_{LT} = 0.01$	104
Figure 5.46	Example of NASA-PW airfoil lift coefficient convergence history at the high incidence angle condition for fully turbulent flow.....	106
Figure 5.47	Example of the absolute value of the average density residual convergence history for the NASA-PW airfoil at the high incidence angle condition for fully turbulent flow.....	107

Figure 5.48	Surface pressure coefficient distribution for the NASA-PW airfoil at the high incidence angle condition for fully turbulent flow.....	109
Figure 5.49	Leading edge surface pressure coefficient distribution for the NASA-PW airfoil at the high incidence angle condition for fully turbulent flow.....	110
Figure 5.50	NASA-PW airfoil lift coefficient convergence history at the high incidence angle condition for fully turbulent flow with the BL model providing the initial conditions for the SA model.....	112
Figure 5.51	Surface pressure coefficient distribution for the NASA-PW airfoil at the high incidence angle condition for fully turbulent flow with the BL model providing the initial conditions for the SA model.....	113
Figure 5.52	Leading edge surface pressure coefficient distribution for the NASA-PW airfoil at the high incidence angle condition for fully turbulent flow with the BL model providing the initial conditions for the SA model.....	114
Figure 5.53	Surface pressure coefficient distribution for the NASA-PW airfoil at the high incidence angle condition for fully turbulent flow with different inlet turbulent viscosities.....	116
Figure 5.54	Leading edge surface pressure coefficient distribution for the NASA-PW airfoil at the high incidence angle condition for fully turbulent flow with different inlet turbulent viscosities.....	117
Figure 5.55	Surface pressure coefficient distribution for the NASA-PW airfoil at the high incidence angle condition for fully turbulent flow using different production term formulations in the SA model.....	119
Figure 5.56	Leading edge surface pressure coefficient distribution for the NASA-PW airfoil at the high incidence angle condition for fully turbulent flow using different production term formulations in the SA model.....	120
Figure 5.57	Surface pressure coefficient distribution for the NASA-PW airfoil at the high incidence angle condition for fully turbulent flow with and without streamline curvature correction.....	122
Figure 5.58	Leading edge surface pressure coefficient distribution for the NASA-PW airfoil at the high incidence angle condition for fully turbulent flow with and without streamline curvature correction.....	123
Figure 5.59	Example of NASA-PW airfoil lift coefficient convergence history at the high incidence angle condition for turbulent flow with transition.....	124
Figure 5.60	Example of the absolute value of the average density residual convergence history for the NASA-PW airfoil at the high incidence angle condition for turbulent flow with transition.....	125

Figure 5.61	Example of ρu contours for the NASA-PW airfoil (193 x 101 Grid) at the high incidence angle condition for transitional flow using fixed transition onset with $x_{LT} = 0.08$	127
Figure 5.62	Example of ρu contours in the leading edge region of the NASA-PW airfoil (193 x 101 Grid) at the high incidence angle condition for transitional flow using fixed transition onset with $x_{LT} = 0.08$	127
Figure 5.63	Example of velocity vectors with ρu contours in the leading edge region of the NASA-PW airfoil (193 x 101 Grid) at the high incidence angle condition for (a) fully turbulent flow, and (b) transitional flow using fixed transition onset with $x_{LT} = 0.08$	128
Figure 5.64	Surface pressure coefficient distribution for the NASA-PW airfoil at the high incidence angle condition for turbulent flow and transitional flow with fixed transition onset.....	132
Figure 5.65	Leading edge surface pressure coefficient distribution for the NASA-PW airfoil at the high incidence angle condition for turbulent flow and transitional flow with fixed transition onset.....	133
Figure 5.66	Surface pressure coefficient distribution for the NASA-PW airfoil at the high incidence angle condition for turbulent flow and transitional flow with fixed transition onset for different inlet turbulent viscosities.....	135
Figure 5.67	Leading edge surface pressure coefficient distribution for the NASA-PW airfoil at the high incidence angle condition for turbulent flow and transitional flow with fixed transition onset for different inlet turbulent viscosities.....	136
Figure 5.68	Surface pressure coefficient distribution for the NASA-PW airfoil at the high incidence angle condition for turbulent flow and transitional flow with fixed transition onset using different production term formulations in the SA model.....	139
Figure 5.69	Leading edge surface pressure coefficient distribution for the NASA-PW airfoil at the high incidence angle condition for turbulent flow and transitional flow with fixed transition onset using different production term formulations in the SA model.....	140
Figure 5.70	Surface pressure coefficient distribution for the NASA-PW airfoil at the high incidence angle condition for turbulent flow and transitional flow with fixed transition onset with and without streamline curvature correction...143	
Figure 5.71	Leading edge surface pressure coefficient distribution for the NASA-PW airfoil at the high incidence angle condition for turbulent flow and transitional flow with fixed transition onset with and without streamline curvature correction.....	144

Figure 5.72 Streamlines in the leading edge region of the NASA-PW airfoil (193 x 101 Grid) at the high incidence angle condition with streamline curvature correction for (a) fully turbulent flow, and (b) transitional flow using fixed transition onset with $x_{LT} = 0.08$ 145

Figure 5.73 Surface pressure coefficient distribution for the NASA-PW airfoil at the high incidence angle condition for turbulent flow and transitional flow with fixed transition onset for different inlet turbulent viscosities with streamline curvature correction..... 149

Figure 5.74 Leading edge surface pressure coefficient distribution for the NASA-PW airfoil at the high incidence angle condition for turbulent flow and transitional flow with fixed transition onset for different inlet turbulent viscosities with streamline curvature correction..... 150

LIST OF SYMBOLS

$A^+, C_{CP}, C_{KLEB}, C_{MUTM}, C_{WK}$	constants in the Baldwin-Lomax model
$c_{b1}, c_{b2}, c_{t1}, c_{t2}, c_{t3}, c_{t4}, c_{v1}, c_{w1}, c_{w2}, c_{w3}$	empirical constants in the Spalart-Allmaras model
C	airfoil chord
C_f	skin-friction coefficient
C_p	pressure coefficient
C_{CR}	constant in the curvature and rotation sensitization
C_L	lift coefficient
d	distance to the wall (Spalart-Allmaras model)
$f_{t1}, f_{t2}, f_{v1}, f_{v2}, f_w$	empirical functions in the Spalart-Allmaras model
$F(y)$	function used to determine F_{MAX} and y_{MAX} in the Baldwin-Lomax model
F_{CR}	function in the curvature and rotation sensitization
$F_{KLEB}(y)$	Klebanoff intermittency factor
F_{MAX}	maximum of function $F(y)$ (Equation (3.8)) in the Baldwin-Lomax model
F_{WAKE}	variable in the Baldwin-Lomax model
g, r, \tilde{S}	intermediate variables in the Spalart-Allmaras model
g_i	components of acceleration due to gravity ($i = 1, 2, 3$)
g_t	factor dependent on the grid for the transition term in the Spalart-Allmaras model
h	blade height
i, j, k	grid point indices
K	acceleration parameter, Clauser constant

ℓ	algebraic length scale in the Baldwin-Lomax model
L	lift force, airfoil chord
M	inlet Mach number
p	pressure
p_∞	pressure in the free stream, inlet pressure
P_n	turbulence production term in the Spalart-Allmaras model
Re_x	local Reynolds number
$(Re_x)_{st}$	Reynolds number between the point of separation and transition onset
$(Re_x)_{LT}$	Reynolds number between the length of transition
Re_L	Reynolds number based on chord
Re_{θ_s}	Reynolds number based on momentum thickness at the point of separation
Ri	Richardson number
s	strain rate
Δs	non-dimensional spacing of the first grid point off the airfoil surface
S	airfoil spacing or pitch, measure of the deformation tensor in the Spalart-Allmaras model
S_{ij}	strain rate tensor ($i, j = 1, 2, 3$)
S_r	streamwise point of flow reattachment
S_s	streamwise point of flow separation
t	time
t_{max}	maximum thickness of the airfoil
u, v	velocity components
\mathbf{u}	velocity vector

u_i	instantaneous velocity components ($i = 1, 2, 3$)
u_{DIF}	difference between the maximum and minimum velocity magnitude in the profile (Baldwin-Lomax model)
u_∞, U_∞, V	free stream velocity or inlet velocity
u_*	friction velocity
u^+, y^+	law-of-the-wall variables
\bar{u}	mean flow velocity
ΔU	norm of the difference between the velocity at the trip and that at the field point (Spalart-Allmaras model)
U_i	mean velocity components ($i = 1, 2, 3$)
U_j	mean velocity components ($j = 1, 2, 3$)
U_s	free stream velocity at the point of separation
x, y, z	Cartesian coordinates in physical space
x, X	chordal distance in the x direction
x	streamwise coordinate
Δx_t	grid spacing along the wall at the trip (Spalart-Allmaras model)
x_i	Cartesian coordinates ($i = 1, 2, 3$)
x_j	Cartesian coordinates ($j = 1, 2, 3$)
x_{max}	location of maximum thickness of the airfoil
x_{pitch}, y_{pitch}	Cartesian coordinate of the pitching axis location
x_r	streamwise point of flow reattachment, chordal distance of the point of flow reattachment (Tables in Chapter 5)
x_s	streamwise point of flow separation, chordal distance of the point of flow separation (Tables in Chapter 5)
x_{st}	streamwise distance between the point of separation and transition onset

x_t	streamwise point of transition onset
x_{LT}	streamwise length of transition
x_T	streamwise point of transition termination
X, Y, Z	Cartesian coordinates in physical space
y	coordinate normal to solid surface
y_{MAX}	value of y at which $F(y)$ (Equation (3.8)) is maximum (Baldwin-Lomax model)
Y	chordal distance in the y direction
$\bar{\alpha}$	mean incidence relative to the airfoil chord line
χ	intermediate variable in the Spalart-Allmaras model
δ	boundary layer thickness
δ_{ij}	Kronecker delta function
ε_{ij}	strain rate tensor
γ_I	intermittency factor
κ	von Kármán constant
μ	viscosity
μ_{eff}	effective turbulent (or eddy) viscosity
μ_t	turbulent (or eddy) viscosity
ν	kinematic viscosity
ν_s	kinematic viscosity at the point of separation
ν_t	kinematic turbulent (or eddy) viscosity
$\tilde{\nu}$	modified turbulent (or eddy) kinematic viscosity in the Spalart-Allmaras model
ω	vorticity

ω_t	vorticity at the wall at the trip point (Spalart-Allmaras model)
Ω_{ij}	vorticity tensor ($i, j = 1, 2, 3$)
ρ	density
ρ_∞	density in the free stream, inlet density
σ	turbulent Prandtl number
τ_0	shear stress at the wall
θ_s	momentum thickness at the point of separation
θ^*	leading edge camber angle
Θ	stagger angle
ξ, η, ζ	coordinates in the computational space

LIST OF FILES

File Name	File Size
1. Vivek_Hariharan_thesis.pdf.....	3.5 MB

Chapter One Introduction

Background

Almost every flow in nature and in practical engineering applications is turbulent. After years of research in turbulence, there still does not exist a precise definition of turbulence. However, some of the characteristics of turbulent flows can be listed: irregularity, diffusivity, large Reynolds numbers, three-dimensional vorticity fluctuations, and dissipation (Tennekes and Lumley, 1972). In spite of all the uncertainties associated with turbulent flows, it has been encouraging that engineering calculations have been possible with well-formulated turbulence models.

In 1937, Taylor and von Kármán proposed the following definition of turbulence: “Turbulence is an irregular motion which in general makes its appearance in fluids, gaseous or liquid, when they flow past solid surfaces or even when neighbouring streams of the same fluid flow past or over one another” (Wilcox, 1994). Turbulence is usually characterized by the presence of a wide range of length and time scales (Wilcox, 1994).

The Navier-Stokes (NS) equation, in its general form, has been around for two centuries now.

$$\rho \frac{Du_i}{Dt} = -\frac{\partial p}{\partial x_i} + \rho g_i + \frac{\partial}{\partial x_j} \left[2\mu \varepsilon_{ij} - \frac{2}{3} \mu (\text{div } \mathbf{u}) \delta_{ij} \right]$$

The NS equation combined with the continuity and energy equations describe the motion of fluid substances. These equations describe how the velocity, pressure, energy, and density of a moving fluid are related. The viscosity, μ , is a function of the thermodynamic state, and for most fluids displays a strong dependence on temperature. However, if the

temperature differences are not very large within the fluid, then μ can be regarded as a constant.

Another important flow characteristic of fluid flow is transition to turbulence. Transition is the process by which a laminar flow changes to a turbulent flow. It is known that, typically, the boundary layer flow is laminar over the surface of the body before it transitions to turbulent flow due to flow instabilities. Instability of a laminar flow does not immediately lead to turbulence, which is a severely nonlinear and chaotic stage characterized by macroscopic “mixing” of fluid particles. Some of the transition modes which lead to turbulence are natural transition, bypass transition, or separated flow transition. The discussion below on these different transition modes is a summary of what appears in Mayle (1991).

In the process for natural transition, after the initial breakdown of laminar flow occurs because of amplification of small disturbances, the flow goes through a complex sequence of changes finally resulting in the chaotic state known as turbulence. Natural transition occurs when the laminar boundary layer becomes susceptible to small disturbances, which grow into an instability. This instability amplifies within the layer to a point where it grows and develops into loop vortices with large fluctuations. These highly fluctuating loop vortices inside the laminar boundary layer develop into turbulent spots, which then are convected downstream, and eventually, with time, grow and coalesce to form a fully developed turbulent boundary layer.

Bypass transition usually occurs at high free-stream turbulence levels. In this mode of transition, free-stream disturbances influence the development of turbulent spots that are directly produced within the boundary layer.

Separated-flow transition occurs in the laminar separation bubble. The flow transitions into turbulent flow over the separated bubble and reattaches to the surface forming a turbulent shear layer. This usually occurs in an adverse pressure gradient region that contributes to the separation of the laminar boundary layer. Separated flow transition is usually found on the suction surface, near a compressor airfoil's leading edge, or near the point of minimum pressure. Turbine blades are likely to have separation along the suction surface in the trailing edge region. High levels of free-stream turbulence can cause early transition compared to lower turbulence levels.

In gas turbine engines, the flow is periodically unsteady, so is transition, and this is called periodic-unsteady transition. In "wake-induced" transition, the periodic passing of wakes from the upstream blades or obstructions causes unsteadiness in the flow field and affects transition on the downstream blades.

There also exists something called reverse transition, i.e., transition from turbulent to laminar flow, which is referred to as "relaminarization." This is usually expected to occur at low turbulence levels if the acceleration parameter, $K = (\nu/U^2)(dU/dx)$, is greater than 3×10^{-6} . In this equation, U refers to the velocity in the streamwise direction and x refers to the surface coordinate in the streamwise direction.

Predicting transition becomes very important for improving the efficiencies of gas turbine engines. Considering transition will lead to improved designs of turbomachinery airfoils. A significant amount of research effort has been devoted to determine the transition regime inside the boundary layer. Since Direct Numerical Simulation (DNS) and Large Eddy Simulation (LES) are more computationally expensive using present computing hardware, the Reynolds-Averaged Navier-Stokes (RANS) equations continue

to be better suited for engineering calculations with the incorporation of appropriate turbulence and transition models.

Literature Review

The incorporation of transition models into existing RANS solvers is an area of fundamental research interest. The Chen and Thyson (1971) model has been used by Ekaterinaris et al. (1995) and van Dyken et al. (1996) in a thin layer RANS code for transition calculations of steady (stationary) and oscillating airfoils. An adjustment of the Chen-Thyson transition constant was necessary to get better correlation with experimental data since the basis of this constant was on zero pressure gradient flow.

Solomon et al. (1996) developed a relationship that considers the influence of pressure gradients as well as free-stream turbulence intensity on transition length for attached flow. Sanz and Platzer (1998) used the Solomon et al. (1996) transition model for transitional flow calculations. Computations were performed on separation bubbles for a NACA0012 airfoil and found that the Solomon et al. transition model successfully predicted the NACA0012 airfoil separation bubbles. This work was continued by Sanz and Platzer (2002) to determine the influence of turbulence models and discretization methods on transition predictions.

Suzen et al. (2003) developed a transition model by combining the models of Steelant and Dick (1996) and Cho and Chung (1992) to solve a transport equation for the intermittency factor. Suzen et al. found that the intermittency thus obtained reproduced the experimentally observed streamwise variation of the intermittency in the transition region, and could also provide a realistic picture of normal-to-wall variation of the

intermittency profile. Using this transition model, good overall agreement of the computational predictions with the experimental data was demonstrated.

Langtry and Sjolander (2002) proposed a transition model for predicting the onset of transition by taking into account the influence of freestream turbulence intensity, pressure gradient and flow separation. The model was based on the concept of vorticity Reynolds number (proposed by Van Driest and Blumer, 1963) and calibrated for use with the Menter SST turbulence model. Langtry and Sjolander used their transition model on different test cases and demonstrated good agreement with the experiments as compared to laminar and turbulent solutions.

The majority of transition models depend on boundary layer parameters. This makes transition models difficult to apply to three dimensional flows and advanced Computational Fluid Dynamics (CFD) codes that use unstructured grids. To overcome this difficulty, Menter et al. (2002) developed a correlation-based method with a general transport equation that depends on local variables. This approach has been extended by Menter et al. (2006) to include two transport equations, one for intermittency and one for the transition onset criteria through use of the momentum thickness Reynolds number. Application of this approach to a number of different test cases yielded promising results.

Recently Whitlow et al. (2006) used a three dimensional RANS code and a two dimensional RANS code with the Solomon et al. (1996) transition model to predict the flow for the NASA-Glenn Research Center (GRC) Transonic Flutter Cascade (TFC) airfoil. Steady flow computations were performed for both the low and large incidence angle cases for which surface pressure measurements are available. Distinct leading edge separation bubbles were predicted for each incidence angle. In particular, for the large

incidence case, improved correlation with the measurements was exhibited compared to the fully turbulent calculations.

Objectives

The overall objective of this research is to predict the transitional flow regime for steady flow over a transonic compressor (NASA-PW) airfoil cross-section. The numerical results obtained are correlated with the experimental data obtained from the Transonic Flutter Cascade (TFC) at NASA Glenn Research Center (GRC). The effect of different transition lengths and transition onset models on the steady pressure distribution is studied. The investigation is done for a low incidence angle and a high incidence angle condition. The high incidence angle condition has a large separation bubble on the suction surface in the leading edge region.

In particular, computational studies are done for turbulent and transitional flow on a flat plate airfoil, and the NASA-PW airfoil. The turbulent flow predictions use the Spalart-Allmaras (SA) (1994) one-equation turbulence model. The transitional flow predictions use the intermittency correlation given by Dhawan and Narasimha (DN) (1958) for fixed transition length and Mayle's (1991) transition length model. The DN model was selected because the transition onset location and transition length could be varied independently.

In this research, the flat plate studies are crucial in order to validate the implementation of the numerical scheme. Since experimental data for turbulent and transitional flows over flat plates are readily available, the numerical results obtained are correlated with this data. The effect of inlet turbulent viscosity is also quantified for the

SA model. In addition, the effect of turbulence production in the SA model is also investigated by using the mean-strain rate based production, blended mean-strain rate and vorticity based production, and the classical vorticity based production. Moreover, streamline curvature effect is also studied by sensitizing the SA model to such effects. Furthermore, a new approach to speed up the convergence of the solution for the NASA-PW airfoil has been explored by combining the Baldwin-Lomax (BL) (1978) algebraic turbulence model and the SA model.

Chapter Two Geometry and Grid Generation

Cascade Geometry

The experimental data for this work was generated in the NASA-GRC TFC (Buffum et al., 1998). An exhaust system was used to draw atmospheric air through honeycomb into a smoothly contracting inlet section; test section Mach numbers up to 1.15 were possible. Downstream of the inlet was a rectangular duct that contained the nine airfoil test section. This facility had the unique capability of oscillating the nine airfoils simultaneously at a specified interblade phase angle using a high-speed cam driven system at frequencies up to 550 Hz. The experimental data used in this work were acquired at an inlet Mach number of 0.5 with a chordal Reynolds number of 0.9 Million for a low and high incidence angle condition.

To reduce the boundary layer thickness, suction was applied to the cascade side walls through perforated walls upstream of the test section. The tailboards used to control the test section exit pressure also formed bleed scoops to reduce the upper and lower wall boundary layers. Chordwise surface static pressure taps were located at mid-span (52% span) as well as 35% and 17.5% span. For the high incidence angle condition, the chordwise pressure distributions at each span location were nearly identical with a slight deviation at the 17.5% span location for the static pressure measurement nearest to the airfoil leading edge. Flow visualization using an oil-pigment mixture indicated that at the high incidence angle condition the flow was separated at mid-span from the leading edge to 40% chord. The separated flow region did decrease in chordwise extent to approximately 7% chord near the upper and lower walls. Based on the experimental

results a two-dimensional analysis was pursued of the mid-span region of the cascade airfoils.

Airfoil Geometry

The airfoil geometry used in this work is that of the experimental setup in the NASA-GRC TFC. This NASA-PW airfoil has a cross-section similar to that found in the tip region of low aspect ratio fan blades. The airfoil cascade parameters are given in Table 2.1 and Figure 2.1 gives the details of the geometry.

Table 2.1: Airfoil and Cascade parameters (Buffum et al., 1998)

Chord, C	8.89 cm
Maximum thickness, t_{max}	0.048C
Maximum thickness location, x_{max}	0.625C
Leading edge camber angle, θ^*	-9.5°
Number of airfoils	9
Stagger angle, Θ	60°
Solidity, C/S	1.52
Pitching axis (x_{pitch} , y_{pitch})	(0.5C, -0.017C)
Blade height, h	9.59 cm

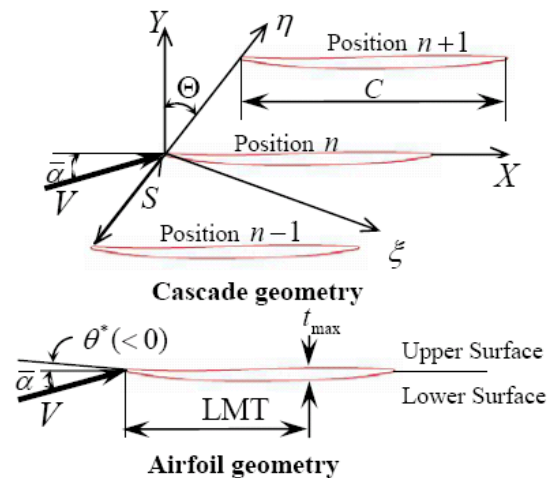


Figure 2.1: Airfoil and cascade geometry

Grid Generation

The grids were generated using POINTWISE. The two dimensional grids have a sheared H-mesh topology. The grids generated have the first grid point off the airfoil surface so as to yield y^+ values of order $\mathcal{O}(1)$. Figure 2.2 below shows typical y^+ values for the first grid point off the airfoil surface from the leading edge to the trailing edge of the airfoil. The grids were generated in a manner so as to closely follow the airfoil surface profile from the leading edge up to the trailing edge. It was ensured that the grid lines emanating from the airfoil surface remain nearly orthogonal to the surface up to and exceeding the boundary layer thickness. This guarantees that the grid cells close to the airfoil surface are not skewed. The expansion ratio of the grid away from the airfoil surface is maintained at a value of 1.2.

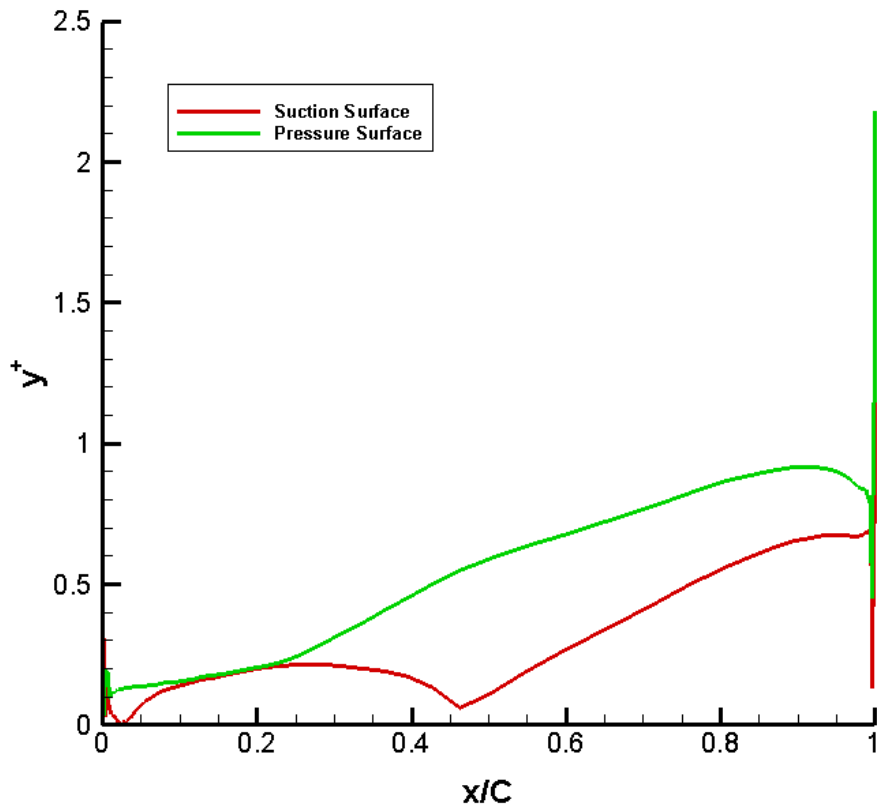


Figure 2.2: Chordwise distribution of y^+ over the NASA-PW airfoil surface (193 x 101 Grid)

Different Types of Grids

Before numerical solution of the governing equations can be generated, the flow domain and its boundaries must be discretized. The choice of discretization is made between structured and unstructured grids. Figure 2.3 presents an example of a structured grid and Figure 2.4 shows an example of an unstructured grid. Both structured and unstructured grids have their own specific advantages and disadvantages. Since the grids used in this research are structured grids, the discussion below will be limited to structured grids only.

The grid points in a structured grid are distinctively identified by a particular set of indices i, j, k (one for each coordinate direction) and every grid point has the set of Cartesian coordinates in physical space given by $(x_{i,j,k}, y_{i,j,k}, z_{i,j,k})$. The set of coordinates in the computational space is given by $(\xi_{i,j,k}, \eta_{i,j,k}, \zeta_{i,j,k})$. The grid cells formed in a structured grid are quadrilateral in shape in 2-D and hexahedral in shape in 3-D. The different types of grid topologies that can be employed for structured grids are H-, C-, and O-grids.

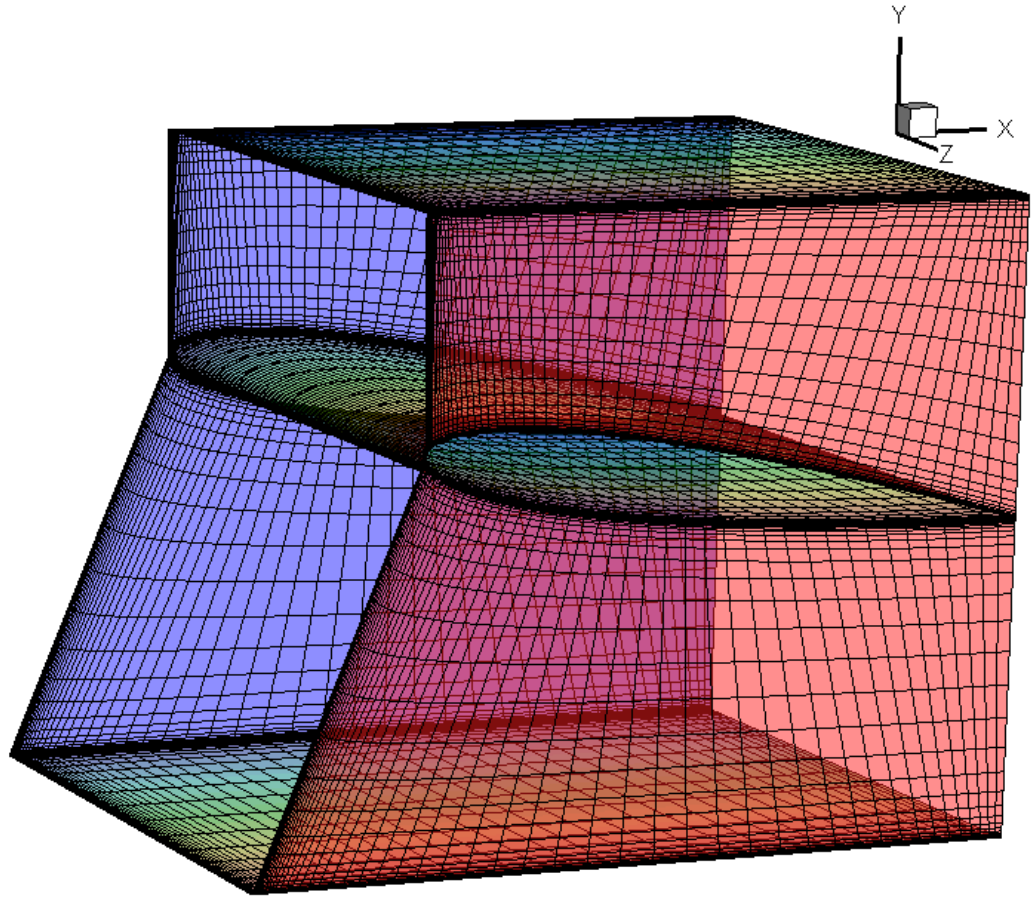


Figure 2.3: Example of a 3-D structured grid for an extruded NACA-0012 airfoil

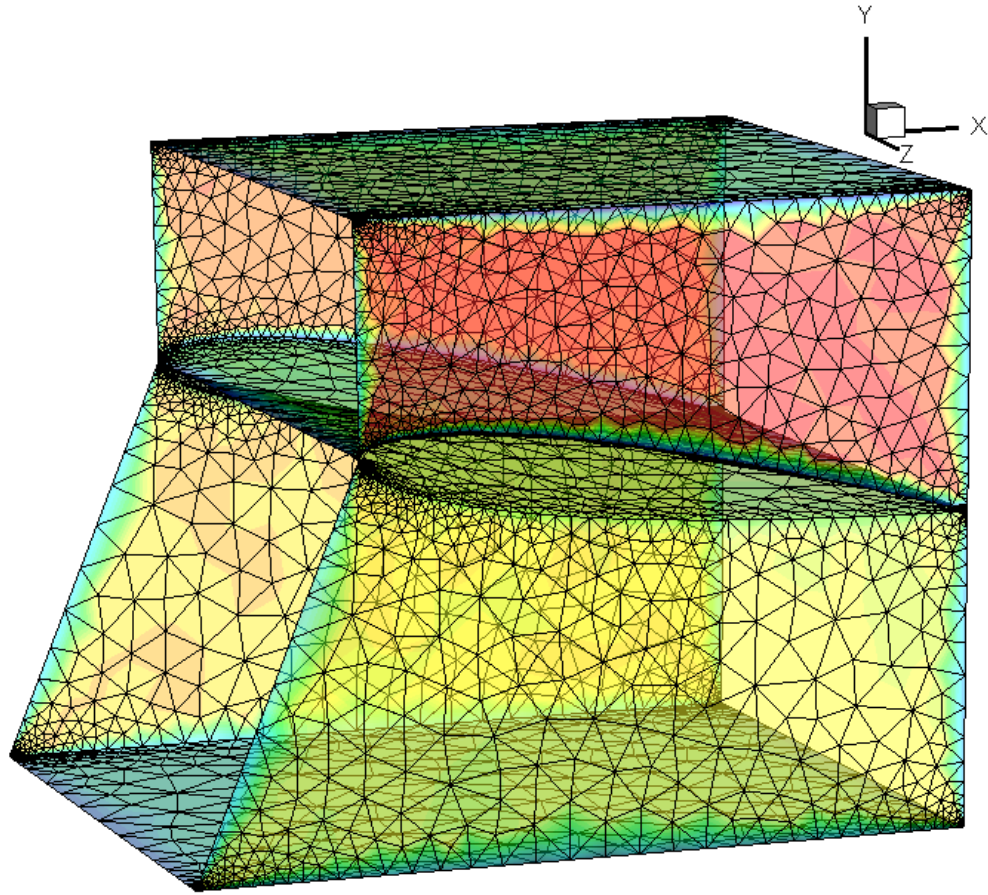


Figure 2.4: Example of a 3-D unstructured grid for an extruded NACA-0012 airfoil

Traditional H-grids and Sheared H-grids

The H-grid topology is most often employed for turbomachinery applications. The H-grid topology is shown in Figure 2.5. As can be seen, the $\eta = 0$ and $\eta = 1$ grid lines represent the periodic boundaries and the surfaces of the aerodynamic body. Moreover, an $\eta = \text{const.}$ grid line begins at the inlet boundary, which is located at $\zeta = 0$, and ends at the outlet boundary, which is located at $\zeta = 1$.

In turbomachinery, the segments from the inlet boundary to the leading edge that are represented by 1-3 and 2-4 are called the periodic boundaries since they are periodic

to each other. In fact, they are rotationally periodic in 3-D. The same applies to the segments 5-7 and 6-8. The grid points along the periodic boundaries should be placed in such a way that they are clustered near the leading edge and trailing edge regions of the blade. This is usually done by making the spacing of the first grid point along the periodic boundary the same as that of the first grid point over the turbomachine blade's leading and trailing edges, respectively. Segments 3-5 and 4-6 have solid-wall boundary conditions.

The traditional H-grids have grid point distribution such as to yield symmetric looking grid cells that are not distorted or skewed. Sheared H-grids distort the grid cells near the leading edge and trailing edge of the airfoil's surface resulting in skewed looking cells. In Figure 2.5, the traditional H-grid topology can be seen in the inlet and exit portions of the grid, and in the mid-channel region between the airfoil surfaces. The sheared H-grid topology can be seen near the leading edge and trailing edge regions of the airfoil's surface. The grid point clustering along the boundaries of the grid and also over the solid walls allows capturing the flow gradients accurately and to resolve the viscous terms present in the NS equation and in any turbulence model. This allows the cells to be stretched easily to account for different flow gradients in different directions.

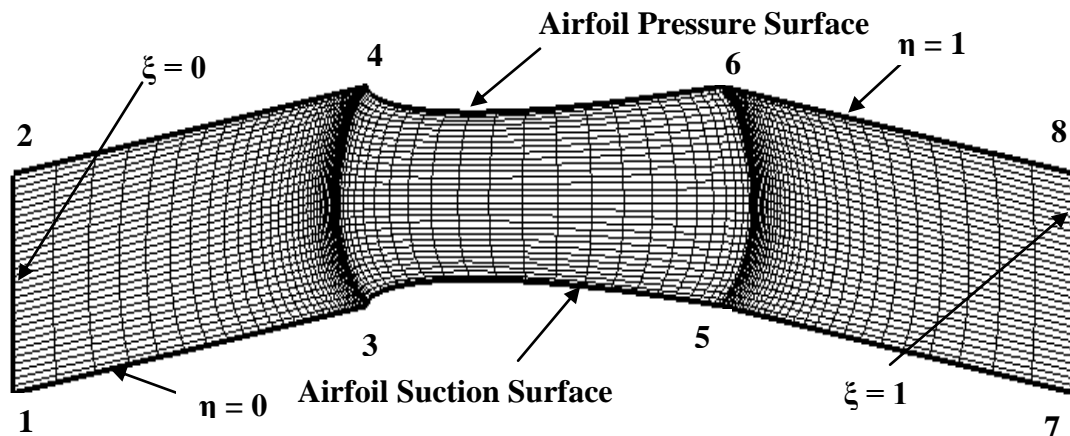


Figure 2.5: An example of H-grid topology over a NACA-0012 airfoil

C-grids

C-grid topology around an aerodynamic body consists of a family of grid lines that wrap around the surface of the body and also form the wake region behind the body. The C-grid topology is shown in Figure 2.6. The C-grid topology when generated introduces a coordinate cut, as also seen in the figure. The coordinate cut requires mapping a single grid point in the physical domain onto two grid points in the computational domain. Using a C-grid topology around an aerodynamic body, in general, reduces skewness of the grid cells on the whole domain when compared to H-grids. In particular, grid skewness is reduced near the leading edge as the grid lines wrap around the leading edge and closely follows the leading edge surface profile in a better way as compared to the grid cells in H-grid topology. Grid cells with low values of skewness are important to reduce numerical errors during computation. Now, due to the presence of the coordinate cut emanating from the trailing edge, a periodic boundary condition is preferred at the cut so that the flow variables and gradients remain continuous across the cut.

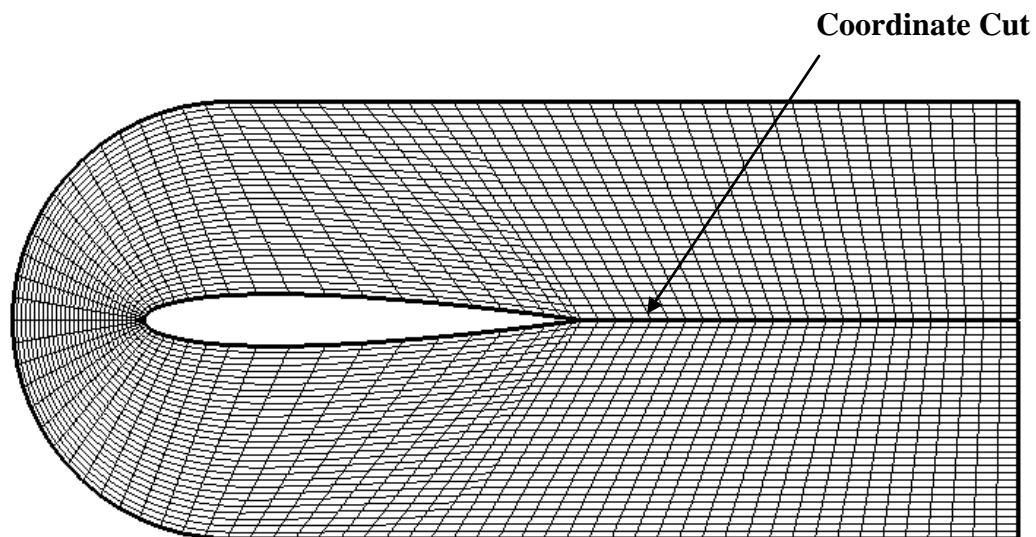


Figure 2.6: C-grid around a NACA-0012 airfoil

O-grids

In the case of O-grids, a family of grid lines form closed loops around the aerodynamic body. The O-grid topology is displayed in Figure 2.7. The other family of grid lines traverse in the radial direction away from the body and towards the outer boundary. Again, as was found with the C-grids, generating an O-grid for an airfoil creates a coordinate cut as shown in the Figure 2.7. An O-grid around the airfoil surface resolves the boundary layer region near the surface in a much better manner by closely following the surface profile of the airfoil. However, an airfoil with a sharp trailing edge having an O-grid topology affects the grid quality in that region. Moreover, as with C-grids, difficulty arises to keep the flow variables and their gradients continuous across the cut and a periodic boundary is always preferred.

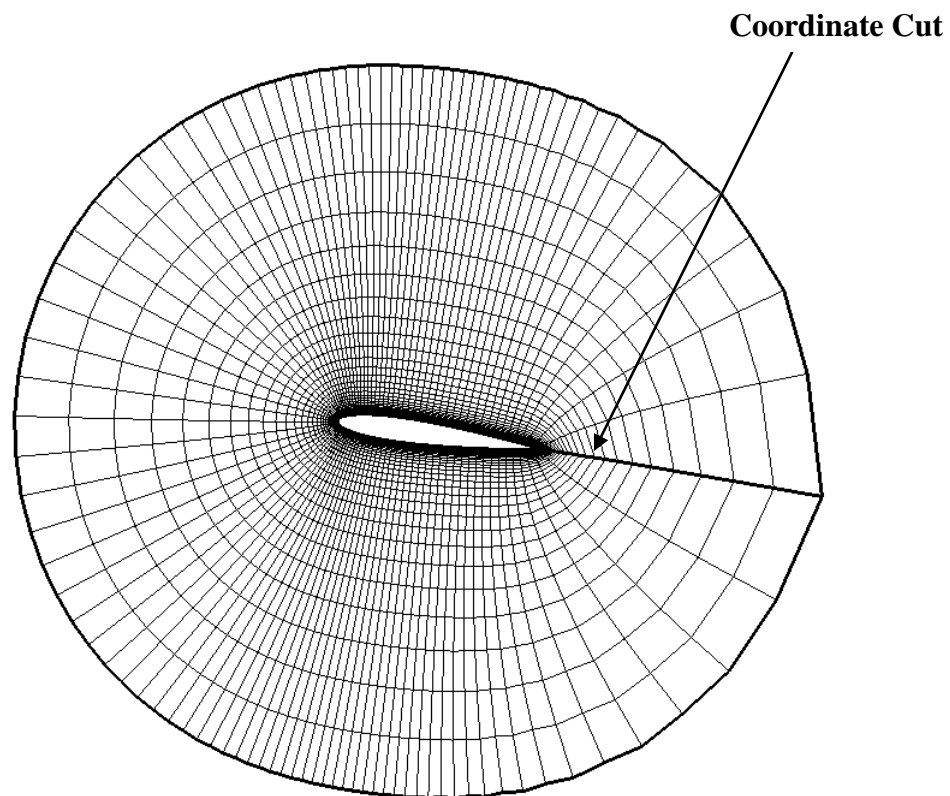


Figure 2.7: Example of O-grid around a NACA-0012 airfoil

Grids for Flat Plate Studies

Table 2.2 lists the essential features of the grids used for flat plate studies.

Table 2.2: Flat plate airfoil grids

Grid Size	Δs	Inlet Boundary	Exit Boundary	S/C	Θ
161 x 82	5.0E-6	2C	2C	10	0°
238 x 164	1.0E-6	2C	2C	1	0°
418 x 161	1.0E-5	2C	3C	1	0°

The grid size represents the number of grid points in the ‘ x ’ and ‘ y ’ directions corresponding to ‘ i ’ and ‘ j ’ directions, respectively. A typical flat plate grid is shown in Figure 2.8. The non-dimensional spacing of the first grid point off the airfoil surface is given by Δs . The values for the inlet and exit boundaries represent the non-dimensional distance at which the boundaries are located from the leading edge and the trailing edge of the airfoil, respectively. The ratio S/C is the space-chord ratio and is the inverse of solidity of the airfoil. The stagger angle of the flat plate airfoil cascade is represented by Θ .

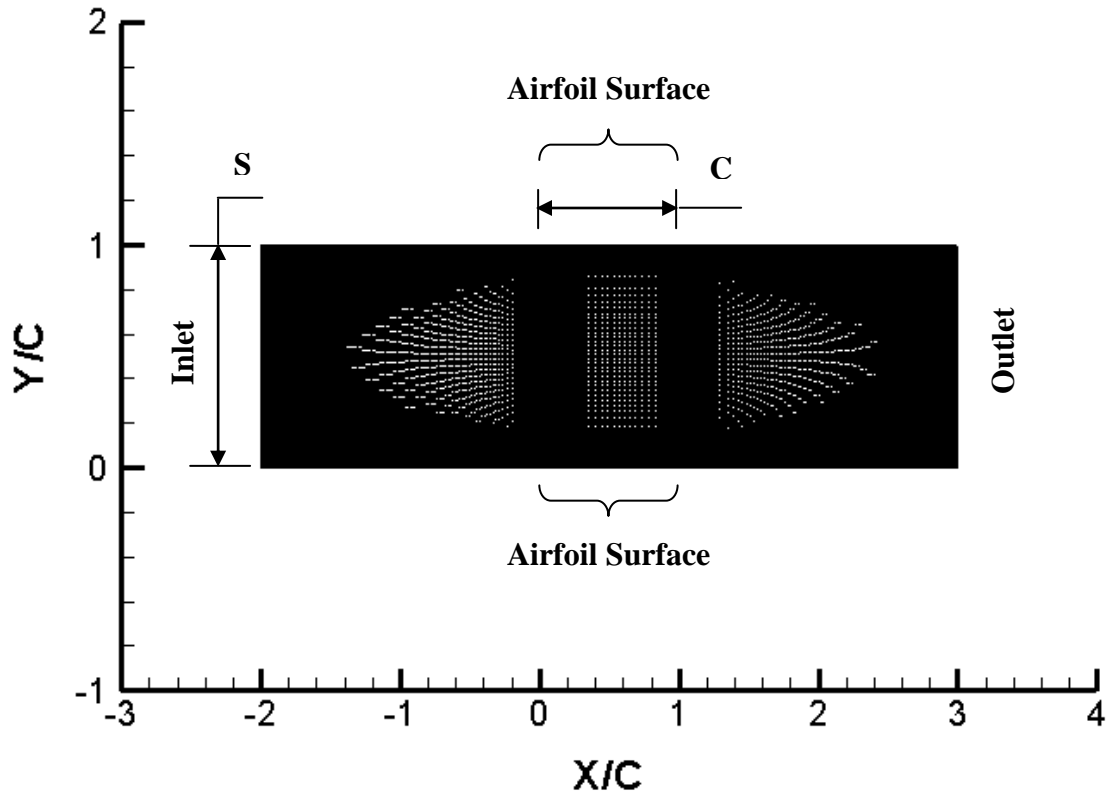


Figure 2.8: Computational domain for the flat plate airfoil (238 x 164 Grid)

Grids for NASA-PW Airfoil

Table 2.3 lists the essential features of the grids used for NASA-PW airfoil.

Table 2.3: NASA-PW airfoil grids

Grid Size	Δs	Inlet Boundary	Exit Boundary	S/C	Θ
193 x 101	5.0E-6	3C	3C	0.65789	60°
363 x 201	5.0E-6	3C	3C	0.65789	60°

The discussion immediately following Table 2.2 also applies to Table 2.3. Some typical views of the grids used in this research are displayed below in Figures 2.9 through

2.12. The grid distribution near the airfoil surface is such that it resolves the boundary layer region effectively by having the grid points move away from the surface in a geometric fashion. The coarse grid of size 193 x 101 has 85 grid points over the airfoil surface, and the dense grid of size 363 x 201 has 182 grid points over the airfoil surface. Grid independence of fully turbulent and transition solutions were demonstrated using these grids.

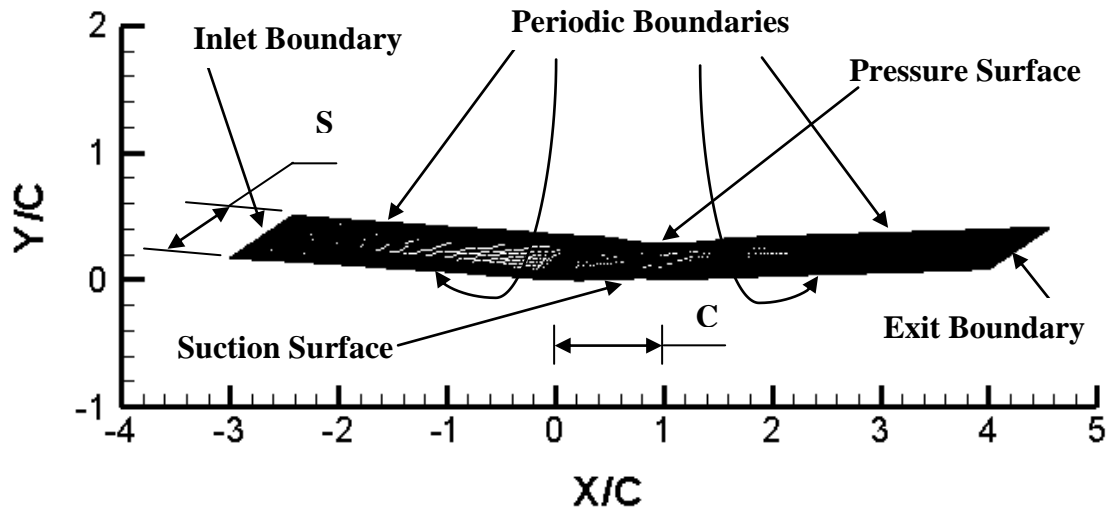


Figure 2.9: Computational domain for the NASA-PW airfoil (193 x 101 Grid)

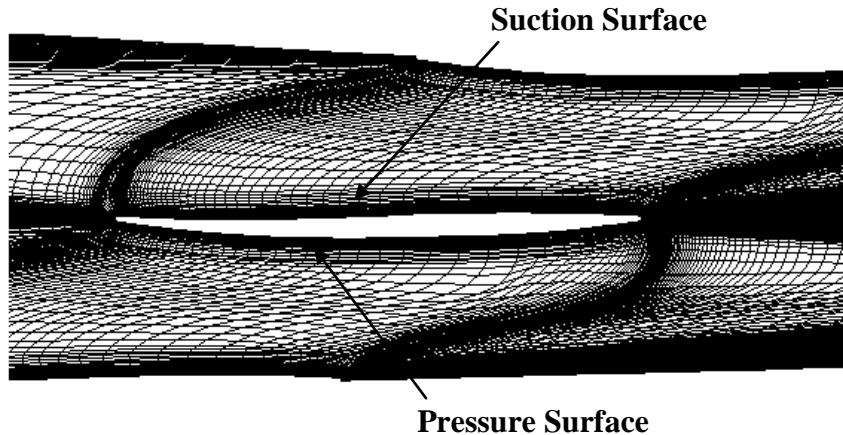


Figure 2.10: Airfoil surface grid topology for the NASA-PW airfoil (193 x 101 Grid)

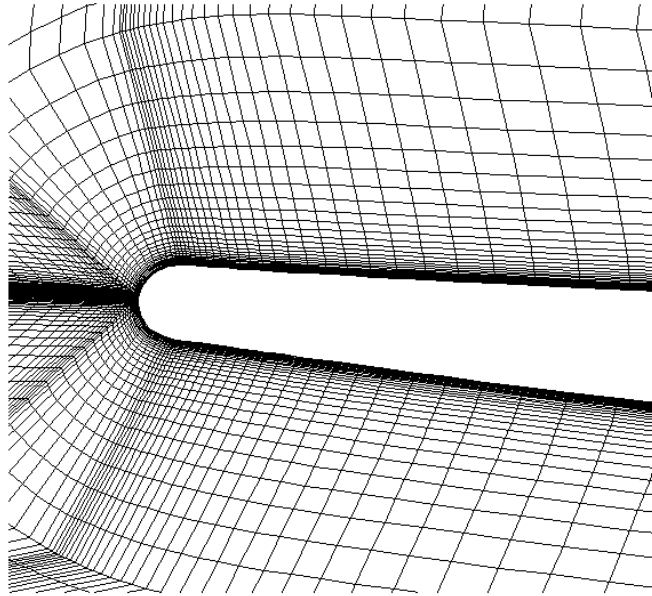


Figure 2.11: Grid topology in the leading edge region of the NASA-PW airfoil (193 x 101 Grid)

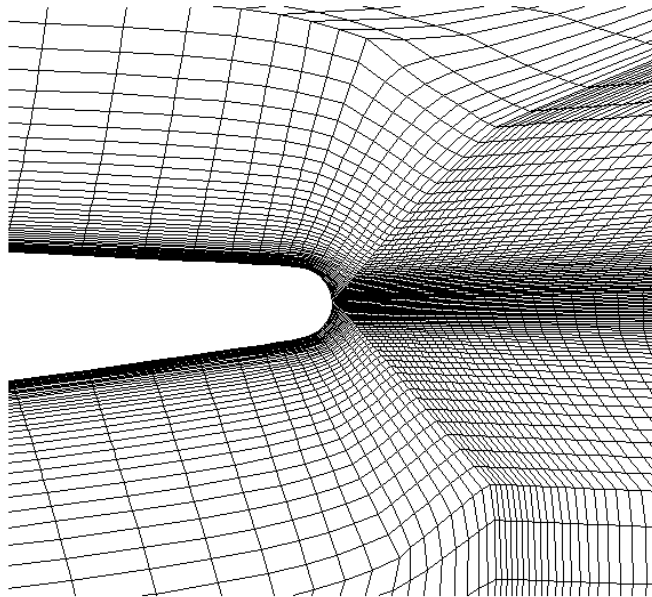


Figure 2.12: Grid topology in the trailing edge region of the NASA-PW airfoil (193 x 101 Grid)

Chapter Three

Turbulence and Transition Models

Turbulence

It is now understood and accepted that turbulent flows are characterized by varying length and time scales. The inherent nature of turbulent flow causes the velocity field to fluctuate. This in turn yields rapid mixing of the transported quantities, such as momentum and energy. To capture the exact physics of the flow, especially for the small-scale high-frequency fluctuations, DNS of the governing equations is required. Since DNS is too computationally expensive with present computing hardware for practical engineering applications, other approaches, such as time-averaging or ensemble-averaging of the instantaneous governing equations, are employed. However, the modified equations contain additional unknown variables creating what is called the turbulence ‘closure’ problem. Hence, turbulence models are needed to determine these additional variables. Reynolds averaging the NS equation introduces additional stress terms, known as the Reynolds stress, which acts on the mean turbulent flow. Boussinesq proposed to address these Reynolds stress terms by introducing what is called the turbulent or eddy viscosity in a manner analogous to laminar shear stress.

Baldwin-Lomax Algebraic Turbulence Model

The Baldwin-Lomax (BL) (1978) model is a two-layer algebraic model (also called a zero-equation model) which gives the eddy viscosity, μ_t , as a function of the local boundary layer velocity profile. The eddy viscosity is calculated in this research by using a blending function as proposed by Granville (1990) that is given by

$$\mu_t = (\mu_t)_{outer} \tanh \left[\frac{(\mu_t)_{inner}}{(\mu_t)_{outer}} \right]. \quad (3.1)$$

The Prandtl-Van Driest formulation is used in the inner region which gives

$$(\mu_t)_{inner} = \rho \ell^2 |\omega| \quad (3.2)$$

where

$$\ell = \kappa y [1 - \exp(-y^+/A^+)]. \quad (3.3)$$

The magnitude of the vorticity, $|\omega|$, for two dimensional flow is given by

$$|\omega| = \sqrt{\left(\frac{\partial u}{\partial y} - \frac{\partial v}{\partial x} \right)^2} \quad (3.4)$$

and

$$y^+ = \frac{y u_*}{\nu}. \quad (3.5)$$

For the outer region

$$(\mu_t)_{outer} = K C_{CP} \rho F_{WAKE} F_{KLEB}(y) \quad (3.6)$$

where K is the Clauser constant, which is given with the other modeling constants in Table 3.1.

$$F_{WAKE} = \min \left(y_{MAX} F_{MAX}, \frac{C_{WK} y_{MAX} u_{DIF}^2}{F_{MAX}} \right) \quad (3.7)$$

The quantities y_{MAX} and F_{MAX} are determined from the maximum of the function

$$F(y) = y |\omega| [1 - \exp(-y^+/A^+)]. \quad (3.8)$$

For computation in the wake region, the exponential term in $F(y)$ is set to zero. The Klebanoff intermittency factor, $F_{KLEB}(y)$, is given by

$$F_{KLEB}(y) = \left[1 + 5.5 \left(\frac{C_{KLEB} y}{y_{MAX}} \right)^6 \right]^{-1}. \quad (3.9)$$

The quantity u_{DIF} is the difference between the maximum and minimum velocity magnitude in the profile at a specific x location and is given by, for two dimensional flow,

$$u_{DIF} = \max\left(\sqrt{u^2 + v^2}\right) - \min\left(\sqrt{u^2 + v^2}\right). \quad (3.10)$$

For boundary layers, the minimum is always set to zero in the above equation.

The effect of transition from laminar to turbulent flow can be simulated by setting μ_t to zero everywhere in a profile where the maximum computed value of μ_t is less than a specified value, that is, $\mu_t = 0$ if $\max(\mu_t)_{profile} < C_{MUTM} u_\infty$. However, this feature of the Baldwin-Lomax model has not been implemented in the flow solver used for the purpose of this research.

The constants in the Baldwin-Lomax model take the values presented in Table 3.1, as used by Chima, Giel, and Boyle (1993).

Table 3.1: Baldwin-Lomax turbulence model constants

A^+	26
C_{CP}	1.216
C_{KLEB}	0.646
C_{WK}	1
κ	0.4
K	0.0168
C_{MUTM}	14

In the Baldwin-Lomax model, the distribution of vorticity is used to determine length scales so that the necessity for finding the outer edge of the boundary layer is

removed. The model is suitable for high-speed flows with thin attached boundary layers (http://www.cfd-online.com/Wiki/Baldwin-Lomax_model, 2007). The Baldwin-Lomax model was not developed for cases with large separation bubbles or significant rotation/curvature effects.

The Baldwin-Lomax model requires a well-resolved grid near the walls, with the first cell off the airfoil surface located at $y^+ < 1$. The model does not always give accurate solutions, especially for cases with large separation zones and recirculation. However, the Baldwin-Lomax model can be used to provide a reasonable initial condition for more sophisticated turbulence models.

Spalart-Allmaras One-Equation Turbulence Model

The Spalart-Allmaras (1994) model is a one-equation model that solves a transport equation to determine the eddy viscosity to resolve the turbulence closure problem. The transport equation is based on empiricism, dimensional analysis, Galilean invariance, and dependence on the molecular viscosity. The model was calibrated using two-dimensional mixing layers, wakes, and flat plate boundary layers. The model gives satisfactory results for boundary layers subjected to pressure gradients.

The Spalart-Allmaras (SA) model solves for the transport variable, $\tilde{\nu}$, which is a modified form of the turbulent kinematic viscosity and obeys the transport equation

$$\begin{aligned} \frac{D\tilde{\nu}}{Dt} = c_{b1}[1 - f_{t2}]\tilde{S}\tilde{\nu} + \frac{1}{\sigma}[\nabla \cdot ((\nu + \tilde{\nu})\nabla\tilde{\nu}) + c_{b2}(\nabla\tilde{\nu})^2] \\ - \left[c_{w1}f_w - \frac{c_{b1}}{\kappa^2}f_{t2} \right] \left[\frac{\tilde{\nu}}{d} \right]^2 + f_{t1}\Delta U^2, \end{aligned} \quad (3.11)$$

where

$$v_t = \tilde{v} f_{v1} \quad (3.12)$$

$$f_{v1} = \chi^3 / (\chi^3 + c_{v1}^3) \quad (3.13)$$

$$\chi = \tilde{v}/v \quad (3.14)$$

$$\tilde{S} = S + (\tilde{v}/\kappa^2 d^2) f_{v2} \quad (3.15)$$

$$f_{v2} = 1 - \chi / (1 + \chi f_{v1}) \quad (3.16)$$

$$f_w = g \left[(1 + c_{w3}^6) / (g^6 + c_{w3}^6) \right]^{1/6} \quad (3.17)$$

$$g = r + c_{w2}(r^6 - r) \quad (3.18)$$

$$r = \tilde{v} / \tilde{S} \kappa^2 d^2 \quad (3.19)$$

$$f_{t2} = c_{t3} \exp[-c_{t4} \chi^2] \quad (3.20)$$

$$f_{t1} = c_{t1} g_t \exp \left[-c_{t2} \left(\omega_t^2 / \Delta U^2 \right) (d^2 + g_t^2 d_t^2) \right] \quad (3.21)$$

$$g_t = \min \left(0.1, \Delta U / \omega_t \Delta x_t \right). \quad (3.22)$$

The constants in the SA model are given below in Table 3.2.

Table 3.2: Spalart-Allmaras turbulence model constants

σ	2/3
c_{b1}	0.1355
c_{b2}	0.622
c_{w1}	$(c_{b1}/\kappa^2) + (1+c_{b2})/\sigma$
c_{w2}	0.3
c_{w3}	2
κ	0.41
c_{v1}	7.1
c_{t1}	1
c_{t2}	2
c_{t3}	1.2
c_{t4}	0.5

The terms on the right-hand side of the transport equation represent eddy-viscosity production, diffusion, and destruction. The effect of transition is also included through the $f_{t1}\Delta U^2$ term.

The production term, which is the first term on the right-hand side of the transport equation, can be modified to improve the accuracy of the solution. The modification applies to the scalar measure of the deformation tensor, S . The original SA model uses the magnitude of vorticity, $|\omega|$ for S .

$$S = |\omega| = (2\Omega_{ij}\Omega_{ij})^{1/2}, \quad (3.23)$$

where Ω_{ij} is the vorticity tensor given by

$$\Omega_{ij} = \frac{1}{2} \left(\frac{\partial U_i}{\partial x_j} - \frac{\partial U_j}{\partial x_i} \right). \quad (3.24)$$

The argument that supports using $|\omega|$ for S is that, for aerodynamic flows for which the model was formulated, turbulence is found only where vorticity is present near the solid boundaries. The other possible choice for S is to base it on the magnitude of strain rate $|s|$ as indicated by Spalart and Allmaras (1994) and Dacles-Mariani et al. (1995).

$$S = |s| = (2S_{ij}S_{ij})^{1/2}, \quad (3.25)$$

where S_{ij} is the strain rate tensor defined as

$$S_{ij} = \frac{1}{2} \left(\frac{\partial U_i}{\partial x_j} + \frac{\partial U_j}{\partial x_i} \right). \quad (3.26)$$

However, a new form for S has been proposed in Dacles-Mariani et al. (1995) that combines both $|\omega|$ and $|s|$ as follows:

$$S = |\omega| + C_{prod} \min(0, |s| - |\omega|), \quad (3.27)$$

where $C_{prod} = 2$. The motivation for this modification is that taking into account both vorticity and strain rate reduces the eddy viscosity being generated in regions where the vorticity exceeds the strain rate. This behavior can be seen at the core of a vortex where pure rotation is taking place and consequently the turbulence should be suppressed (Dacles-Mariani et al., 1995).

History effects are taken into account by the Spalart-Allmaras model, where the convection and the diffusion of turbulence is modeled by the transport equation presented above. This model is easy to implement on structured as well as unstructured grids.

The capability of the Spalart-Allmaras model to yield smooth laminar-turbulent transition at the point specified by the user is not used in the present work. An explicit transition model is used in this research. Thus, the solution generated by using the Spalart-Allmaras model only represents a fully turbulent solution right from the leading edge.

Boundary and Initial Conditions for the Spalart-Allmaras Turbulence Model

To obtain a physical solution to the governing equations, appropriate initial and boundary conditions need to be specified. The initial conditions provide the state of the fluid at time $t = 0$.

In computer simulation of a physical flow domain, only a part of the physical domain is considered. This results in truncation of the original flow domain and creates non-physical boundaries, such as inlet boundaries, outlet boundaries, and periodic boundaries. At these boundaries the values of the flow variables must be specified. Moreover, the solution obtained on the truncated domain should represent the solution for the entire physical domain.

The wall boundary condition for the SA model requires the modified turbulent kinematic viscosity, $\tilde{\nu}$, is zero. For the exit boundary, extrapolation from the interior of the flow domain is used to specify the values at the boundary. At the inlet boundary, the Dirichlet boundary condition is used that requires specifying the turbulent viscosity. For the periodic boundaries, the values are specified using the periodicity condition. More details concerning the inlet boundary condition and initial condition for the modified turbulent viscosity for the SA model are given in the next section.

Inlet Turbulent Viscosity and Initial Condition

The non-dimensional inlet turbulent viscosity in the SA model was previously specified as 0.009 (CFL3D Version 5.0 User's Manual, 1997). In this research the capability of specifying any desired inlet turbulent viscosity was added to the SA model. This was accomplished through use of a set of correlations for converting the turbulent eddy viscosity, ν_t , to the modified eddy viscosity in the SA model, $\tilde{\nu}$, provided by Wong (1999). The correlations are presented below.

$$\tilde{\nu} = \frac{\nu_t}{4} + \frac{a}{2} + \frac{\sqrt{(\nu_t^2/2) + a\nu_t - b + 2\sqrt{4c_{v1}^3\nu^3\nu_t + b^2}}}{2} \quad (3.28)$$

where

$$a = \sqrt{\nu_t^2/4 + b} \quad (3.29)$$

$$b = (c - e\nu_t^2)/4e \quad (3.30)$$

$$c = e\nu_t^2 - 73728^{1/3}c_{v1}^3\nu^3\nu_t + \left(\frac{32}{243}\right)^{1/3}e^2 \quad (3.31)$$

$$e = \left[\sqrt{2304c_{v1}^6\nu^6f + f^2} - f\right]^{1/3} \quad (3.32)$$

$$f = 243c_{v1}^3\nu^3\nu_t^3 \quad (3.33)$$

The value of c_{v1} is the same as that in the SA model. The above correlations can be used to specify and test the effect of different initial conditions of $\tilde{\nu}$ on the final solution. Furthermore, the effect of specifying a fixed value of $\tilde{\nu}$ at the inlet boundary can be investigated.

The above procedure can also be used to generate better initial conditions for the SA model by obtaining an initial solution with the BL model and utilizing the turbulent viscosity, ν_t , calculated and converting it to the transformed eddy viscosity, $\tilde{\nu}$, using the relationships presented by Wong (1999).

Streamline Curvature Correction

Sensitization of the solution to the effects of streamline curvature can be studied by implementing the model proposed by Hellsten (1998). In the present work, the suggested model of Hellsten is incorporated into the SA turbulence model by effectively modifying the turbulence production term of the SA model. The model equations are presented below.

$$F_{CR} = \frac{1}{1 + C_{CR} Ri}, \quad (3.34)$$

$$Ri = \frac{|\omega|}{|s|} \left(\frac{|\omega|}{|s|} - 1 \right), \quad (3.35)$$

where $C_{CR} = 3.6$, and the terms $|\omega|$ and $|s|$ are the magnitude of vorticity and the magnitude of strain rate, respectively, as given above. The Richardson number, Ri , which is a dimensionless number indicates the level of turbulence in the flow with lower values indicating significant turbulence. The FCR model has been calibrated for a rotating channel flow (Hellsten, 1998). The term F_{CR} sensitizes the SA turbulence model, which is an eddy-viscosity model, for curvature/rotation effects. As recommended by Yaras and Grosvenor (2003) the F_{CR} term is multiplied by the production term in the SA model. In the code used for the purpose of this research, the FCR correction of Hellsten has been implemented as described above with the option of turning the FCR correction on/off.

Transition from Laminar to Turbulent Flow

Emmons (1951) took the first major step in providing a description of the transitional region in a boundary layer. He proposed that transition occurred through the development of turbulent spots that were surrounded by laminar flow (Narasimha, 1985). Previously, transition was thought to be an abrupt, more or less two-dimensional discontinuity of laminar into turbulent flow (Mayle, 1991). In 1935, Prandtl said, “In actual fact the transition is accomplished in a region of appreciable length and moreover experiments show that the position of the point when turbulence commences oscillates with time” (Narasimha, 1985). In recent times, the concept of transition as a randomly intermittent laminar-turbulent flow has gained acceptance.

Mayle Transition Length Model

Based on experimental data for separated flow transition, Mayle (1991) suggested the following correlation for determining the transition onset point, x_t ,

$$(Re_x)_{st} = 1000 Re_{\theta_s}^{0.7} . \quad (3.36)$$

The Reynolds numbers, $(Re_x)_{st}$ and Re_{θ_s} , correspond to the Reynolds number between the point of separation and transition onset, and the momentum thickness Reynolds number at the point of separation, respectively, and are defined as

$$(Re_x)_{st} = U_s(x_t - x_s)/\nu_s , \quad (3.37)$$

$$Re_{\theta_s} = U_s\theta_s/\nu_s . \quad (3.38)$$

The above relations require that the conditions at the point of separation be known for predicting the point of transition onset. A second experimental correlation is provided by Mayle for determining the transition termination point, x_T ,

$$(Re_x)_{LT} = U_s(x_T - x_t)/\nu_s = 400Re_{\theta_s}^{0.7} . \quad (3.39)$$

Using the above relation, the length of the transition region, $x_T - x_t$, can be estimated. In the correlations provided above for Mayle's transition length model, x_s , x_t , and x_T represent streamwise distances.

The important features of separated-flow transition over a separation bubble are shown in Figure 3.1. As explained by Mayle (1991) in the upstream region, the laminar shear flow zone becomes unstable, which leads to the formation of turbulent spots and the onset of transition starts at this point. The unstable laminar shear flow is found between x_s and x_t . In the transition region, which lies between x_t and x_T , the turbulent spots grow to form fully developed turbulent flow towards the end of transition. The transition zone is usually characterized by having constant pressure. In the downstream region the flow reattaches as turbulent at x_r .

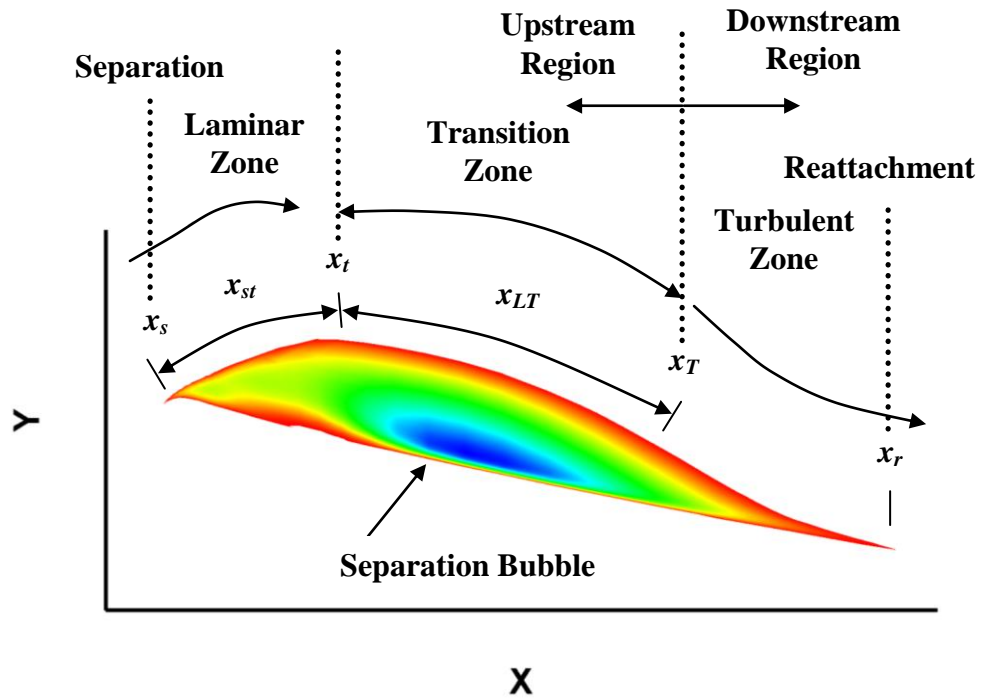


Figure 3.1: Schematic diagram in a transitional flow with a separation bubble (Mayle, 1991)

Dhawan and Narasimha Transition Model

To account for transition in the boundary layer, Dhawan and Narasimha (1958) proposed a correlation based on experimental data for evaluating the intermittency factor, γ_I , given by

$$\gamma_I(x) = 1 - \exp \left[-0.412 \left(\frac{x - x_t}{x_{75} - x_{25}} \right)^2 \right]. \quad (3.40)$$

The terms x_{25} and x_{75} in the above equation are the locations where the intermittency factor is equal to 0.25 and 0.75, respectively. Using the value of intermittency factor at x_T ($\gamma_I(x_T) = 0.99$) and the length of the transition region, $x_T - x_t$, the distance $x_{75} - x_{25}$ can be calculated. As can be seen from this discussion one obvious weakness of the DN transition model is that the transition onset and length must be known a priori. Hence, transition length and onset models, like the Mayle model, are required to use the DN transition model. However, it does allow parametric investigations of the influence of transition onset and length on the flow field.

Inside the transition region there are fluctuations between laminar and turbulent flow due to passage of turbulent spots. These fluctuations are quantitatively described by the intermittency factor, γ_I , which represents the fraction of time any point spends in turbulent flow.

Along the transition length, the intermittency function has only streamwise dependency; normal-to-wall effects are assumed to have only a secondary influence on transition (Dhawan and Narasimha, 1958). As indicated by Dhawan and Narasimha (1958), the $\gamma_I(y)$ variation depends on the shape of the turbulent spots and is essential only for studies relating to the detailed structure of the turbulent motion associated with the

spots. From an implementation point of view, the model is quite easy to use, and can be combined with any turbulence model.

The intermittency factor, γ_I , thus calculated is then multiplied by the turbulent viscosity, μ_t , in the transition region of the flow to blend the flow from laminar to turbulent. This modified turbulent viscosity is then used to calculate the Reynolds stress terms that are appropriate for the transition region in the computational model. This will be covered in more detail in the next chapter.

Chapter Four

Computational Model and Data-Theory Correlation

NPHASE

NPHASE is the computational model used in this investigation. NPHASE is a two-dimensional compressible turbomachinery flow simulator that solves nonlinear steady and unsteady flow fields for turbomachinery geometries using sheared H-grids. Originally developed by the Engineering Research Center at Mississippi State University (Swafford et al., 1994), NPHASE is capable of computing both viscous (using the thin-layer Reynolds Averaged Navier-Stokes equations) and inviscid (Euler) flows.

Initially, there was no transition model, and the Baldwin-Lomax (1978) algebraic turbulence model was used for viscous flow computations. At present, the Spalart-Allmaras (1994) turbulence model, the Solomon, Walker, and Gostelow (1996) transition model, Dhawan and Narasimha (1958) transition model, and Mayle (1991) transition length model have been implemented in the code. Different transition onset models (fixed, Michel (1951), Suzen et al. (2003), Steelant and Dick (2001), and Praisner and Clark (2004)) have also been added to NPHASE. In addition, the capability to specify the value of inlet turbulent viscosity, μ_t , and also use different initial condition values for the Spalart-Allmaras model, has been implemented in the code. Moreover, the code now has the capability to start with the Baldwin-Lomax model and then continue the computations with the Spalart-Allmaras model using the turbulent viscosity computed with the Baldwin-Lomax model. Furthermore, it is now possible to use different formulations for the turbulence production term in the Spalart-Allmaras model. The Spalart-Allmaras turbulence model has also been sensitized to system rotation/streamline curvature effects

using the FCR correction of Hellsten (1998). Both gust (Ayer and Verdon, 1994) and oscillating airfoil unsteady aerodynamics can be calculated. For oscillating airfoil unsteady flow simulations, a time marching method with a deforming computational mesh that uses multiple airfoil passages to satisfy periodicity is used.

Interaction of Transition Model with Flow Solver

There are two main parts to computing transitional flows in RANS codes: 1) determining the transition onset point, and 2) predicting the length of the transition zone. Current turbulence models are not able to perform these two tasks reliably. Hence, the approach taken in this research is to use a transition onset model to determine the transition onset location and a transition model to predict the transition zone length. Within the transition zone the intermittent behavior of the transitional boundary layer is incorporated into existing turbulence models. This is accomplished by using an intermittency factor. Once calculated, the intermittency factor is multiplied by the turbulent eddy viscosity to get an effective eddy viscosity.

$$\mu_{eff}(x, y) = \gamma_I(x)\mu_t(x, y)$$

The effective viscosity is then used in the place of the turbulent eddy viscosity. The turbulent viscosity is calculated using the Spalart-Allmaras turbulence model and the intermittency is determined using the Dhawan and Narasimha model in this investigation.

The turbulence model is applied starting at the leading edge of the airfoil. In the laminar region, the intermittency factor is set to zero. In the transition zone, the intermittency factor varies between 0 and 1 and is determined by the transition length model. The turbulent flow region has an intermittency factor of 1. Figure 4.1 presents an

example of the variation of the intermittency factor as the flow transitions from laminar to turbulent over the suction surface of the NASA-PW airfoil.

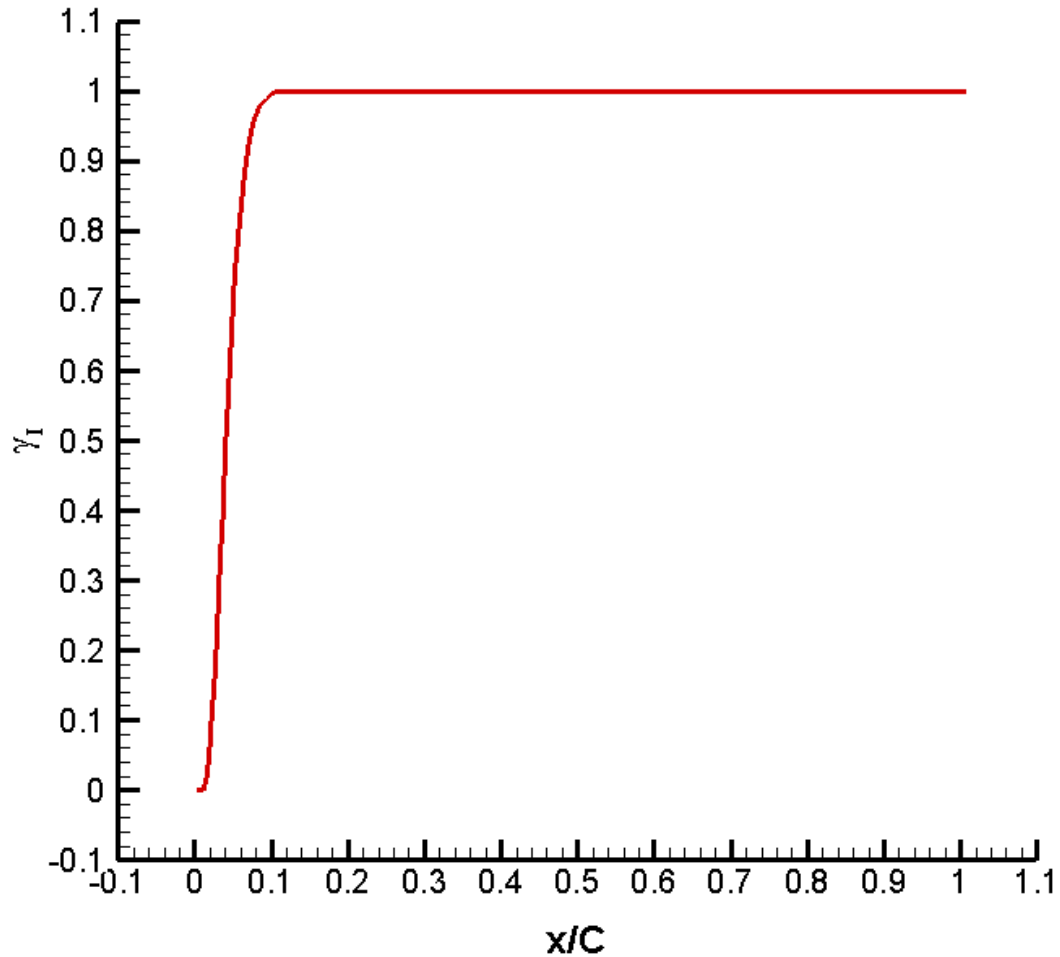


Figure 4.1: Example of the variation of the intermittency factor in the transition region over the suction surface of the NASA-PW airfoil (193 x 101 Grid)

Data-Theory Correlation

In this section several relationships concerning the computed quantities used to represent the solution for flat plate studies and the NASA-PW airfoil will be presented.

Two non-dimensional quantities of interest in this investigation are the skin-friction coefficient and lift coefficient, which are denoted by C_f and C_L , respectively. The skin-friction and lift coefficients are calculated in the computer code using the equations given below.

$$C_f(x) = \frac{\tau_0(x)}{1/2 \rho_\infty U_\infty^2}$$

$$C_L = \frac{L}{1/2 \rho_\infty U_\infty^2 A}$$

The skin-friction coefficient describes the change in the local frictional drag over the surface. The lift coefficient is a convenient measure that gives the lift generated by an airfoil relative to the dynamic pressure of the fluid flow around the airfoil.

Flat Plate

To validate the implementation of the inlet turbulent viscosity boundary conditions and modifications to the turbulence production term in the SA model, flat plate turbulent boundary layer data was used. A significant amount of data and correlations are available for flat plate turbulent boundary layers. Two sources are used in this research.

The first data source is the incompressible turbulent flat plate boundary layer data of Wieghardt and Tillmann (1951), which has been cited by Coles and Hirst (1968). The Wieghardt and Tillmann experimental data as tabulated by Coles and Hirst can be found in Slater (2008); this benchmark experimental data is tabulated in Appendix A for completeness. The data of interest in this research are the skin-friction along the surface of the plate and the velocity profile at the location where the Reynolds number is 10.3

Million. The skin-friction is represented in non-dimensional form using the skin-friction coefficient.

The turbulent skin-friction coefficient correlation based on experimental data as given by White (1974), and presented below, is used as the second data source.

$$C_f = 0.026(Re_x)^{-(1/7)}$$

The T3A experimental data from the series of test cases compiled by Savill (1993) is used as the data source for correlating the flat plate laminar boundary layer flow and transitional boundary layer flow calculations. In addition to the experimental data by Savill, skin-friction coefficient correlation obtained from the Blasius (1908) solution for laminar boundary layers over a flat plate is used, which is presented below.

$$C_f = \frac{0.664}{\sqrt{Re_x}}$$

The turbulent velocity profile is given in terms of non-dimensional variables, u^+ and y^+ ,

$$u^+ = \frac{\bar{u}}{u_*},$$

$$y^+ = \frac{yu_*}{\nu}.$$

This turbulent velocity profile has three regions near the wall: 1) Viscous Sub-layer, 2) Overlap Layer or Logarithmic Layer, and 3) Outer Layer. Throughout the inner region of the boundary layer next to the wall, the velocity distribution can be written as

$$\frac{\bar{u}}{u_*} = f\left(\frac{yu_*}{\nu}\right),$$

or

$$u^+ = f(y^+).$$

This is known as the “law of the wall.” Inside the viscous sub-layer, which is right next to the wall, the shear due to viscous forces is dominant and the velocity distribution is linear, and is given by

$$u^+ = y^+ .$$

The overlap layer has a logarithmic velocity distribution, which smoothly matches the velocity distribution profile of the viscous sub-layer in the inner region and that of the outer layer. The logarithmic law that governs the velocity profile in the overlap layer is given by

$$u^+ = \frac{1}{\kappa} \ln y^+ + B ,$$

where $\kappa = 0.41$ and $B = 5.0$, or $\kappa = 0.4$ and $B = 5.5$. The outer layer is governed by what is known as the “velocity defect law,” where there is a deviation in the mean flow velocity, \bar{u} , from the free stream velocity, V . This outer layer velocity distribution is written as

$$\frac{V - \bar{u}}{u_*} = F\left(\frac{y}{\delta}\right) .$$

In addition to the Wieghardt and Tillmann experimental data for the turbulent velocity profile, Spalding’s (1961) wall law formula is used, which is accurate throughout the inner region of the boundary layer including the logarithmic layer, and is presented below.

$$y^+ = u^+ + e^{-\kappa B} \left[e^{\kappa u^+} - 1 - \kappa u^+ - \frac{(\kappa u^+)^2}{2} - \frac{(\kappa u^+)^3}{6} \right] ,$$

where $\kappa = 0.4$ and $B = 5.5$ have been used in the present work.

NASA-PW Airfoil

The computed solution for the pressure coefficient, C_p , obtained for turbulent flow and transitional flow simulations over the NASA-PW airfoil is compared with the experimental results from NASA-GRC TFC (Buffum et al., 1998). The equation used to compute C_p is shown below.

$$C_p = \frac{p_\infty - p}{\rho_\infty U_\infty^2}$$

It is a non-dimensional variable that gives the relative pressure of the fluid at a given point in the flow field.

Computational Procedures

For computing transition, the approach used in this work involves: 1) obtaining a fully turbulent solution on the whole computational domain, and 2) restarting the fully turbulent solution with the transition model activated. In this investigation, the fully turbulent solution is obtained using the SA turbulence model. For transition calculations, the DN transition model is used simultaneously with the SA model. In addition, as discussed above, fully turbulent solutions can be generated by computing the turbulent viscosity with the BL turbulence model and then restarting this solution using the SA turbulence model. This procedure is used to speed up solution convergence of the SA turbulence model by providing the SA model with a better initial condition.

Chapter Five Results

In this chapter, laminar, turbulent, and transitional flow results are presented for a flat plate airfoil, plus turbulent and transitional flow results are presented for NASA-PW airfoil geometry. In addition, studies have been done for the following cases: 1) the effect of varying the values of inlet turbulent viscosity, 2) the effect of adopting different methodologies in formulating the production term in the Spalart-Allmaras model, 3) including the effect of streamline curvature correction (FCR correction), and 4) restarting the solution from the Baldwin-Lomax model with the Spalart-Allmaras model to speed up convergence.

Flat Plate

Flat plate test cases are used to validate the implementation of the inlet turbulent viscosity boundary conditions, sensitivity of SA model to streamline curvature, and the modification of the turbulent production term in the SA model, which is used in NPHASE. Two distinct cases were utilized for the validation process. Since NPHASE uses the compressible form of the governing equations without preconditioning, the inlet Mach number was set to 0.3 for these simulations.

Solutions are presented for laminar, turbulent, and transitional flow. Grid independence of the solutions is demonstrated by computing the flow on grids of different density. The experimental data from Wieghardt and Tillmann (1951), the skin-friction coefficient correlation based on experimental data as given by White (1974), and the analytic formula for $u^+ - y^+$ as derived by Spalding (1961) are used in this research for

validating the fully turbulent flow computations. For laminar flow and transitional flow computations the T3A experimental data from the series of test cases compiled by Savill (1993) are used. In addition, the laminar flow calculations are also compared with the skin-friction coefficient correlation obtained from the Blasius (1908) solution for laminar boundary layers over a flat plate.

The incompressible flat plate turbulent boundary layer with zero pressure gradient experimental data of Wieghardt and Tillmann (1951) used a chordal Reynolds number of 12.8 Million. The velocity profile experimental data was correlated with the computations at the location on the flat plate where the Reynolds number was 10.3 Million.

Flat plate simulations with a Mach number of 0.6, which is closer to the value used for the NASA-PW airfoil case were also conducted, and the results are presented in the Appendix B. The chordal Reynolds number used for these calculations was 3 Million.

Laminar Flow

Laminar flow calculations were done on a coarse grid and a dense grid of size 161 x 82 and 238 x 164, respectively, and correlated with the T3A experimental data compiled by Savill (1993). The computations were conducted at an inlet Mach number of 0.3, chordal Reynolds number of 1 Million, and chordal incidence angle of zero degrees. These laminar flow computations are essential from the standpoint of addressing the importance of predicting the transitional flow as the flow transitions from laminar to turbulent. Figure 5.1 shows the lift coefficient convergence history for the laminar calculation. As seen in the figure, the lift coefficient has only extremely small fluctuations in amplitude after the initial starting transient. Figure 5.2 shows the density

residual history for the laminar calculation. The density residual levels out at a value less than 10^{-7} towards the end of the calculation indicating, along with the lift coefficient, the convergence of the solution. The solution convergence history for the 161 x 82 grid is similar to the 238 x 164 grid results displayed in Figures 5.1 and 5.2.

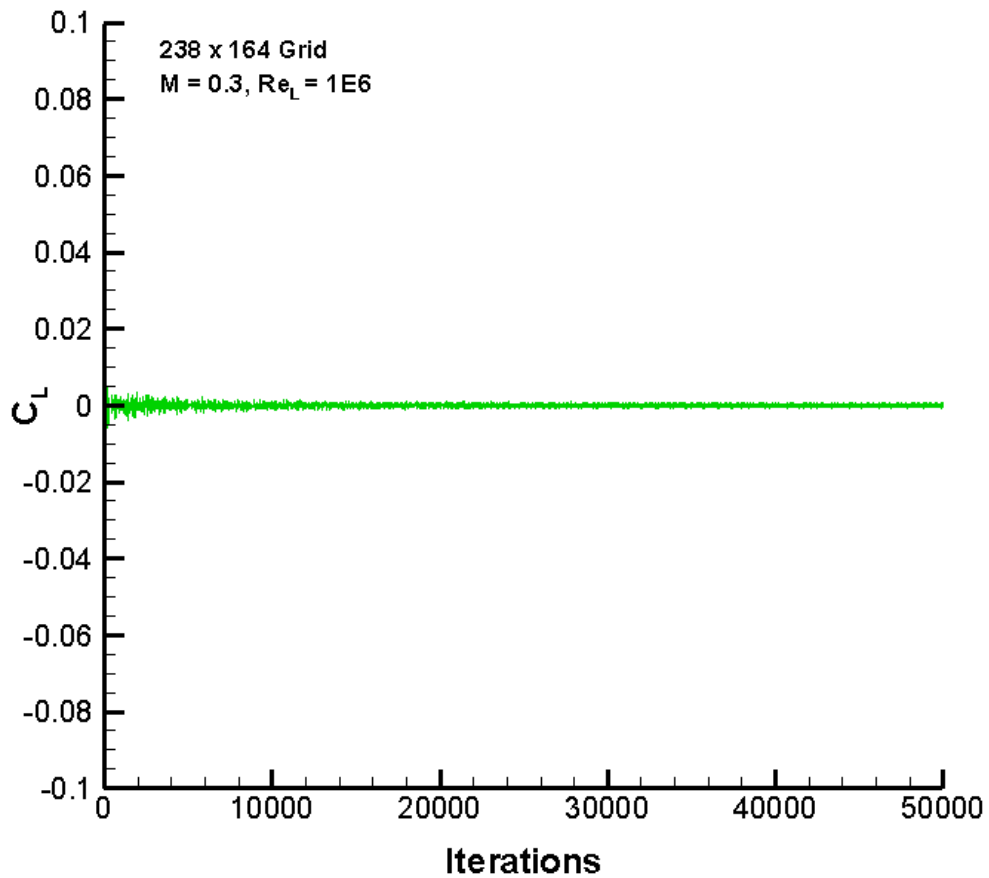


Figure 5.1: Example of flat plate lift coefficient convergence history for laminar flow

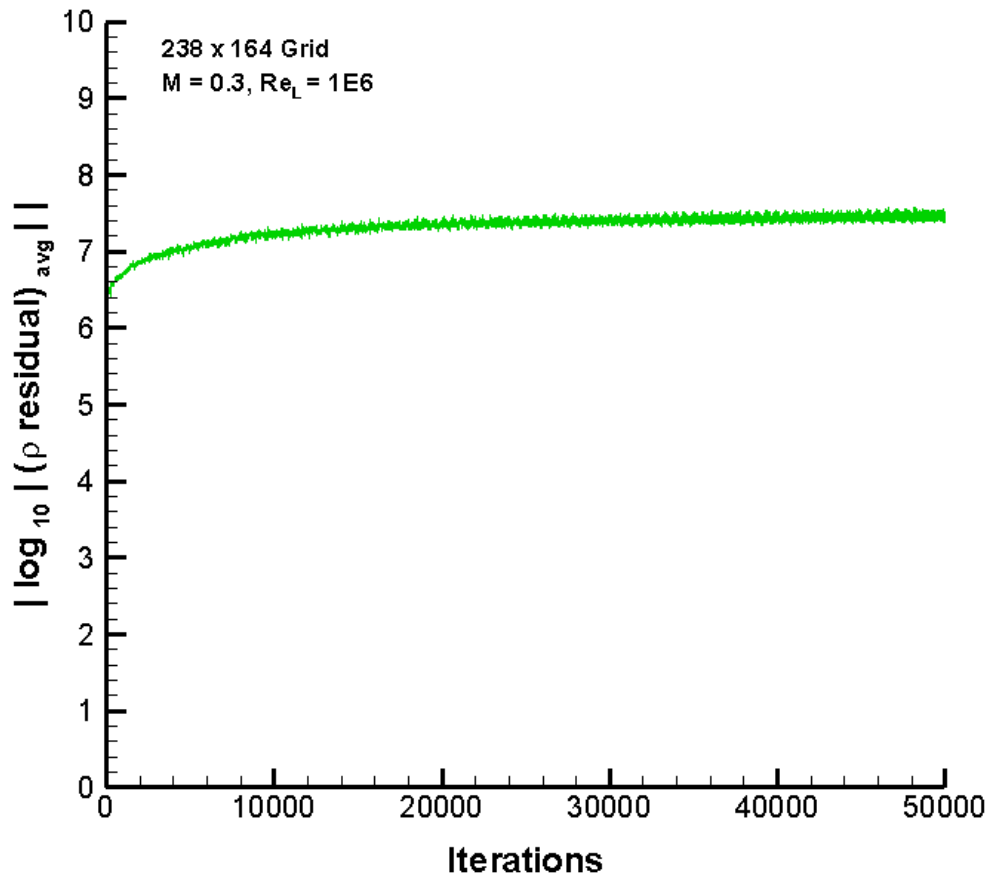


Figure 5.2: Example of the absolute value of the average density residual convergence history for laminar flow over a flat plate airfoil

The skin-friction coefficient for the laminar solution on the flat plate airfoil is presented below in Figure 5.3. The local Reynolds number, Re_x , represents the distance along the plate. A chordal Reynolds number of 1 Million was chosen to be consistent with the computations performed for transitional flow calculations and more details will be provided in the Transition section below. The solutions obtained using a coarse grid of size 161 x 82 and a denser grid of size 238 x 164 demonstrate the grid independence of the laminar flow solution. Also, the skin-friction on the pressure surface and the suction

surface for both the grids are the same as both the surfaces are identical to each other. As illustrated in Figure 5.3, the results from the computation are compared with the Blasius solution and experimental data. The computations have very good agreement with the Blasius solution. The trends exhibited by the computations and the Blasius solution are the same, which indicate that the C_f reduces downstream of the leading edge over the flat plate airfoil for laminar flow. The experimental data clearly shows the transition region where the skin-friction increases as the flow undergoes transition from laminar to turbulent. The laminar computations agree well with the experimental data up to the point where transition begins and the flow ceases to be laminar. From the skin-friction results it can be clearly seen that the laminar computations on both the grids fail to predict and correlate with the experimental data in the transition and turbulent flow regime of the flat plate airfoil. Moreover, a huge difference is seen between the skin-friction for laminar flow and turbulent flow after transition has occurred. This suggests that predicting the transition region accurately is essential from a basic fluid physics point of view, as well as a designer of turbomachine blades.

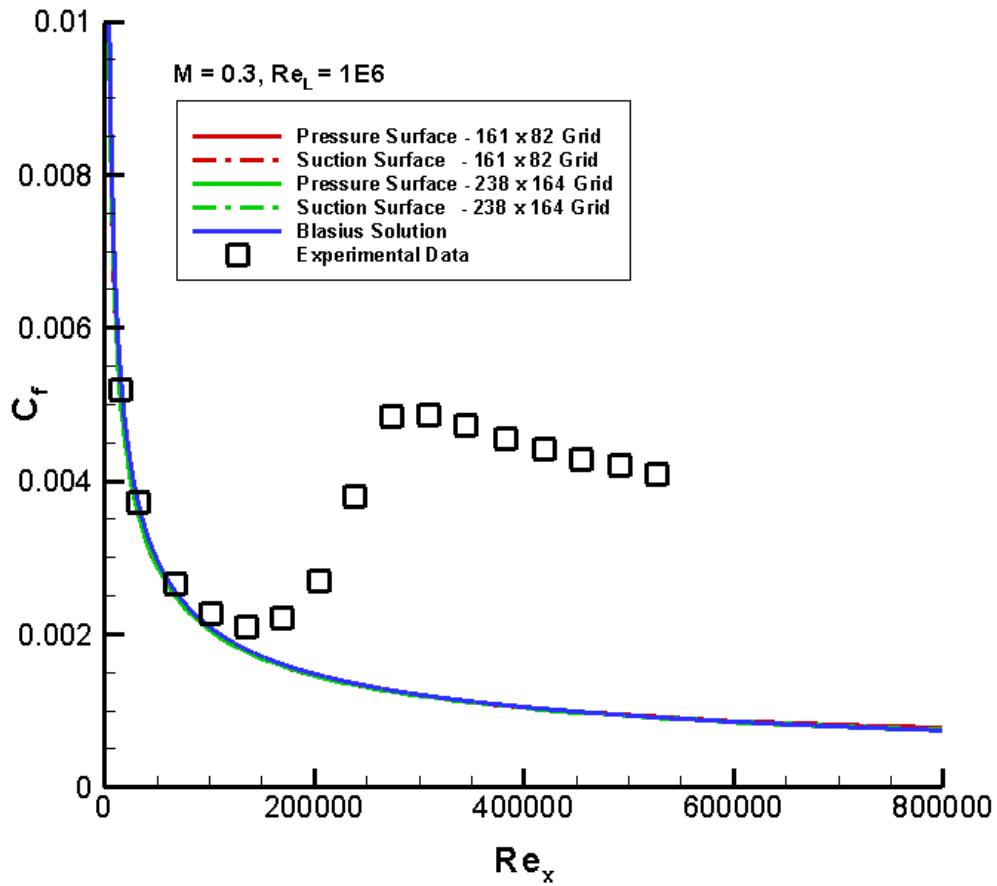


Figure 5.3: Flat plate skin-friction coefficient for laminar flow

Turbulent Flow

Figures 5.4 and 5.5 below give the variation of the lift coefficient and the average density residual with the number of time steps for fully turbulent flow. The indicators that solution has converged are: 1) extremely small fluctuations in amplitude of the C_L , and 2) the absolute value of the average density residual is greater than 7.5. The solution convergence indicators for the 161 x 82 grid were similar to that of the 238 x 164 grid.

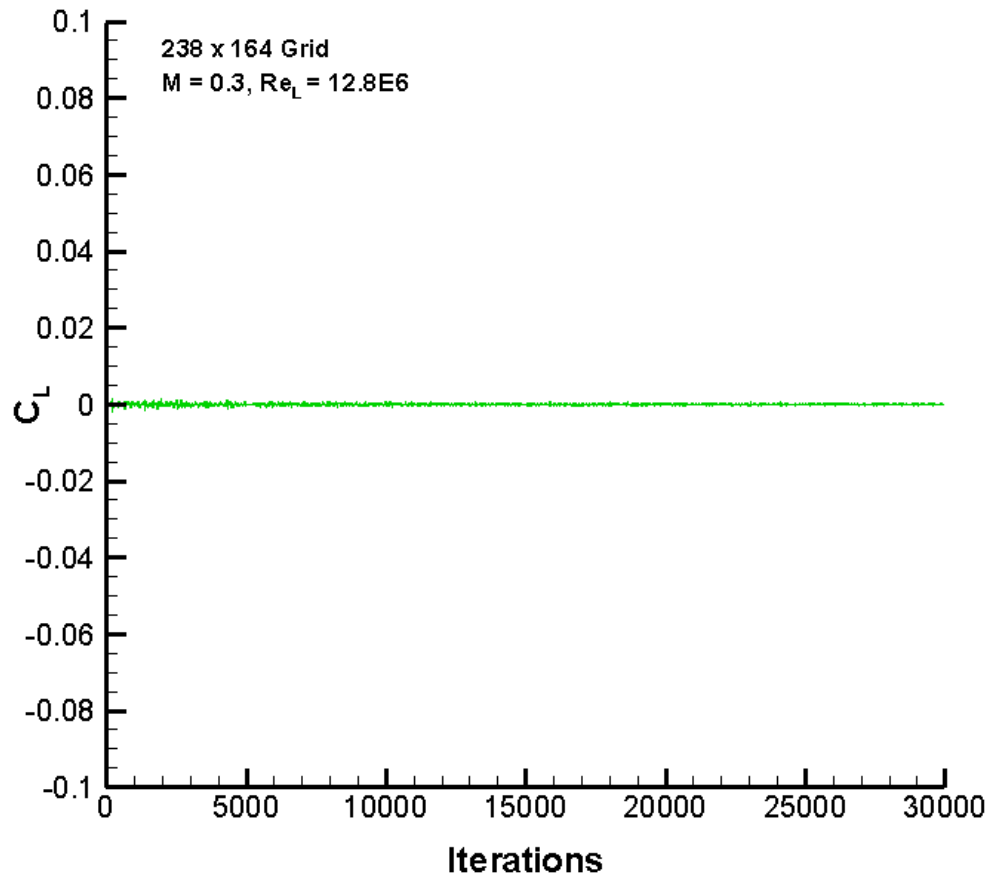


Figure 5.4: Example of flat plate lift coefficient convergence history for fully turbulent flow

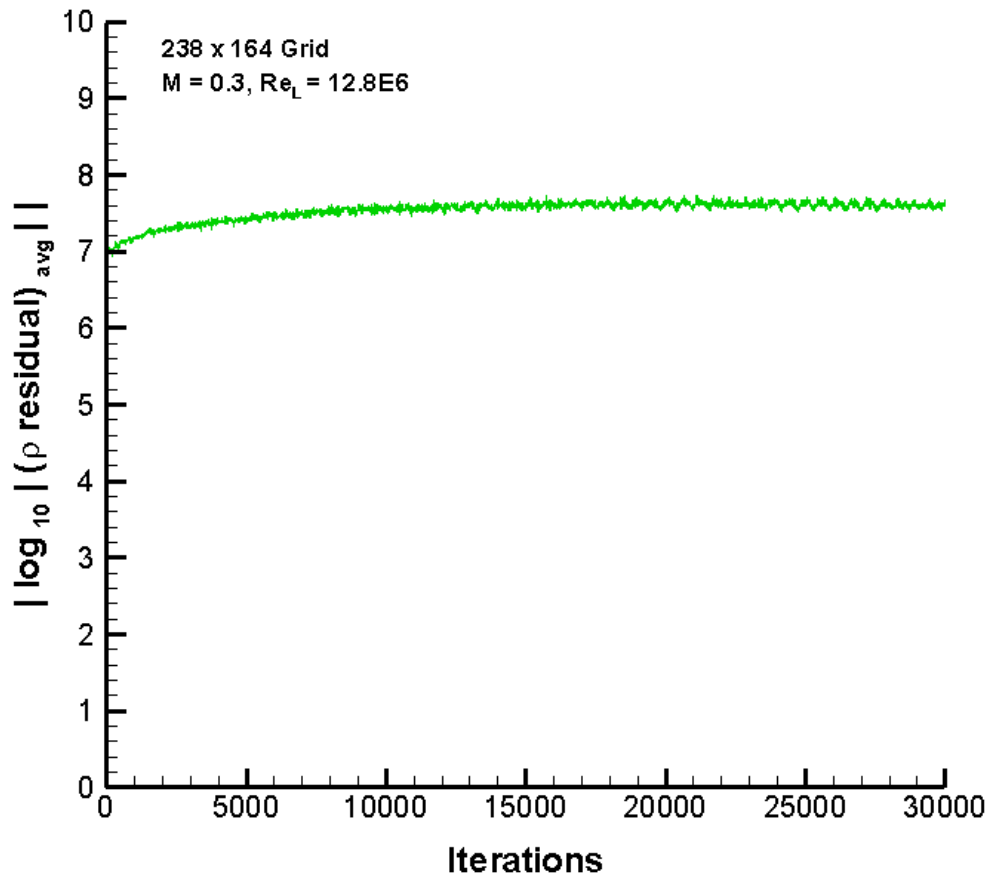


Figure 5.5: Example of the absolute value of the average density residual convergence history for fully turbulent flow over a flat plate airfoil

Figure 5.6 shows the variation of the skin-friction at Mach 0.3 with a chordal Reynolds number of 12.8 Million for the flat plate airfoil computed on two different grids of size 161 x 82 and 238 x 164 that demonstrates grid independence of the solution. The C_f curves for the suction and pressure surfaces are identical for each grid. This is because for the flat plate airfoil, the geometry of both the suction and pressure surfaces is identical to each other. In Figure 5.6 and in subsequent fully turbulent skin-friction coefficient figures, the curve denoted by “Theoretical Data” represents the skin-friction coefficient

correlation by White (1974). The trend of the computations, theoretical data curve, and the experimental data are exactly alike, which indicates that turbulent flat plate friction drops slowly in the streamwise direction. The computations are slightly lower than the theoretical skin-friction data. Good agreement was obtained between the computations and the experimental data of Wieghardt and Tillmann (1951). For these computations the inlet turbulent viscosity was fixed at 0.009, vorticity based production formulation was used in the SA model, and streamline curvature correction was not used.

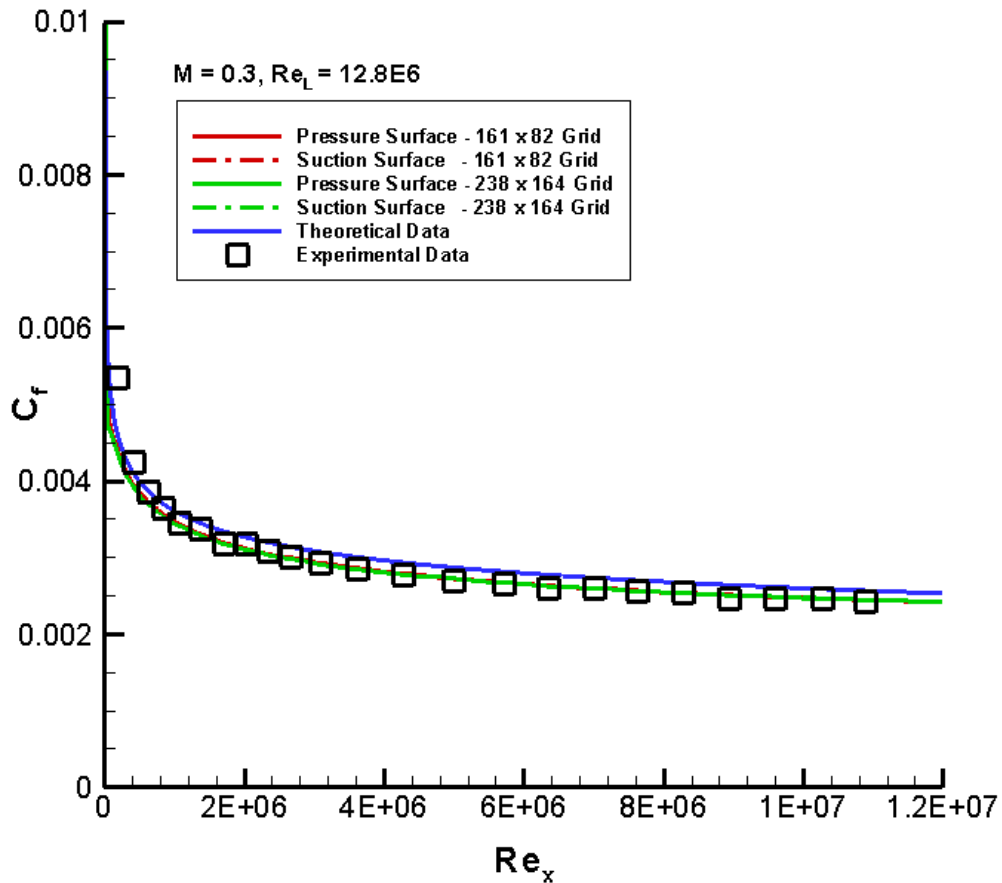


Figure 5.6: Flat plate skin-friction coefficient for fully turbulent flow

Figure 5.7 presents the variation of u^+ with y^+ . The velocity profiles from these computations were acquired at 80% chord length on the flat plate airfoil corresponding to a Reynolds number of 10.3 Million. The results are identical to each other and again demonstrate the grid independence of the solutions. As already discussed before under the section “Data-Theory Correlation” in Chapter 4, the turbulent velocity profile of Figure 5.7 has three regions near the wall: 1) Viscous sub-layer, 2) Overlap layer or Logarithmic layer, and 3) Outer layer. In the figure, the viscous sub-layer is seen as a curved profile near the wall where the velocity distribution is linear, which merges into a straight line for the logarithmic layer through what is known as the buffer layer, and again curves for the outer layer before the velocity distribution becomes flat with a constant u^+ value in the free stream region where the velocity is unchanged due to the flow being largely undisturbed and inviscid.

The computations show a good agreement with the Spalding’s formula up to the logarithmic overlap region and deviates slightly as the outer layer is approached. Excellent correlation is seen between the computations and the experimental data in the logarithmic layer and the outer layer. The Spalding’s formula $u^+ - y^+$ curve does not curve over as the free stream approaches because it is simply a mapping of u^+ to y^+ and indicates the extension of the logarithmic overlap region.

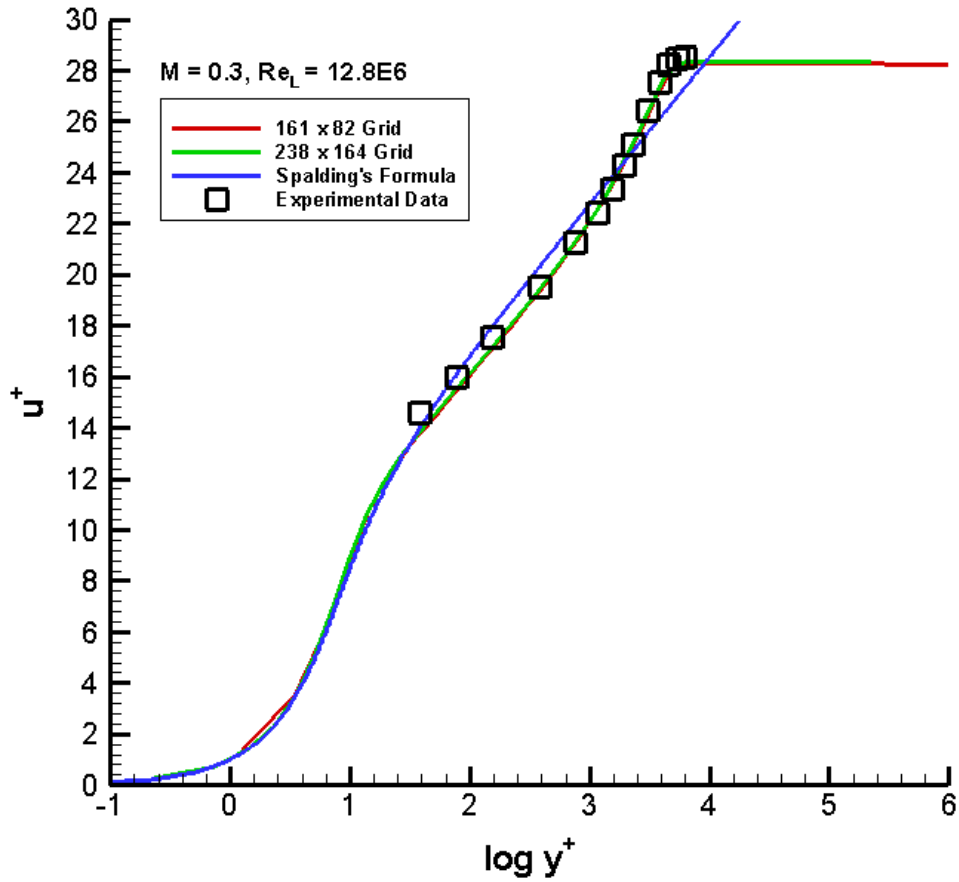


Figure 5.7: Flat plate velocity distribution for fully turbulent flow

Inlet Turbulent Viscosity and Initial Condition Study

The skin-friction coefficient variation is presented below in Figure 5.8 for flow over the flat plate airfoil surface at Mach 0.3 with a chordal Reynolds number of 12.8 Million using a coarse grid of size 161 x 82 for different inlet turbulent viscosity values and correspondingly different initial condition values of the modified turbulent viscosity in the SA model, $\tilde{\nu}$. In these computations the vorticity based production formulation was used and the streamline curvature correction was not used. The results are identical over the flat plate airfoil surface. This indicates that inlet turbulent viscosity and also the

different initial conditions do not have a significant effect on the skin-friction. This is exactly what is expected since the transition capability of the SA model is not activated.

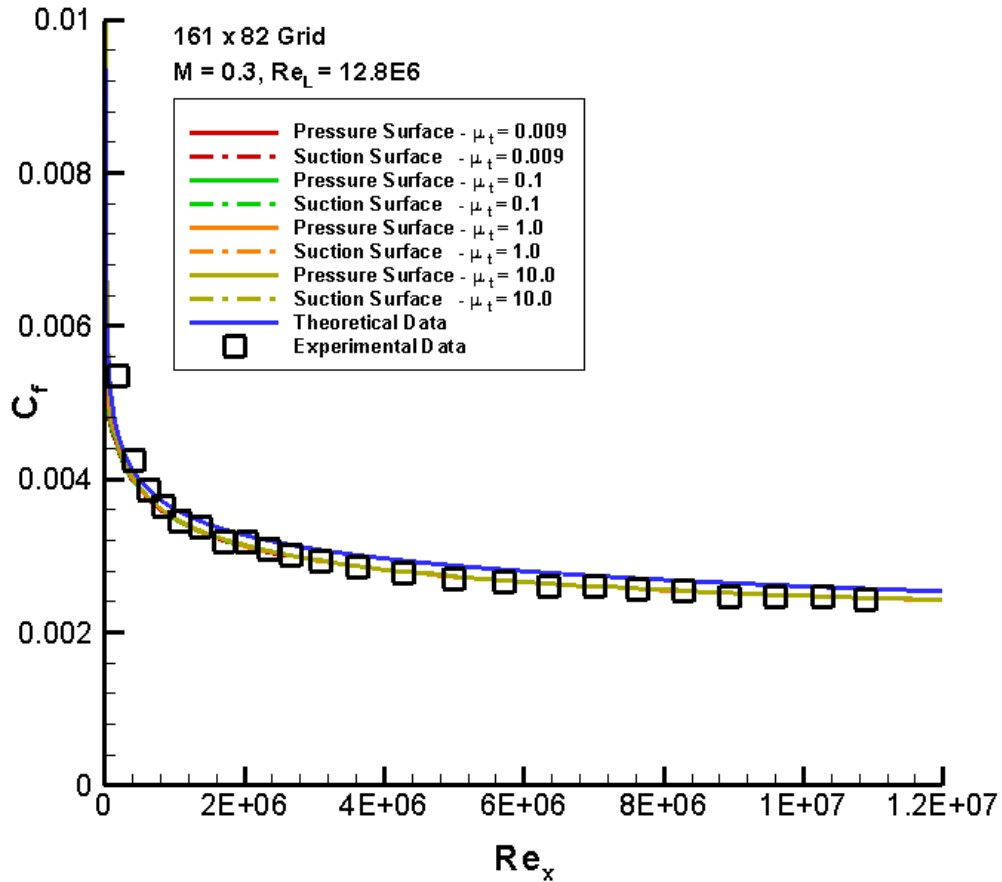


Figure 5.8: Flat plate skin-friction coefficient for fully turbulent flow with different values of the inlet turbulent viscosity and initial conditions

The variation of u^+ with y^+ is presented below in Figure 5.9 at 80% of the chord length, which corresponds to a Reynolds number of 10.3 Million at Mach 0.3 for the coarse grid of size 161 x 82 with different inlet turbulent viscosity values and corresponding different initial condition values of $\tilde{\nu}$. Changing the inlet turbulent

viscosity and starting out the computations with different initial conditions did not have any appreciable change in the computed u^+ values.

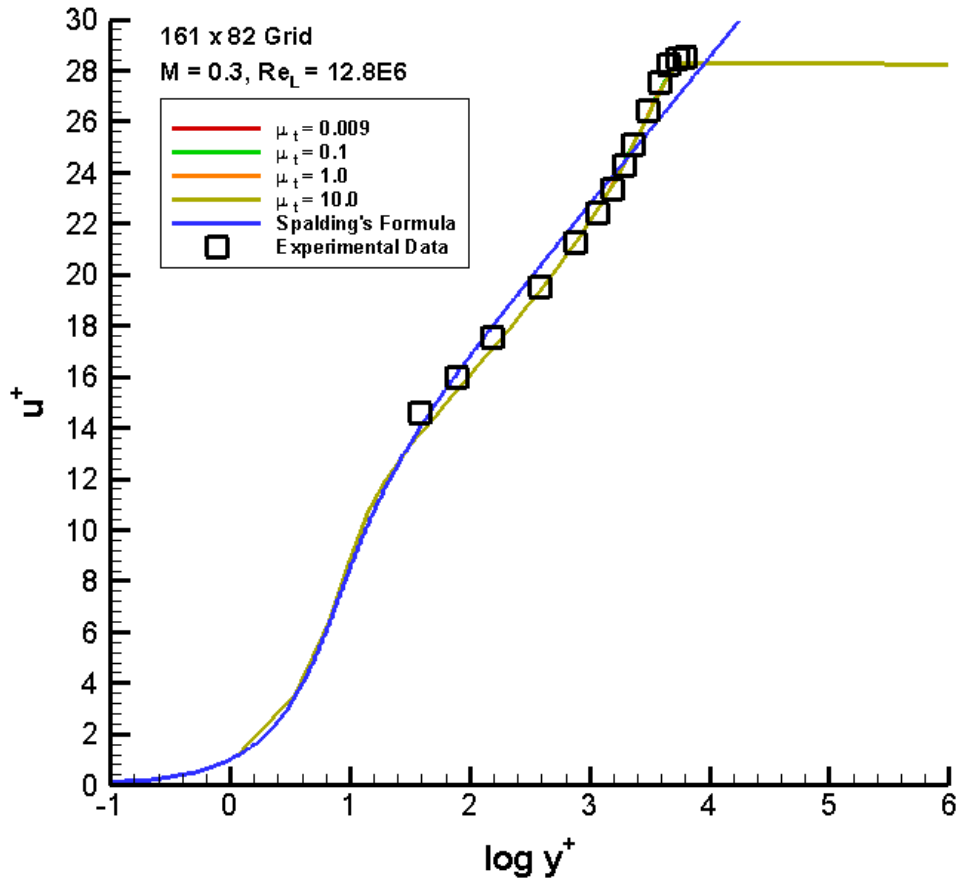


Figure 5.9: Flat plate velocity distribution for fully turbulent flow with different inlet turbulent viscosity values and initial conditions

Production Term Formulation Study in the Spalart-Allmaras Model

The production term in the SA model is modeled using the following three different methods: 1) Vorticity based, 2) Strain based, and 3) Strain-Vorticity based. Figure 5.10 shows the skin-friction on the surface of the flat plate airfoil at Mach 0.3, chordal Reynolds number of 12.8 Million for a coarse grid of size 161 x 82 using the

above mentioned methods to model the production term. For these computer simulations, the inlet turbulent viscosity was fixed at 0.009 and the streamline curvature correction was not used. There was no noticeable change observed for the flat plate airfoil case. To present the reasoning for this expected result, it should be noted that inside the boundary layer the variations across the boundary layer are much large than variations along the boundary layer in the streamwise direction. This implies that $\partial/\partial x \ll \partial/\partial y$. Moreover, $u \gg v$. Hence, $\partial u/\partial x$, $\partial v/\partial x$, and $\partial v/\partial y$ are much less than $\partial u/\partial y$. Therefore, inside the boundary layer, all the three formulations for the production term give the absolute value of $\partial u/\partial y$ as the scalar measure of the deformation tensor used in the production term of the SA model. This is the reason that there is no change in the skin-friction results for different production term formulations.

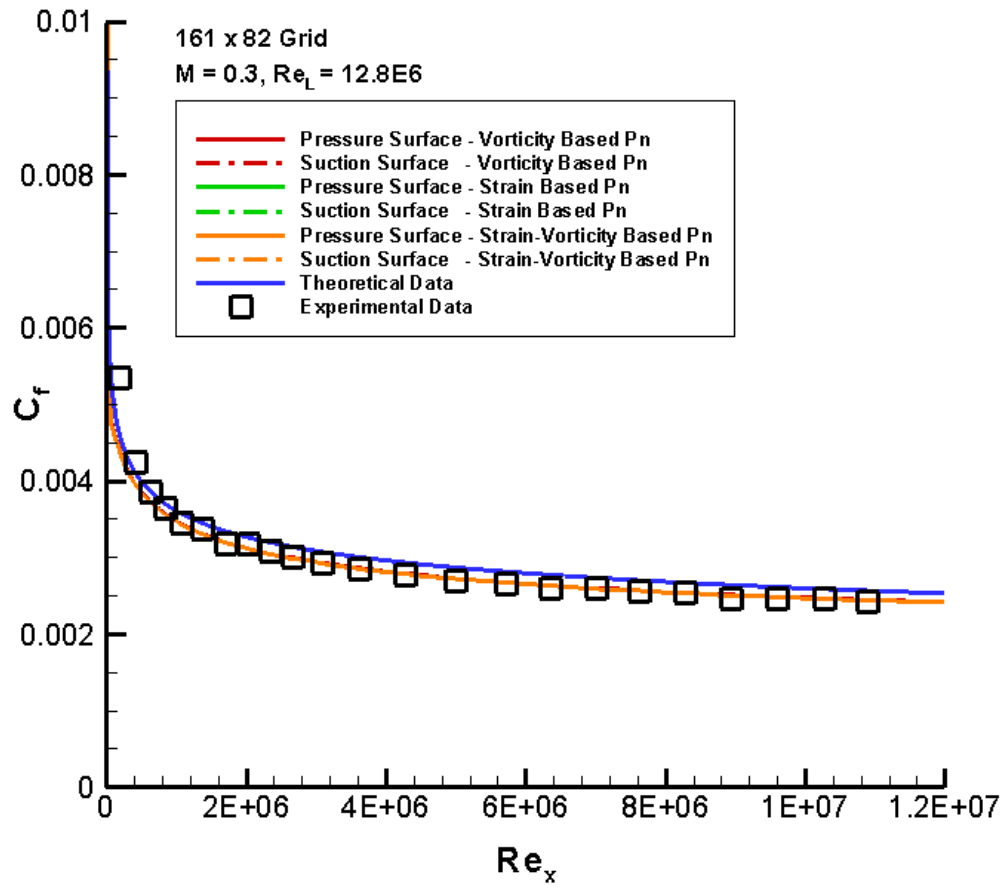


Figure 5.10: Flat plate skin-friction coefficient for fully turbulent flow using different production term formulations in the SA model

The corresponding $u^+ - y^+$ velocity distributions obtained by using the different methods to model the production term in the SA model are presented in Figure 5.11 for the coarse grid of size 161 x 82. Again, there was no appreciable change in the u^+ values for the reasons discussed above.

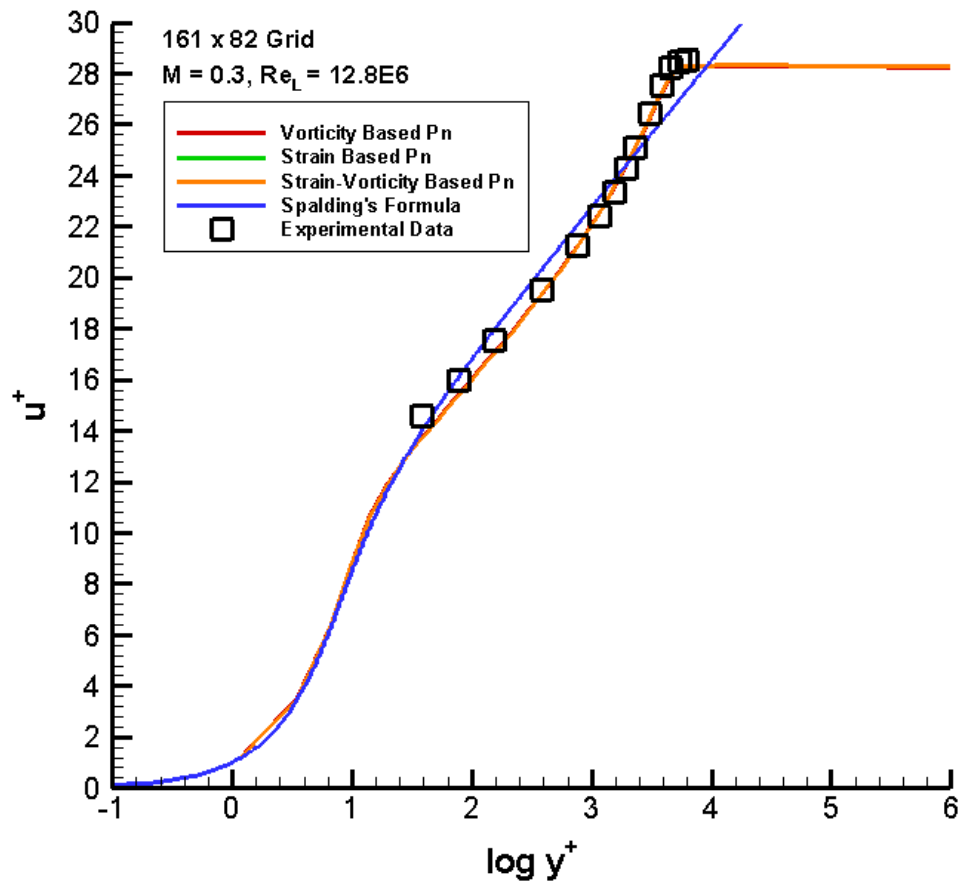


Figure 5.11: Flat plate velocity distribution for fully turbulent flow using different production term formulations in the SA model

Streamline Curvature Correction Study

The effect of the streamline curvature correction was studied for the flat plate airfoil case. The skin-friction coefficient variation on the flat plate airfoil surface is

presented in Figure 5.12 at Mach 0.3, chordal Reynolds number of 12.8 Million for the coarse grid of size 161 x 82 with and without the streamline curvature correction. For these computations, the inlet turbulent viscosity was fixed at 0.009, and vorticity based production formulation was used in the SA model. As expected, there was no difference in the two computed solutions. This is attributed to the fact that the flat plate airfoil does not have any curvature in its geometry and hence, there is no streamline curvature correction required for the flat plate case. Therefore, the F_{CR} term that accounts for the correction due to streamline curvature effects does not produce any change in the computed solution.

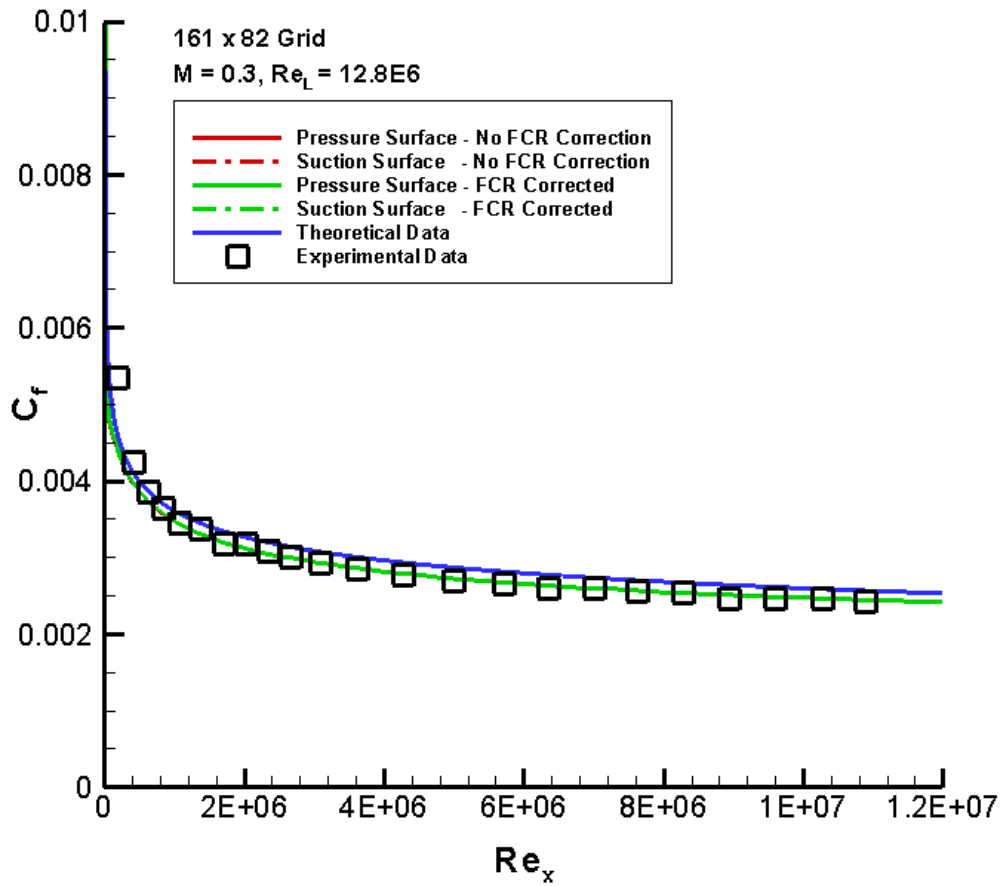


Figure 5.12: Flat plate skin-friction coefficient for fully turbulent flow with and without the streamline curvature correction

The corresponding turbulent velocity profile in terms of the inner variables u^+, y^+ is presented in Figure 5.13 for the coarse grid with and without the streamline curvature correction. There was no change in the computed solution when streamline curvature correction was used as compared to the solution where streamline curvature correction was not used for the reasons discussed above.

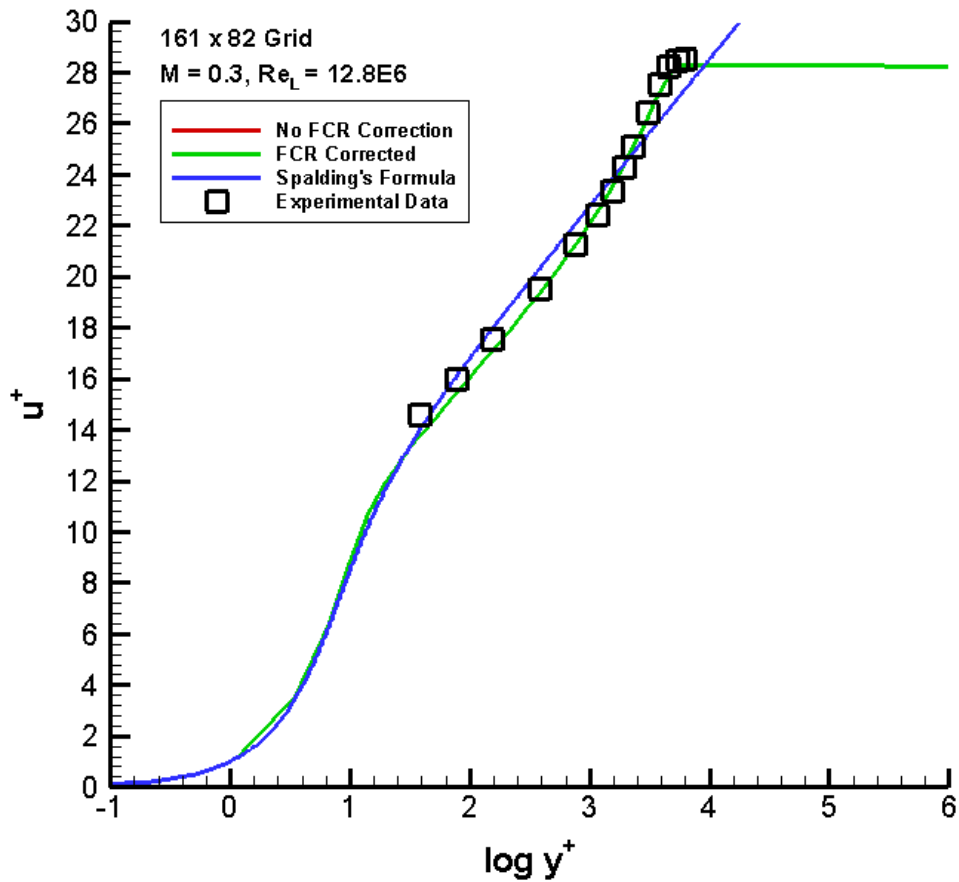


Figure 5.13: Flat plate velocity distribution for fully turbulent flow with and without the streamline curvature correction

Transition

Transitional flow computations were performed on the coarse grid of size 161 x 82 and the dense grid of size 238 x 164. The predictions from the computer code were correlated with the experimental data from Savill (1993). For the transitional flow calculations, solutions were first generated for fully turbulent flow using the SA model. These converged solutions were restarted with the DN transition model activated. The lift coefficient convergence history for the fully turbulent and transition calculations is shown

in Figure 5.14. Also shown is the average density residual convergence history in Figure 5.15. Transition solution is converged as indicated by: 1) extremely small fluctuations in amplitude of the lift coefficient, and 2) the average density residual value is less than $10^{-7.5}$. The solution convergence history for the 161 x 82 grid is similar to the 238 x 164 grid results.

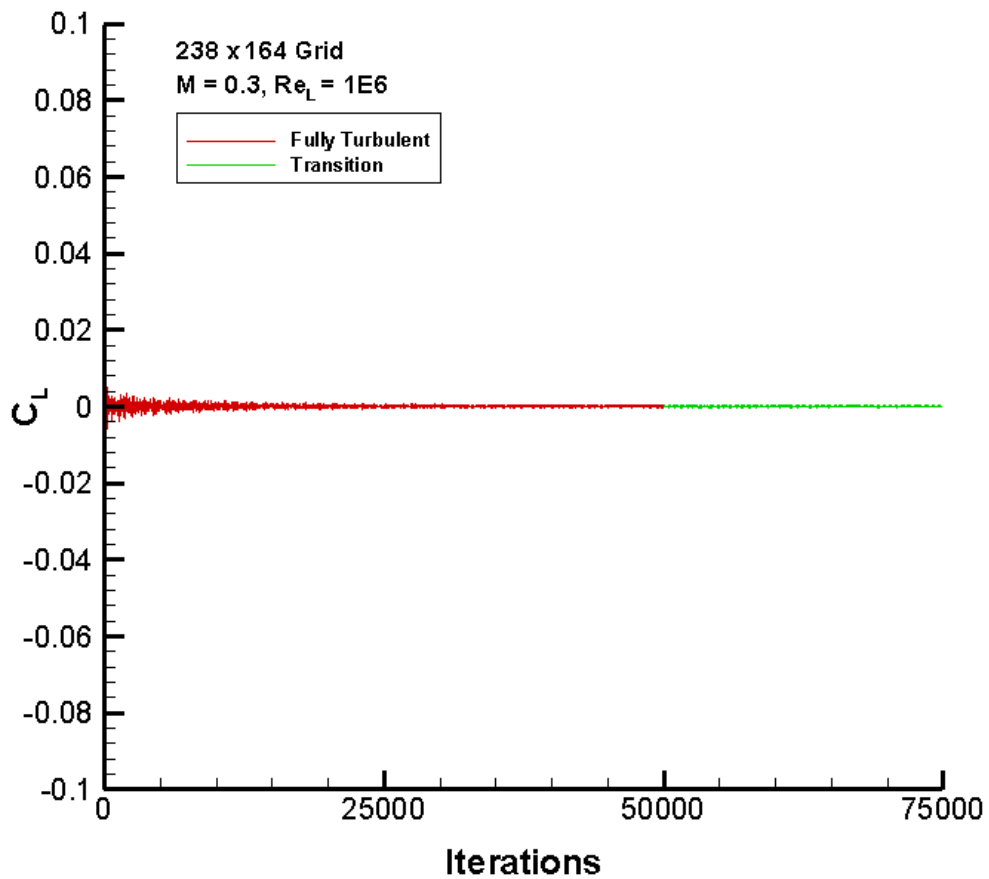


Figure 5.14: Example of flat plate lift coefficient convergence history for turbulent and transition flow

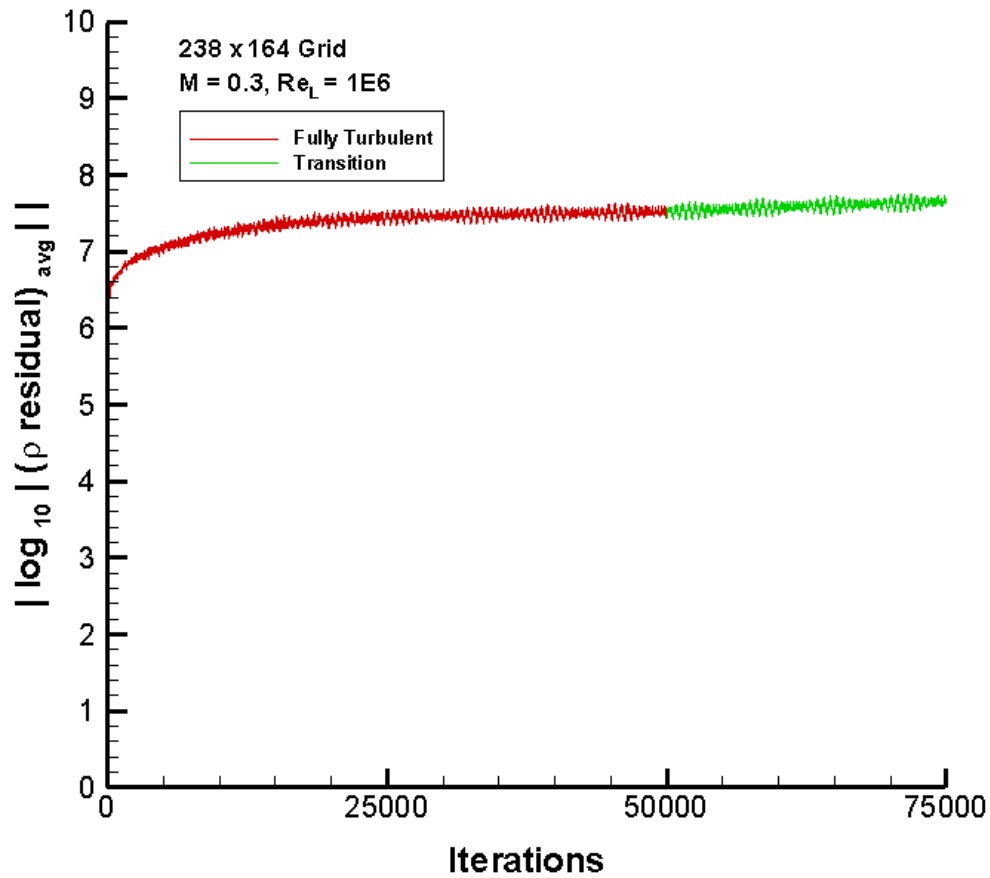


Figure 5.15: Example of the absolute value of the average density residual convergence history for turbulent and transition flow over a flat plate airfoil

From the transitional flow computations performed using the two flat plate grids, skin-friction coefficient results were calculated and correlated with the experimental data, which is presented in Figure 5.16. The computations were performed at a Mach number of 0.3 and chordal Reynolds number of 1 Million. As compared to the chordal Reynolds number of 12.8 Million that was used for the fully turbulent calculations, a much lower value of 1 Million was selected for computing the transitional flow. The reason for choosing such a low value is that for high values of chordal Reynolds number the

transition region will be shifted very close to the leading edge. Grid independence of the solutions is shown by computing the flow on the coarse grid of size 161 x 82 and the dense grid of size 238 x 164. On both the grids, the pressure surface was allowed to remain fully turbulent, and transition from laminar to turbulent flow was allowed to occur only on the suction surface of the flat plate airfoil. The difference in skin-friction coefficient is clearly seen between the laminar, transitional, and turbulent flows. Also, it can be seen that the turbulent skin-friction profile after transition on the suction surface merges with the fully turbulent skin-friction coefficient profile of the pressure surface towards the trailing edge of the flat plate. Transition onset and transition end points were selected on the suction surface and were fixed so as to give the best correlation with the experimental data points. This gave a value for $x_t = 0.19$ corresponding to an Re_x value of 190,000, and $x_T = 0.30$ corresponding to an Re_x value of 300,000. The experimental data decrease for $Re_x < 135,000$ in the laminar flow region. The skin-friction then increases as the flow undergoes transition to turbulent flow. Downstream of the transition region, the skin-friction coefficient decreases with further increase in Re_x , as expected for turbulent flow. The experimental data and computational predictions have the same trends. Moreover, the predicted increase in the skin-friction coefficient for both the grids reaches the peak value found for the experimental data. The two computational grids used have excellent agreement with each other. The transitional flow skin-friction coefficient results clearly emphasize the importance of predicting transition and how it affects the flow downstream of the transition onset point.

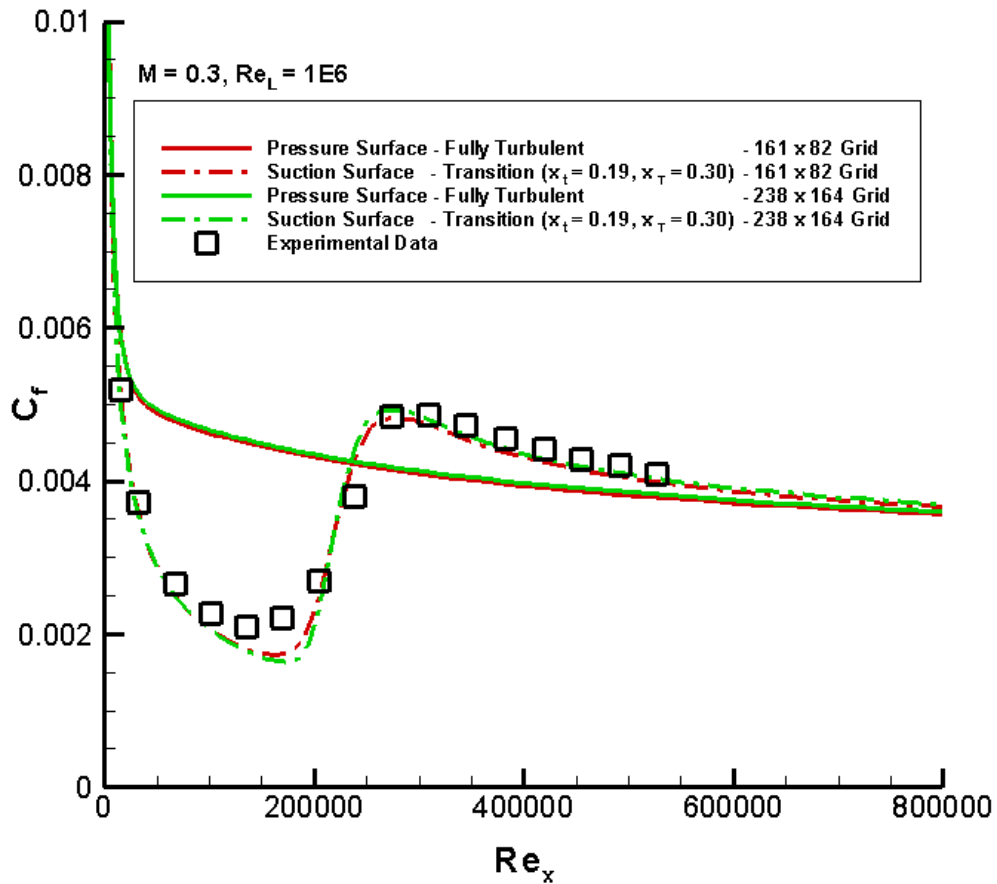


Figure 5.16: Flat plate skin-friction coefficient for transition from laminar to turbulent flow along the suction surface

NASA-PW

The experimental data used in this work were acquired at an inlet Mach number of 0.5 with a chordal Reynolds number of 0.9 Million. The same set of flow conditions are used for simulating the flow for a low incidence angle condition of 0° and a high incidence angle condition of 10° . The chordal incidence angles given by Buffum et al. (1998) were based on the cascade geometry; the actual inlet flow angles were not measured. To get better correlation with the experimental data the inlet chordal incidence

angle used in the simulations were 1° for the low incidence angle case and 7.5° for the high incidence angle case.

Grid convergence of the solutions is demonstrated by computing on a coarse grid of size 193×101 and a dense grid of size 363×201 . The cascade geometry used by Buffum et al. (1998) was presented in Chapter 2.

Low Incidence Angle Condition

The low incidence angle case will now be considered. At this condition, a small separation bubble was predicted on the suction surface of the airfoil near the leading edge region. As already mentioned above, in the experiments the flow angle was not measured and was concluded to be 0° from the geometry of the cascade. Therefore, for the purpose of computation, the inlet flow angle was varied until the best match with the chordwise surface steady pressure coefficient distribution was achieved. This resulted in a chordal incidence angle of 1° , which was used for all calculations presented below.

Fully Turbulent Flow

An example of the lift coefficient for the low incidence angle condition is shown in Figure 5.17 for fully turbulent flow over NASA-PW airfoil. A steady, non-oscillatory solution is obtained when the C_L becomes constant after the initial transients in the solution process damp out. Figure 5.18 gives an example of the average density residual for fully turbulent flow over the NASA-PW airfoil at the low incidence angle condition. The average density residual signifies the amount by which the solution is changing with each time step. For example, an average density residual of 7 indicates that the change in

the solution over the whole flow domain is by an average amount equal to 10^{-7} . The steady, non-oscillating C_L , and the absolute value of the average density residual greater than 8.5 indicate the solution has converged. The solution convergence history for the 363 x 201 grid is similar to the 193 x 101 grid results displayed in Figures 5.17 and 5.18.

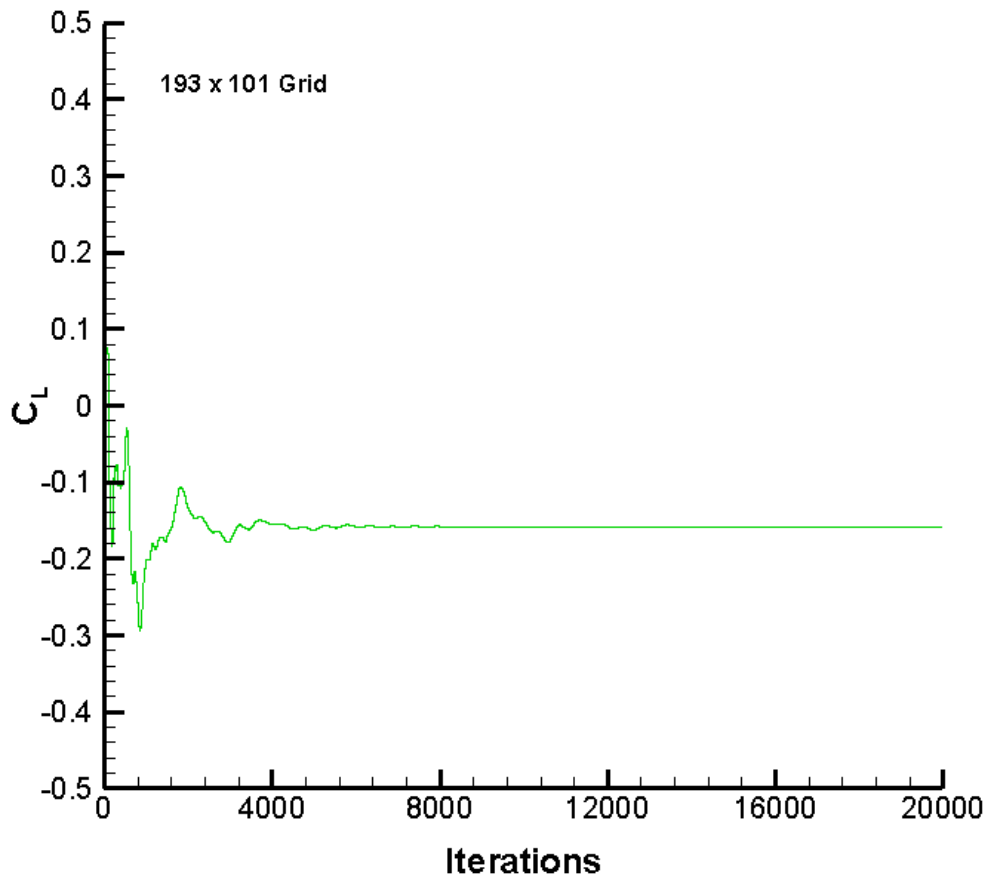


Figure 5.17: Example of NASA-PW airfoil lift coefficient convergence history at the low incidence angle condition for fully turbulent flow

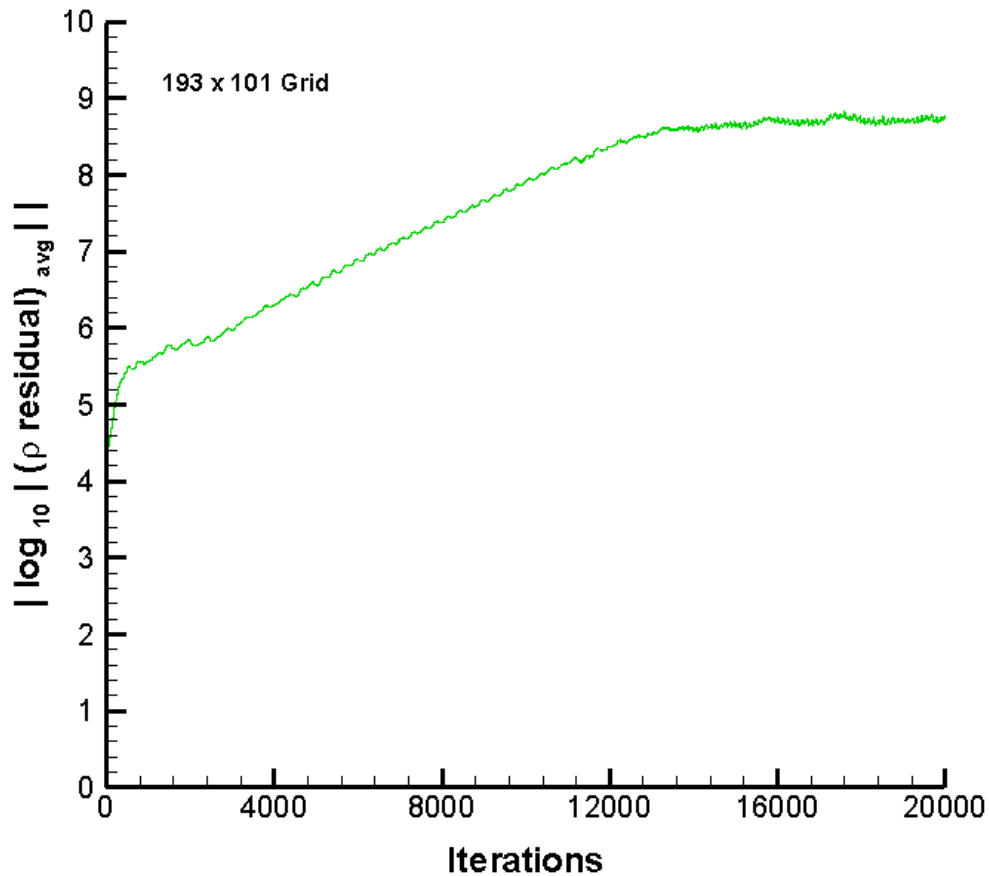


Figure 5.18: Example of the absolute value of the average density residual convergence history for the NASA-PW airfoil at the low incidence angle condition for fully turbulent flow

The chordwise distribution of the surface pressure coefficient are presented below in Figures 5.19 and 5.20 for fully turbulent flow on both grids. Overall, the solutions indicate a good correlation between the fully turbulent computations and the experimental data. The solutions obtained from both the coarse and dense grids are very close to each other over the whole of the airfoil surface except for a small region just downstream of the suction peak. The most important feature of interest here is the surface pressure distribution near the leading edge of the airfoil's suction surface where a small separation

bubble exists. For these fully turbulent calculations, the inlet turbulent viscosity was fixed at 0.009, vorticity based production formulation was used in the SA model, and streamline curvature correction was not used.

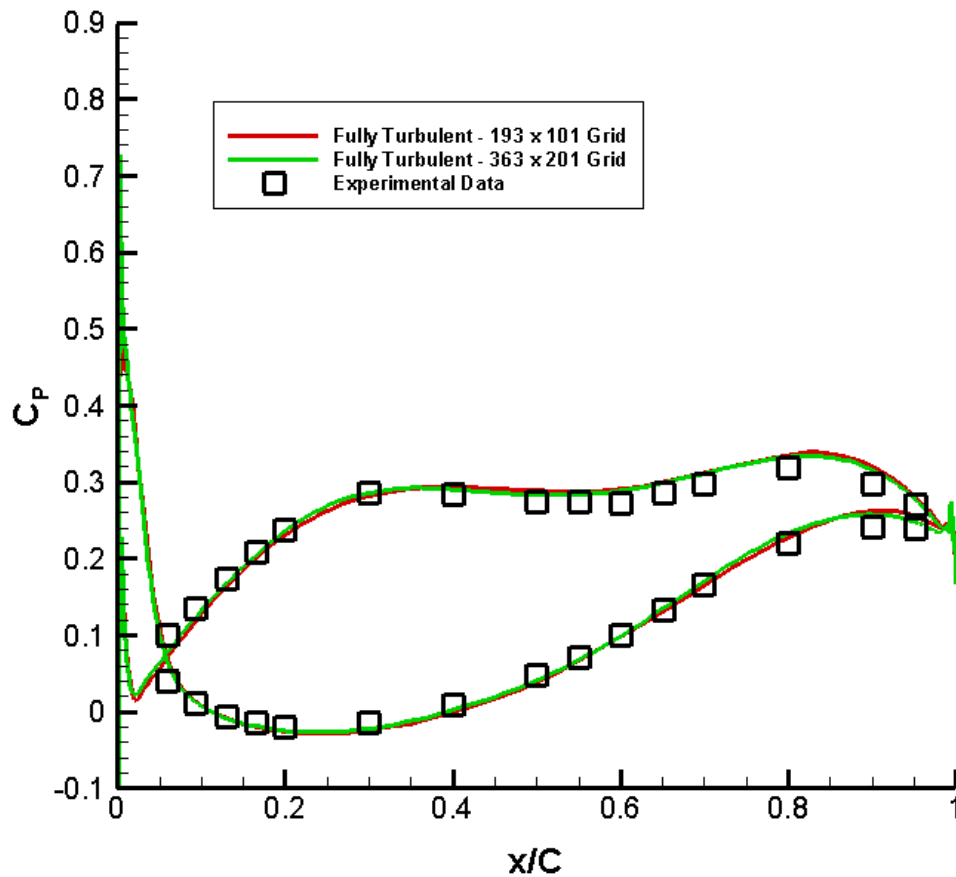


Figure 5.19: Surface pressure coefficient distribution for the NASA-PW airfoil at the low incidence angle condition for fully turbulent flow

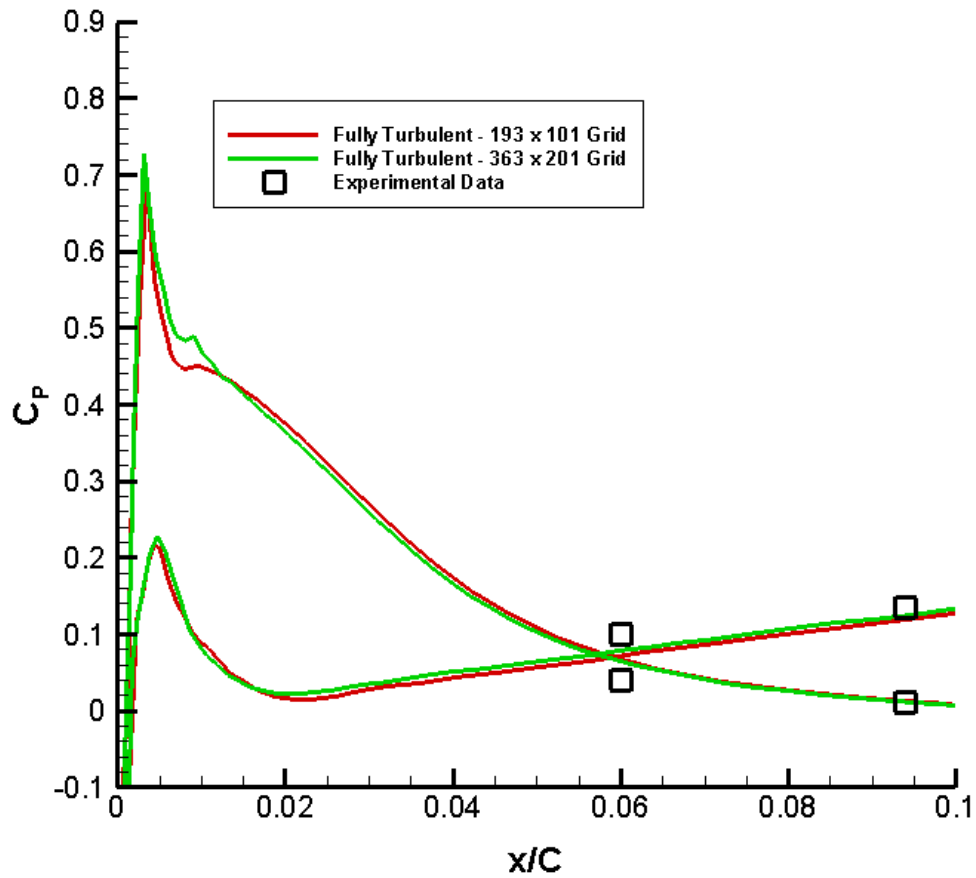


Figure 5.20: Leading edge surface pressure coefficient distribution for the NASA-PW airfoil at the low incidence angle condition for fully turbulent flow

Baldwin-Lomax and Spalart-Allmaras Model

The ability of the code to convert the eddy viscosity, ν_t , into the transported variable $\tilde{\nu}$ of SA model is used to speed up the convergence of the solution. Figure 5.21 shows the lift coefficient convergence history for the SA model restarted from the BL model using the coarse grid. It can be observed that when better initial conditions were provided to the SA model by starting the solution process using the BL model, convergence occurred in a smaller number of iterations for SA model as compared to

when SA model alone was used. Moreover, the lift coefficients obtained using the two methodologies were the same, as expected. Figures 5.22 and 5.23 present the comparison of steady surface pressure coefficient distribution over the airfoil surface obtained using the traditional methodology (SA model alone), which is adopted throughout this research, and the option of using both BL and SA models in conjunction to expedite the computations. Both the methodologies gave the exact same results. Moreover, the solution for leading edge pressure distribution being the same using the new approach and the traditional approach is very encouraging in terms of computation time since the leading edge pressure distribution for the suction surface is crucial due to the presence of a small separation bubble. For the computations shown, the inlet turbulent viscosity was fixed at 0.009, vorticity based production formulation was used in the SA model, and streamline curvature correction was not used.

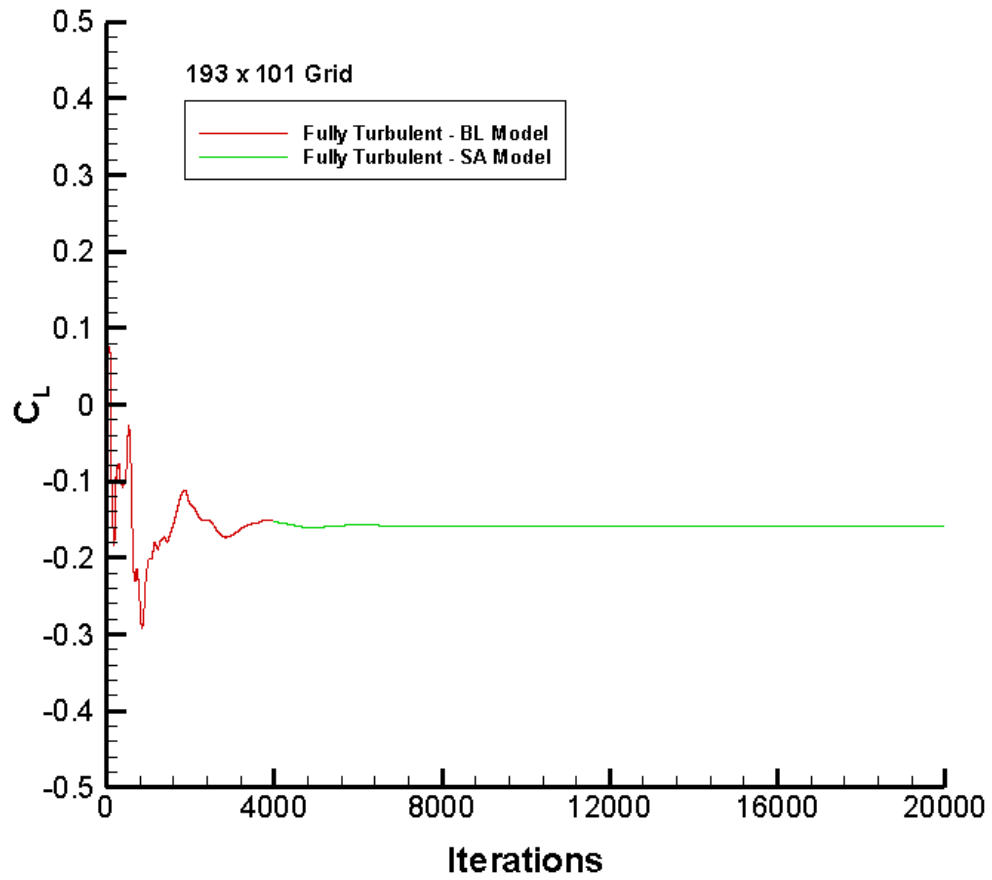


Figure 5.21: NASA-PW airfoil lift coefficient convergence history at the low incidence angle condition for fully turbulent flow with the BL model providing the initial conditions for the SA model

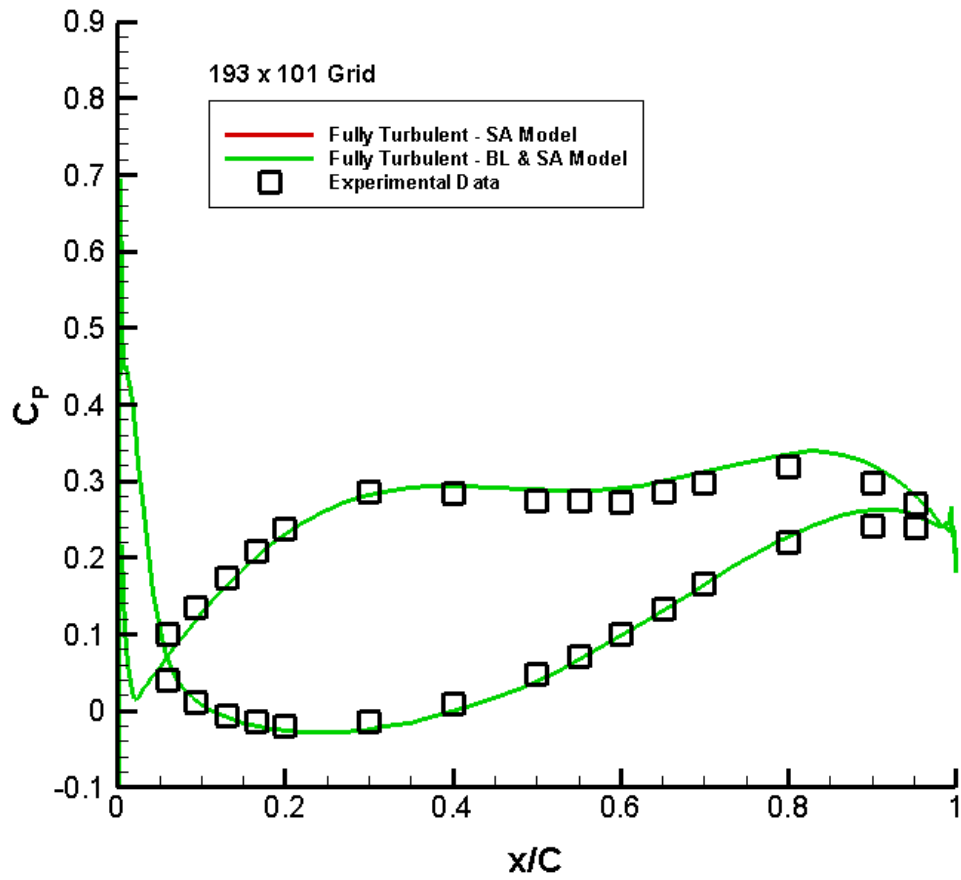


Figure 5.22: Surface pressure coefficient distribution for the NASA-PW airfoil at the low incidence angle condition for fully turbulent flow with the BL model providing the initial conditions for the SA model

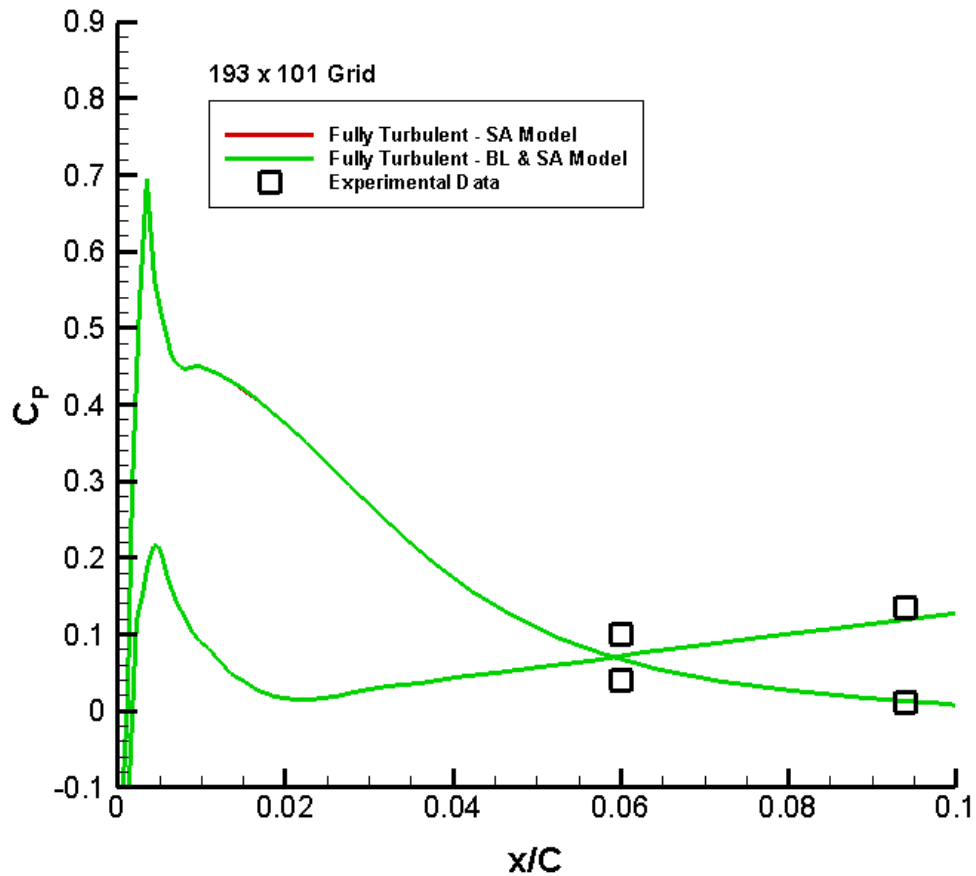


Figure 5.23: Leading edge surface pressure coefficient distribution for the NASA-PW airfoil at the low incidence angle condition for fully turbulent flow with the BL model providing the initial conditions for the SA model

Inlet Turbulent Viscosity Study

The steady surface pressure coefficient distribution for fully turbulent flow is presented below in Figure 5.24 with different inlet turbulent viscosities. The coarse grid of size 193 x 101 was used for the study. The computations were carried out using the vorticity based production formulation in the SA model, and streamline curvature correction was not used. The predicted pressure distribution is the same for both the values of inlet turbulent viscosities considered, and have a good correlation with the

experimental data points except in the leading edge region. The leading edge surface pressure distribution can be seen in Figure 5.25. The pressure surface showed a minor change in the solution for the leading edge region. A major change is seen in the pressure distribution for the suction surface leading edge region with a sizeable increase in the value of suction peak as the inlet turbulent viscosity was increased to a value of 10.0. This is attributed to the presence of a small separation bubble near the leading edge region of the suction surface. Since there is no experimental data available for the leading edge portion of the airfoil, it cannot be clearly stated as to which value of inlet turbulent viscosity gives a better solution. Nevertheless, it should be noted that changing the inlet turbulent viscosity changes the solution in the leading edge region where the separation bubble exists.

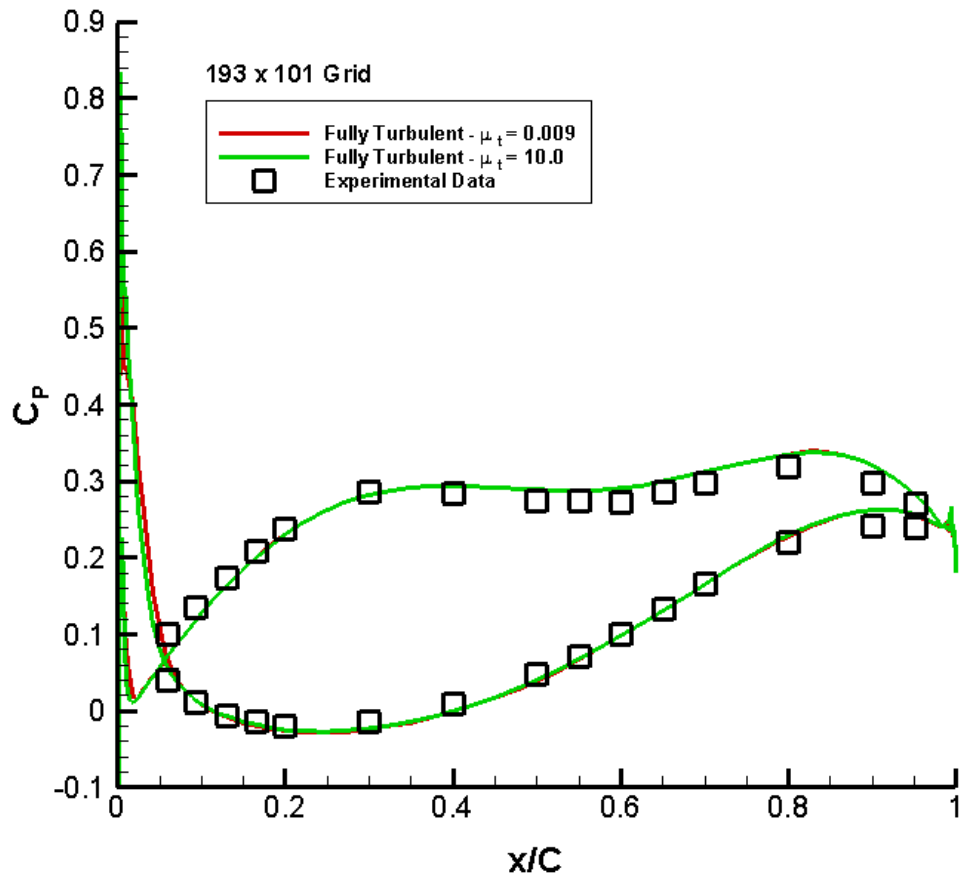


Figure 5.24: Surface pressure coefficient distribution for the NASA-PW airfoil at the low incidence angle condition for fully turbulent flow with different inlet turbulent viscosity values

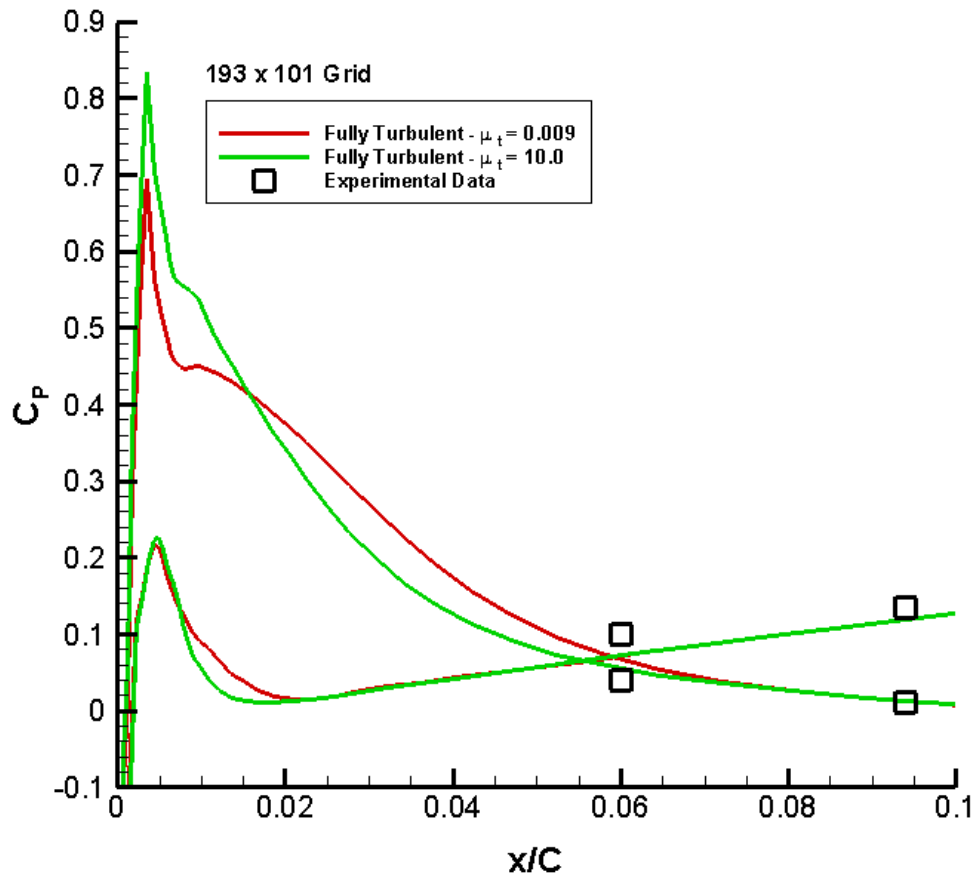


Figure 5.25: Leading edge surface pressure coefficient distribution for the NASA-PW airfoil at the low incidence angle condition for fully turbulent flow with different inlet turbulent viscosity values

Streamline Curvature Correction Study

Streamline curvature correction was used in the fully turbulent calculation for the low incidence angle case on the coarse grid to investigate the effect of streamline curvature on the steady surface pressure distribution. Overall, the pressure distribution over the surface of the airfoil was the same when compared to the solution where streamline curvature correction was not used as illustrated in Figure 5.26 except in the leading edge region. In the leading edge region the pressure distribution changed and the

pressure coefficient value for the suction surface decreased with a corresponding decrease in pressure coefficient for the suction peak as seen in Figure 5.27. This change is attributed to the circular leading edge and to the presence of a small separation bubble over the suction surface near the leading edge. No change was observed for the pressure surface pressure distribution. For these computations, the inlet turbulent viscosity was fixed at 0.009, and vorticity based production formulation was used in the SA model.

Figure 5.28 shows the streamlines in the leading edge region for fully turbulent flow with and without streamline curvature correction. It is observed that flow recirculation occurs inside the separation bubble on the suction surface. The streamlines for the pressure surface indicate that the flow is attached. Only subtle changes in the ρu contours can be seen when streamline curvature effect is included in the calculation. Moreover, it can be noticed that the recirculating flow region gets extended slightly when streamline curvature correction is included in the calculation.

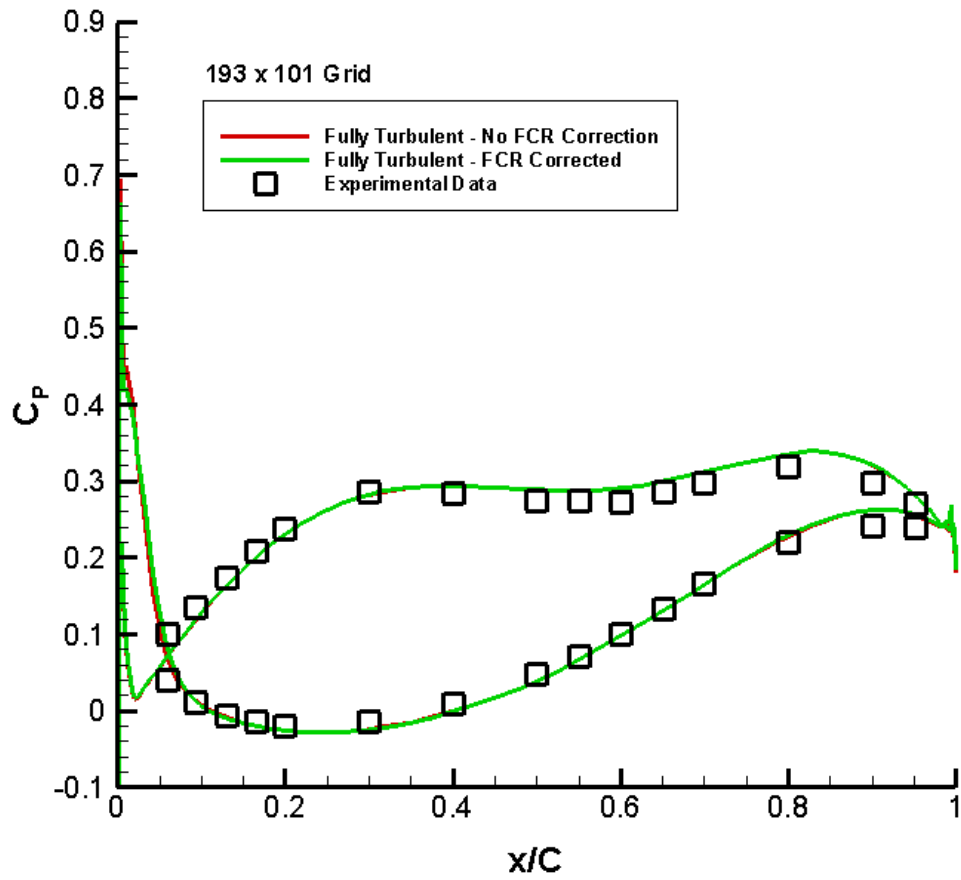


Figure 5.26: Surface pressure coefficient distribution for the NASA-PW airfoil at the low incidence angle condition for fully turbulent flow with and without the streamline curvature correction

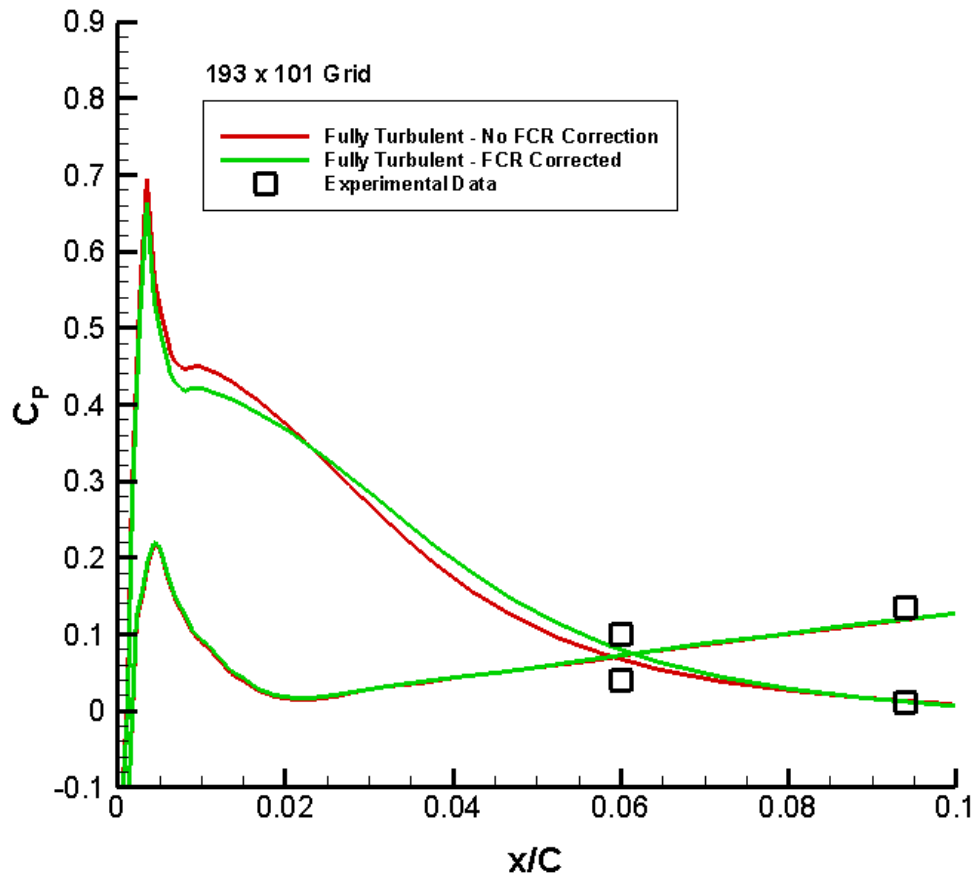
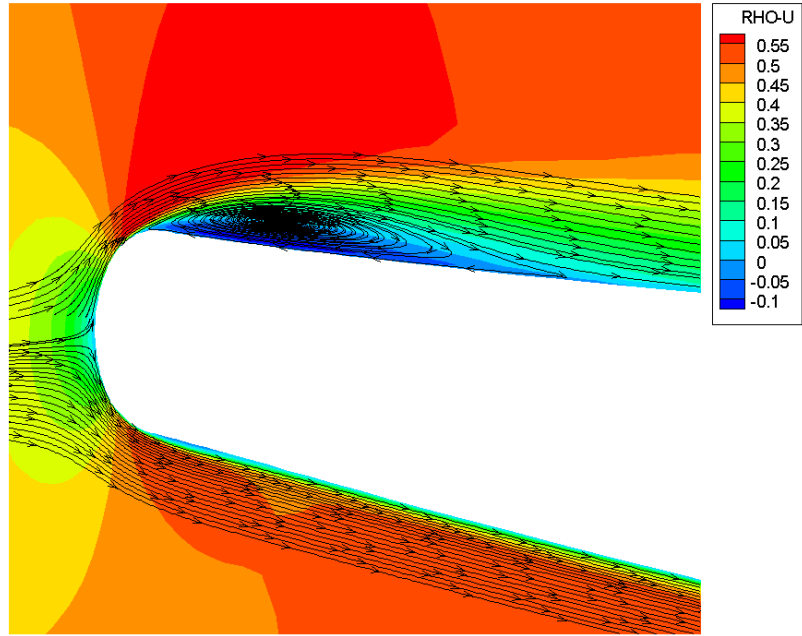
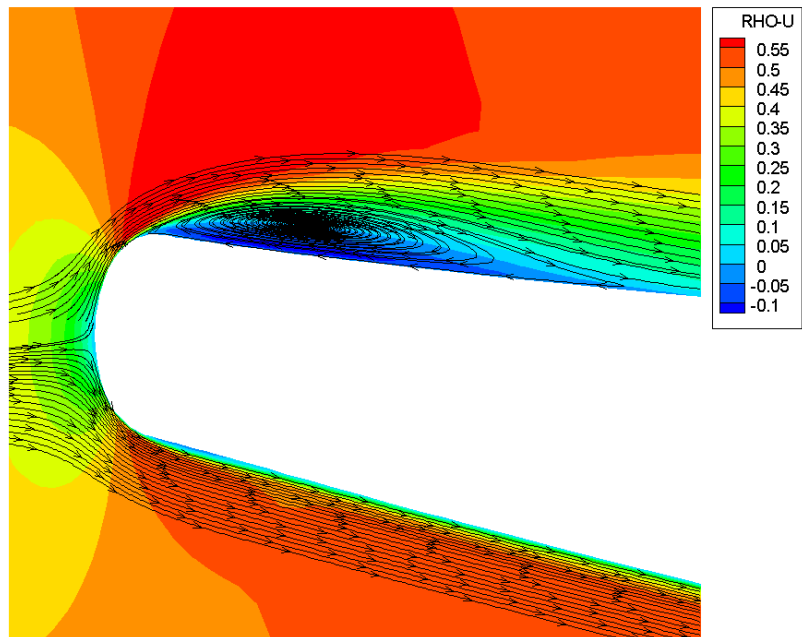


Figure 5.27: Leading edge surface pressure coefficient distribution for the NASA-PW airfoil at the low incidence angle condition for fully turbulent flow with and without the streamline curvature correction



(a)



(b)

Figure 5.28: Streamlines in the leading edge region of the NASA-PW airfoil (193 x 101 Grid) at the low incidence angle condition for fully turbulent flow (a) without streamline curvature correction, and (b) with streamline curvature correction

Transition

Transition calculations were done using the coarse grid of size 193 x 101 and the dense grid of size 363 x 201. For calculating transition, solutions were first generated for fully turbulent flow using the SA model. The converged fully turbulent solutions were then restarted with the DN transition model activated. The lift coefficient convergence history for the fully turbulent and transition calculations for the low incidence angle condition are displayed in Figure 5.29. This is followed by the average density residual convergence history for fully turbulent and transition simulations, which are shown in Figure 5.30. As with the fully turbulent calculations, the transition calculations converged since C_L is steady, non-oscillating, and the absolute value of the average density residual is greater than 8.5.

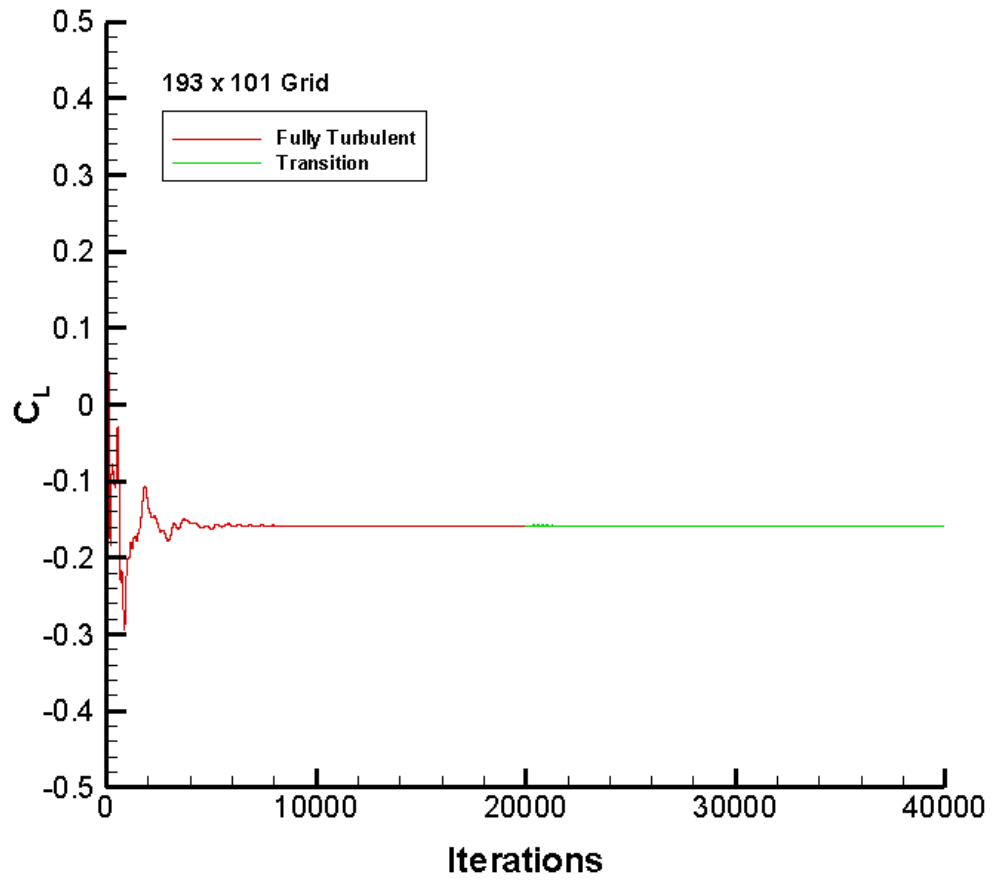


Figure 5.29: Example of NASA-PW airfoil lift coefficient convergence history at the low incidence angle condition for turbulent and transitional flow

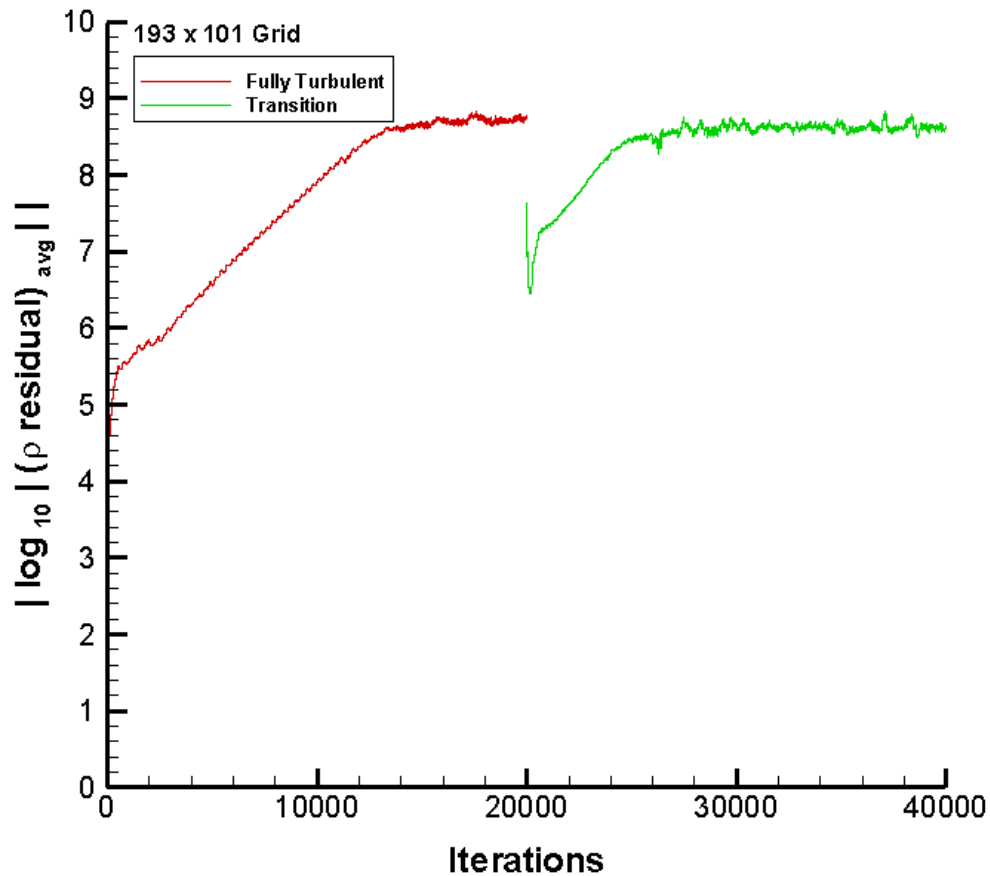


Figure 5.30: Example of the absolute value of the average density residual convergence history for the NASA-PW airfoil at the low incidence angle condition for turbulent and transitional flow

The NASA-PW airfoil at the low incidence angle condition had a small separation bubble in the leading edge region of the suction surface. To illustrate the flow separation and flow recirculation, ρu contours and velocity vectors are presented below. Figure 5.31 shows the ρu contours of the flow around the airfoil. The ρu contours represent the momentum transfer in the streamwise direction. It can be seen that the contour levels vary as the flow passes through the mid-channel region. In particular, the flow phenomenon that is of interest in this investigation occurs near the leading edge. The leading edge ρu

contours is shown in Figure 5.32. The flow undergoes a huge change in the streamwise momentum as it hits the tip of the leading edge. The pressure surface does not have any interesting flow features. Flow separation occurs in the leading edge region of the suction surface forming a small separation bubble due to large flow gradients in that region and also due to the leading edge geometry of the blade profile. The separation bubble is seen as the blue region where the ρu contours have negative values. It is over this separation bubble that the flow undergoes transition from laminar to turbulent flow. The flow then reattaches as turbulent behind the separation bubble and remains attached up to the trailing edge of the airfoil. Several contour levels are seen in the suction surface leading edge region indicating the complicated physics in that region. Figure 5.33 presents an example of velocity vectors with ρu contours in the leading edge region of the NASA-PW airfoil at low incidence angle condition for fully turbulent flow and transitional flow. It can be seen that in the regions where flow separation has occurred, flow recirculation is taking place. The velocity vectors clearly indicate a strong recirculating flow inside the separation bubble near the leading edge of the airfoil. Moreover, including transition in the computations shows that the thickness of the separation bubble increases compared to that of the fully turbulent computations.

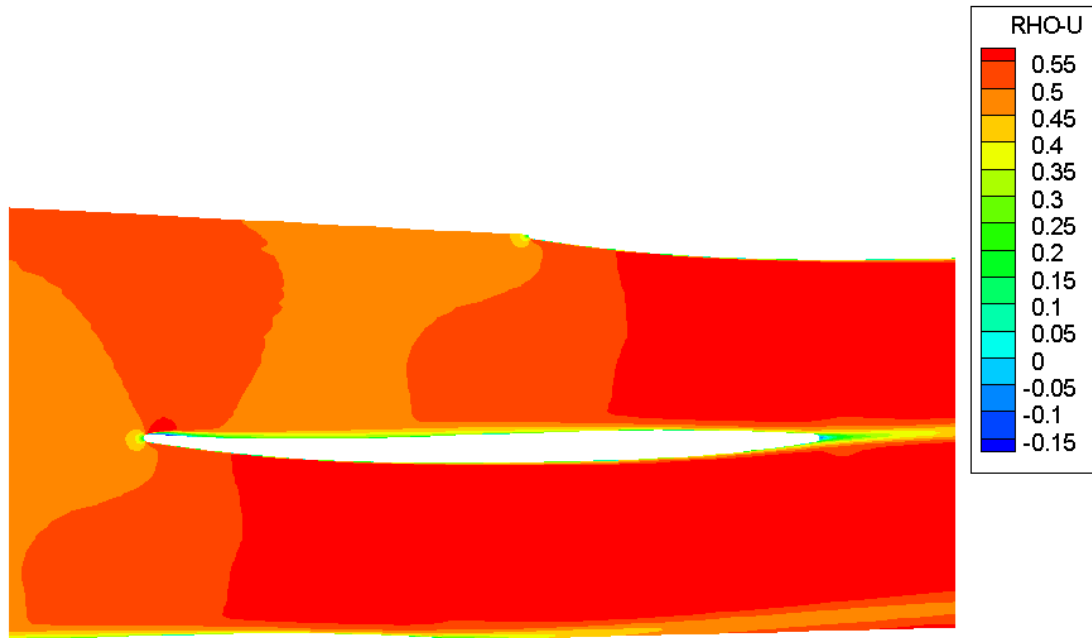


Figure 5.31: Contours of ρu for the NASA-PW airfoil (193 x 101 Grid) at the low incidence angle condition for transitional flow using fixed transition onset with $x_{LT} = 0.03$

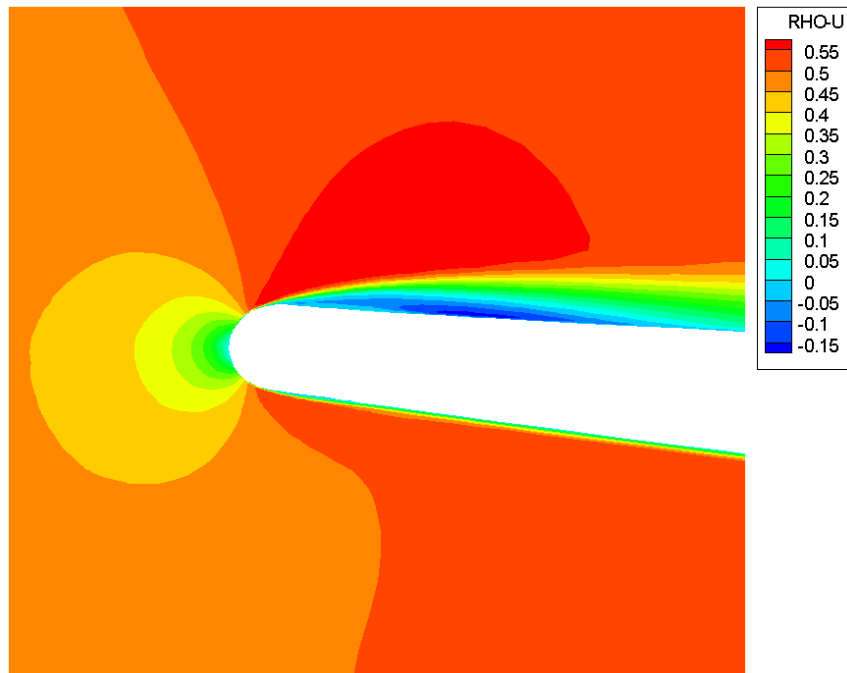
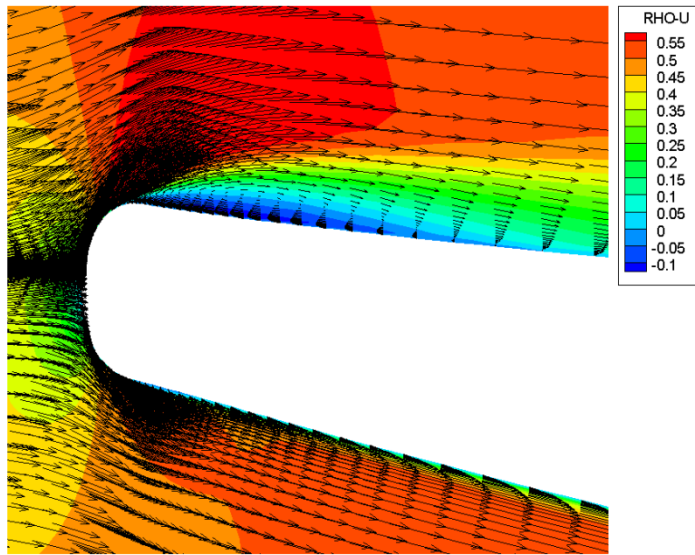
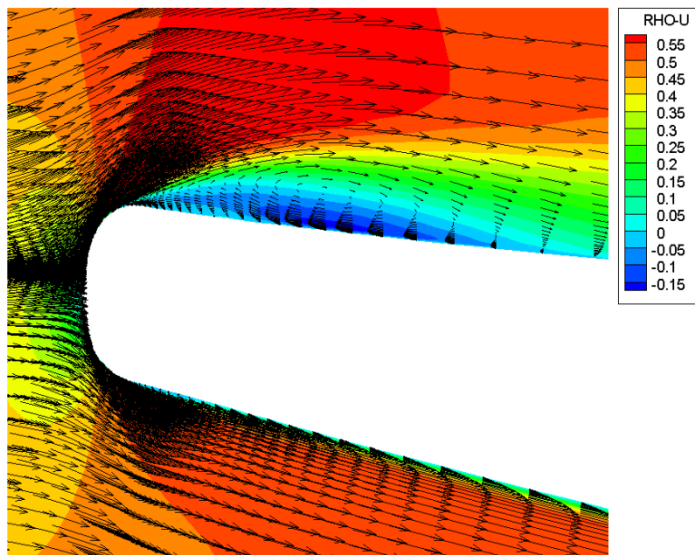


Figure 5.32: Contours of ρu in the leading edge region of the NASA-PW airfoil (193 x 101 Grid) at the low incidence angle condition for transitional flow using fixed transition onset with $x_{LT} = 0.03$



(a)



(b)

Figure 5.33: Velocity vectors with ρu contours in the leading edge region of the NASA-PW airfoil (193 x 101 Grid) at the low incidence angle condition for (a) fully turbulent flow, and (b) transitional flow using fixed transition onset with $x_{LT} = 0.03$

The steady surface pressure coefficient distribution for the transition calculations at the low incidence angle condition will now be presented. Transition calculations were performed using the intermittency correlation of DN model on the suction surface. For the pressure surface, transition was computed using the transition model of Solomon et al. (1996). For this part of the investigation, the transition calculations were performed by fixing the inlet turbulent viscosity at 0.009, vorticity based production formulation was used in the SA model, and streamline curvature correction was not used. Figures 5.34 through 5.39 present the computed chordwise surface pressure distribution with the experimental data for fixed lengths of transition. Figures 5.40 and 5.41 present the computed chordwise surface pressure distribution with the experimental data for transition computed using Mayle's transition length model. Grid convergence of the transition calculations is demonstrated by computing on the coarse and dense grids. The fully turbulent and transitional flow calculations predicted that a small separation bubble exists immediately downstream of the airfoil leading edge circle on the suction surface. The separation bubble is a consequence of the approximately 7° of true incidence on the airfoil. Overall, the predicted pressure distribution has good correlation between the turbulent and transitional flow solutions and the experimental data except near the leading edge region. For the fixed transition length cases on the suction surface, the transition onset point was selected and kept fixed within the separation bubble and immediately downstream of the point of separation. The fixed transition termination point was also selected within the separation bubble and was varied to investigate the influence of transition length on the steady pressure distribution. Mayle's transition length model also predicted the transition onset and the transition termination point locations within the

separation bubble. For the fixed transition point investigation and Mayle's transition prediction model the pressure surface transition onset point was set to $0.1711C$ for use with the transition model of Solomon et al. (1996). The influence of transition on the suction surface is largest upstream of $0.1C$ where the separation bubble is located, which is more clearly illustrated in Figures 5.35, 5.37, and 5.39 for the fixed transition length cases, and Figure 5.41 for Mayle's model. Transition calculations showed that a pressure plateau exists within the separation bubble that is not evident in the fully turbulent calculations. For a fixed transition onset point, the pressure plateau became larger as the transition length increased. At the same time with the increase in the transition length, the pressure coefficient value decreased. Mayle's transition length model predicted the transition onset location farther inside the separation bubble with a very short transition length. This showed that as the suction surface transition onset point moved downstream, the pressure plateau again became larger and decreased in magnitude. The peak pressure on the suction surface also reduced as the transition length increased, or as the transition onset point moved farther downstream.

The variation of the reattachment location with streamwise transition length is presented in Table 5.1 along with the separation point, and the streamwise transition onset and transition termination locations for both grids. The size of the separation bubble did not change for the different transition calculations computed using the coarse grid; the predicted separation bubble size in streamwise coordinates was 0.067 , and the corresponding size in Cartesian coordinates was $0.0596C$. The fully turbulent calculation on the coarse grid predicted a slightly smaller size for the separation bubble. Computations using the dense grid showed variations in the size of the separation bubble,

due to the higher streamwise grid resolution. Again, the fully turbulent calculation on the dense grid predicted a slightly smaller separation bubble size compared to the transition calculations. The separation bubble size increased with increase in the transition length. For the smallest fixed transition length case, the size of the separation bubble was predicted to be 0.06 in the streamwise coordinates, and 0.056C in the Cartesian coordinates. The largest fixed transition length case predicted the separation bubble size as 0.067 in the streamwise coordinates, and 0.063C in the Cartesian coordinates. Mayle's model on the dense grid predicted the size of the separation bubble as 0.063 in the streamwise coordinates, and 0.06C in the Cartesian coordinates. The differences seen in the predicted reattachment points for different transition lengths/onset points on the dense grid are less than 0.4% chord between the two grids. Moreover, no grid studies were done to resolve the reattachment point accurately. All the transition calculations blend back into the fully turbulent calculation around the first experimental data point on the suction surface.

No significant differences between the transition and turbulent calculations were found along the pressure surface for transition zone changes on the suction surface. Moreover, no major change in the pressure coefficient of the pressure surface was observed for the specified pressure surface transition onset location.

When the experiments were conducted, no flow visualization was done because the pressure distributions did not raise any suspicion of flow separation in the leading edge region. Furthermore, there is no experimental data available in the transition region for the low incidence angle condition, which would indicate whether the transition

solutions obtained are better than the fully turbulent solution, due to instrumentation limitations caused by the airfoil thickness in this area.

Table 5.1: Transitional flow parameters for the NASA-PW airfoil at the low incidence angle condition

Grid Size	Transition Model	x_s	x_r	S_s	S_r	x_t	x_T	x_{LT}
193 x 101	None, Fully Turbulent	0.0058	0.0582	0.0098	0.0688	NA	NA	NA
	Fixed	0.0051	0.0647	0.0090	0.0760	0.0200	0.0300	0.0100
	Fixed	0.0051	0.0647	0.0090	0.0760	0.0200	0.0400	0.0200
	Fixed	0.0051	0.0647	0.0090	0.0759	0.0200	0.0500	0.0300
	Mayle	0.0051	0.0647	0.0090	0.0760	0.0275	0.0349	0.0074
363 x 201	None, Fully Turbulent	0.0054	0.0586	0.0093	0.0659	NA	NA	NA
	Fixed	0.0054	0.0618	0.0093	0.0691	0.0200	0.0300	0.0100
	Fixed	0.0054	0.0651	0.0092	0.0726	0.0200	0.0400	0.0200
	Fixed	0.0054	0.0686	0.0092	0.0762	0.0200	0.0500	0.0300
	Mayle	0.0054	0.0651	0.0092	0.0726	0.0285	0.0362	0.0077

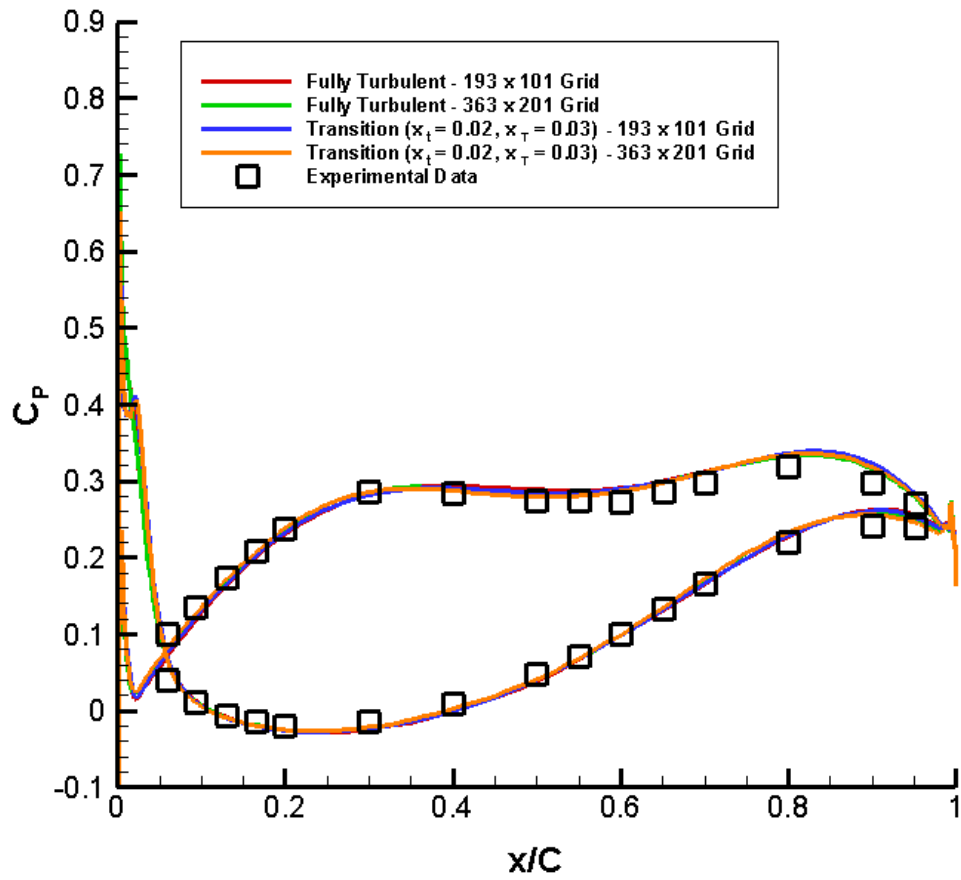


Figure 5.34: Surface pressure coefficient distribution for the NASA-PW airfoil at the low incidence angle condition for transitional flow using fixed transition onset with $x_{LT} = 0.01$

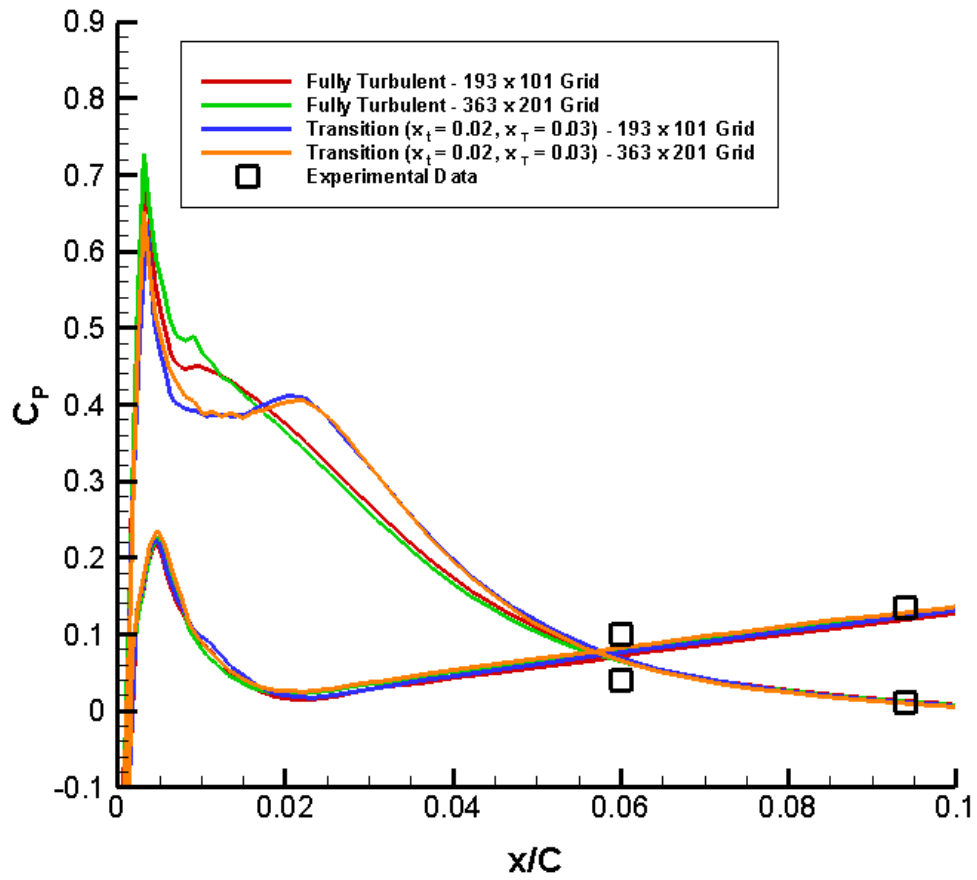


Figure 5.35: Leading edge surface pressure coefficient distribution for the NASA-PW airfoil at the low incidence angle condition for transitional flow using fixed transition onset with $x_{LT} = 0.01$

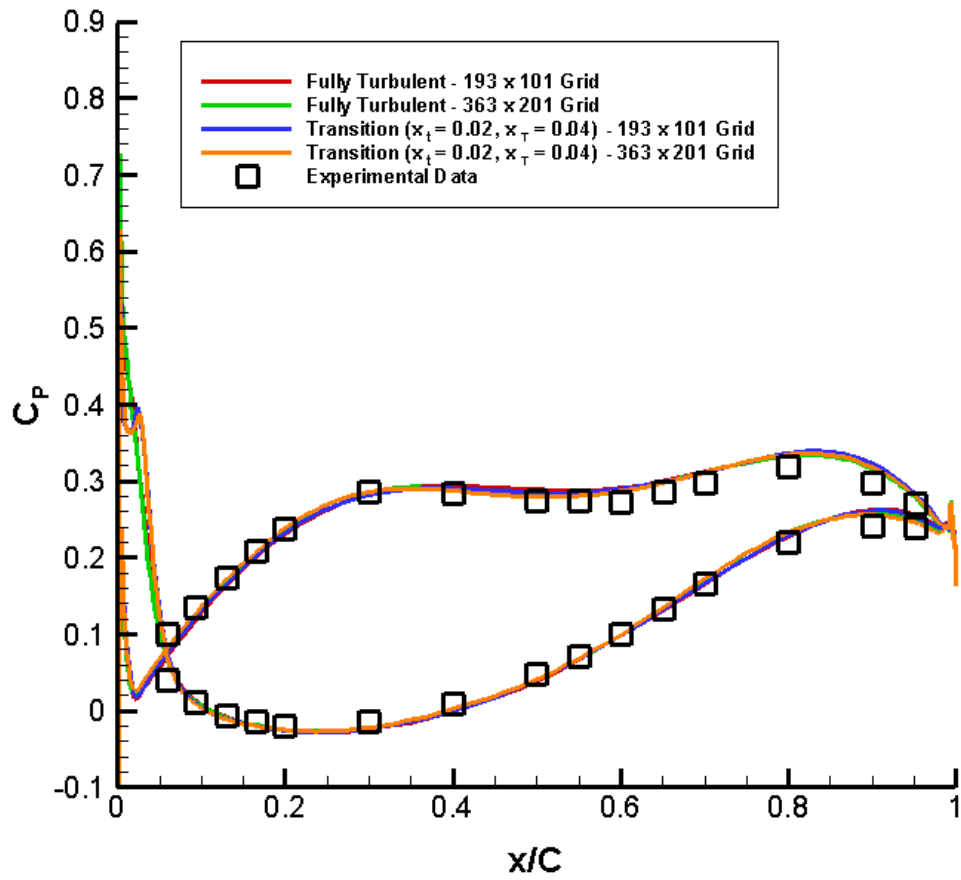


Figure 5.36: Surface pressure coefficient distribution for the NASA-PW airfoil at the low incidence angle condition for transitional flow using fixed transition onset with $x_{LT} = 0.02$

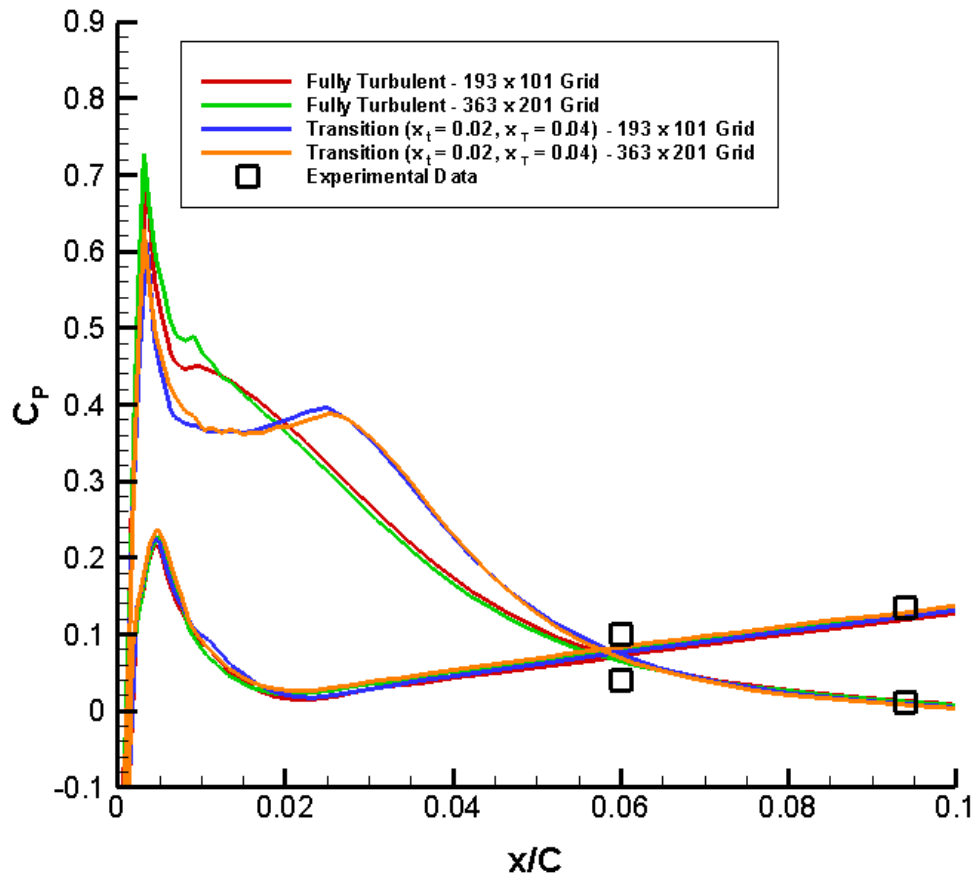


Figure 5.37: Leading edge surface pressure coefficient distribution for the NASA-PW airfoil at the low incidence angle condition for transitional flow using fixed transition onset with $x_{LT} = 0.02$

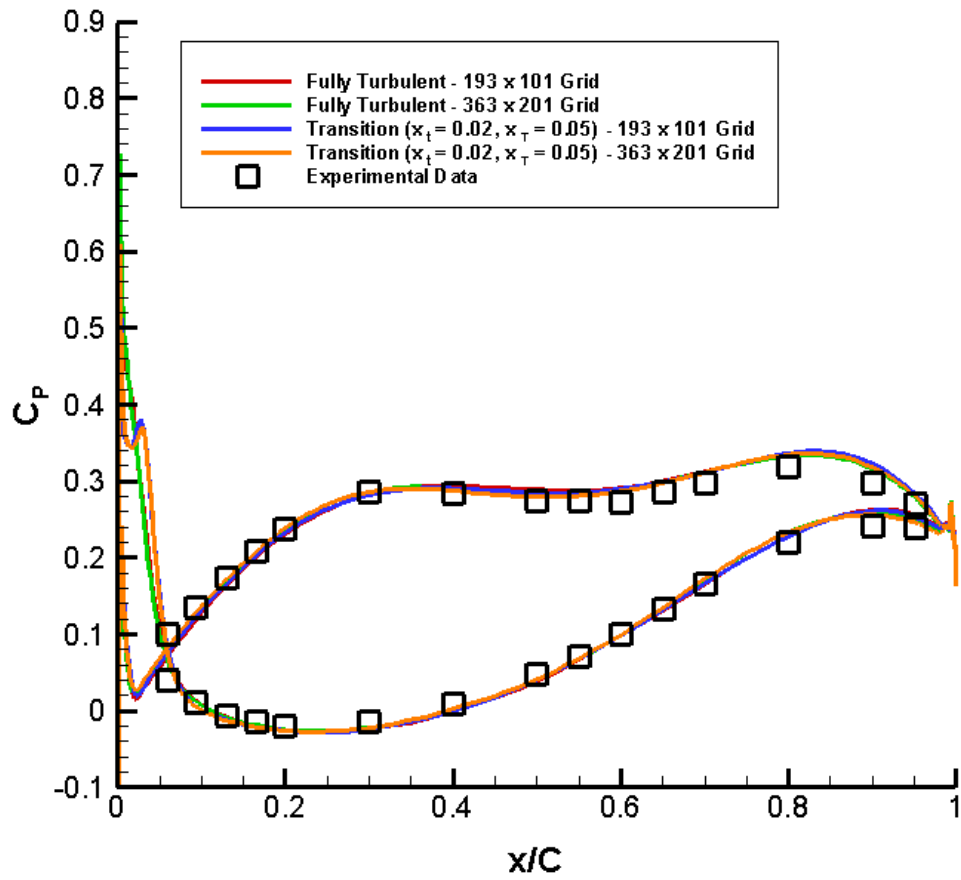


Figure 5.38: Surface pressure coefficient distribution for the NASA-PW airfoil at the low incidence angle condition for transitional flow using fixed transition onset with $x_{LT} = 0.03$

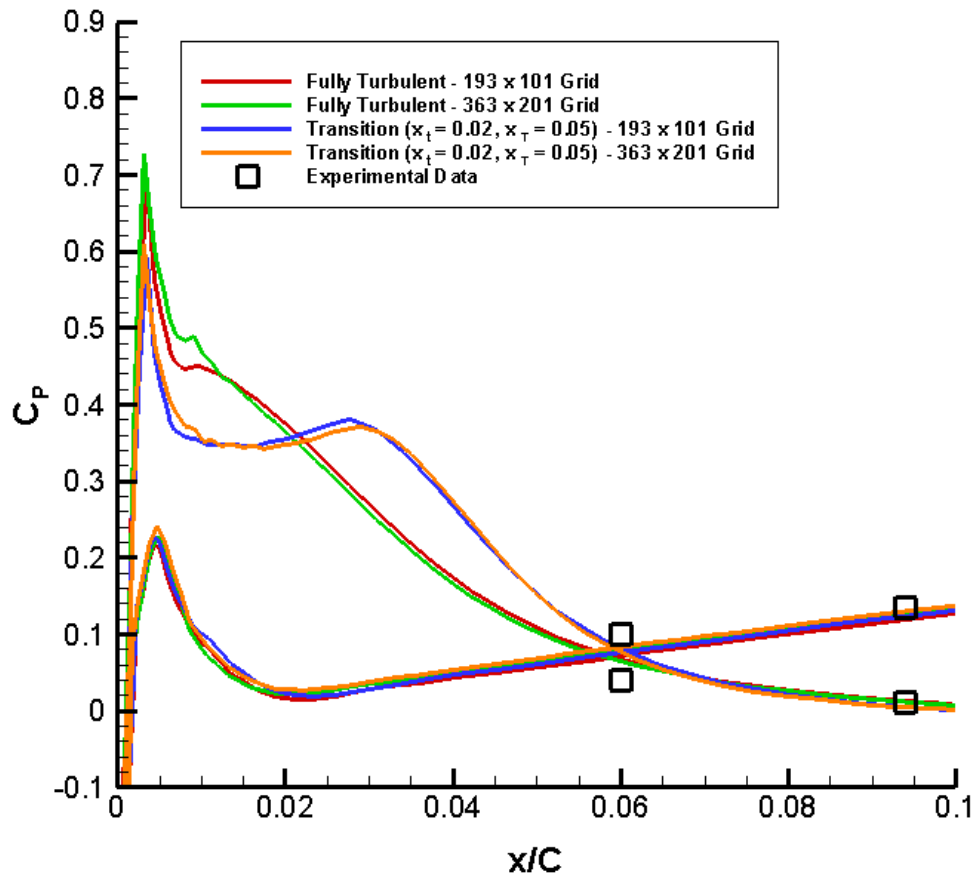


Figure 5.39: Leading edge surface pressure coefficient distribution for the NASA-PW airfoil at the low incidence angle condition for transitional flow using fixed transition onset with $x_{LT} = 0.03$

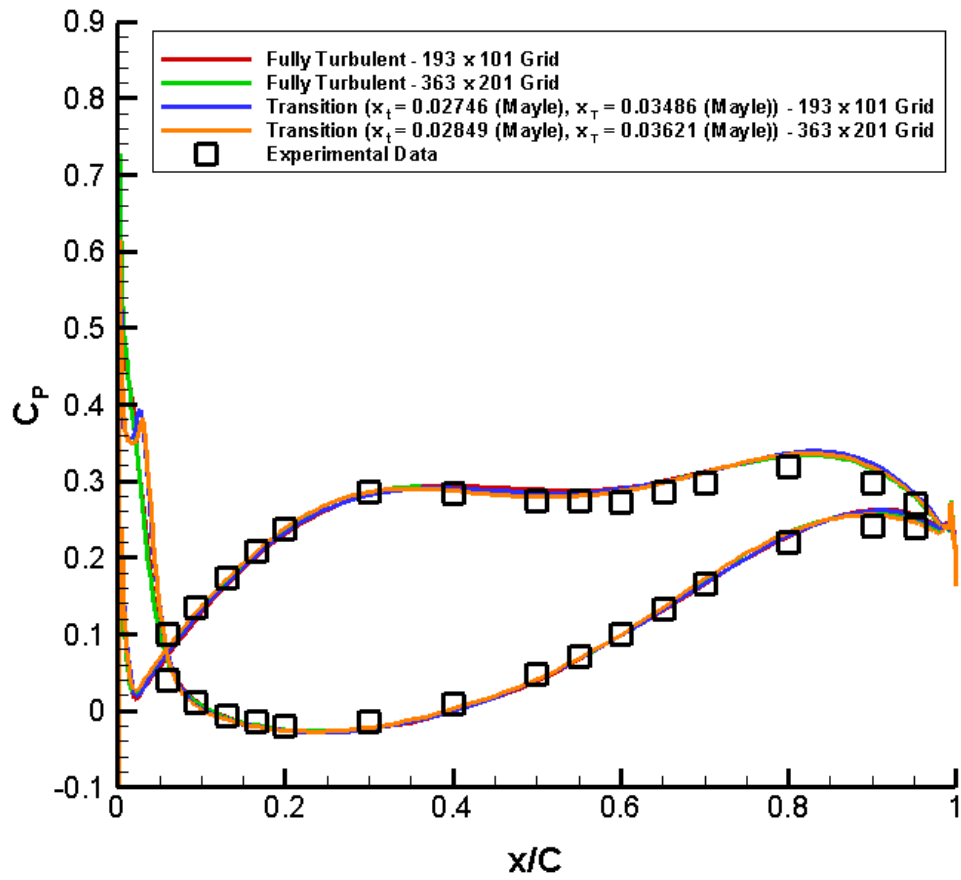


Figure 5.40: Surface pressure coefficient distribution for the NASA-PW airfoil at the low incidence angle condition for transitional flow using Mayle's transition length model

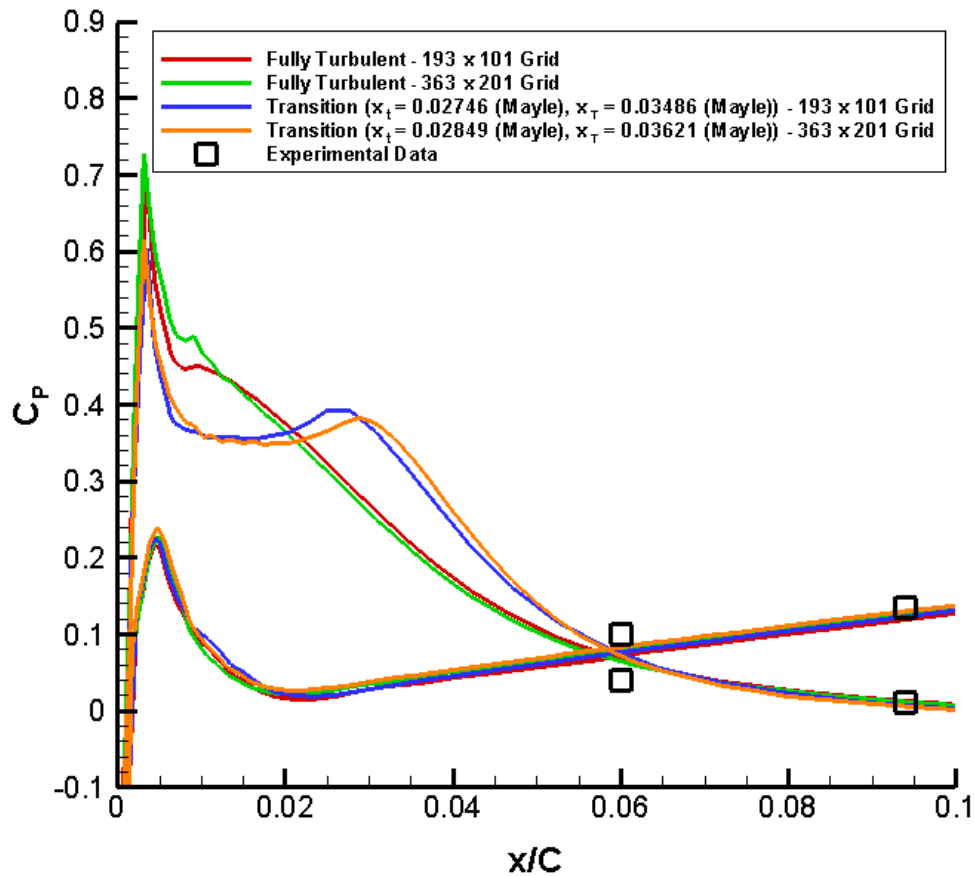


Figure 5.41: Leading edge surface pressure coefficient distribution for the NASA-PW airfoil at the low incidence angle condition for transitional flow using Mayle's transition length model

Inlet Turbulent Viscosity Study

Transitional flow calculations were performed using the NASA-PW airfoil coarse grid size of 193 x 101 for two values of inlet turbulent viscosity. The predicted chordwise steady surface pressure coefficient distribution with the experimental data for fixed transition length of $x_{LT} = 0.01$ is displayed in Figure 5.42. For these computations the vorticity based production formulation was used in the SA model, and the streamline curvature correction was not used. Both the values of inlet turbulent viscosity used in this

investigation produced a pressure plateau in the leading edge region of the suction surface where a small separation bubble is predicted. The leading edge surface pressure coefficient distribution is shown in Figure 5.43. The pressure surface transition onset point was set to $0.1711C$. Again, the influence of transition on suction surface is seen to be largest upstream of $0.1C$. The size of the pressure plateau within the separation bubble is nearly the same for the two values of inlet turbulent viscosity considered, which is expected since the transition onset and termination points is the same for the two transition cases. The higher value of inlet turbulent viscosity has a slightly higher pressure coefficient than that of the lower inlet turbulent viscosity value.

The variation of the reattachment point with inlet turbulent viscosity is presented in Table 5.2 along with the separation point, streamwise transition onset and transition termination points, and the streamwise transition length. The size of the separation bubble reduced when transition was computed for the higher value of inlet turbulent viscosity. The predicted separation bubble size in streamwise coordinates was 0.067 , and in Cartesian coordinates was $0.06C$ for the lower value of inlet turbulent viscosity, which was 0.009 . The higher value of inlet turbulent viscosity, which was 10.0 , predicted the size of the separation bubble as 0.06 in streamwise coordinates, and $0.053C$ in Cartesian coordinates. The flow separation near the leading edge on the suction surface occurred at the same location for both the values of inlet turbulent viscosity as predicted by the transition calculations, which is given in Table 5.2. The fully turbulent calculations also predicted the same separation point for the two inlet turbulent viscosity values. The fully turbulent calculations with the two inlet turbulent viscosities predicted a slightly

smaller size for the separation bubble as compared to their respective transition predictions.

The transition solutions for the pressure surface had no differences for the two inlet turbulent viscosity values. Moreover, no significant change occurred between the transition and fully turbulent calculations for the higher value of inlet turbulent viscosity.

Figure 5.44 shows the velocity vectors with ρu contours in the leading edge region for the inlet turbulent viscosity value of 0.009 for fully turbulent flow and transitional flow, and Figure 5.45 displays the same for the inlet turbulent viscosity value of 10.0. It can be seen that both the transition calculations using the two inlet turbulent viscosity values show an increase in the thickness of the separated flow region on the suction surface compared to the fully turbulent calculations. Fully turbulent calculation with the inlet turbulent viscosity value of 10.0 predicted the smallest and the thinnest separation bubble. The separation bubble thickness is nearly the same for the transition calculations using the inlet turbulent viscosity values of 0.009 and 10.0. The ρu contours and the velocity vectors near the pressure surface indicate that the flow remains attached for both the turbulent and transitional flow predictions using the two inlet turbulent viscosities.

Table 5.2: Transitional flow parameters for the NASA-PW airfoil at the low incidence angle condition for different values of inlet turbulent viscosity

μ_t	Transition Model	x_s	x_r	S_s	S_r	x_t	x_T	x_{LT}
0.009	None, Fully Turbulent	0.0058	0.0582	0.0098	0.0688	NA	NA	NA
	Fixed	0.0051	0.0647	0.0090	0.0760	0.02	0.03	0.01
10.0	None, Fully Turbulent	0.0058	0.0422	0.0098	0.0564	NA	NA	NA
	Fixed	0.0051	0.0582	0.0090	0.0687	0.02	0.03	0.01

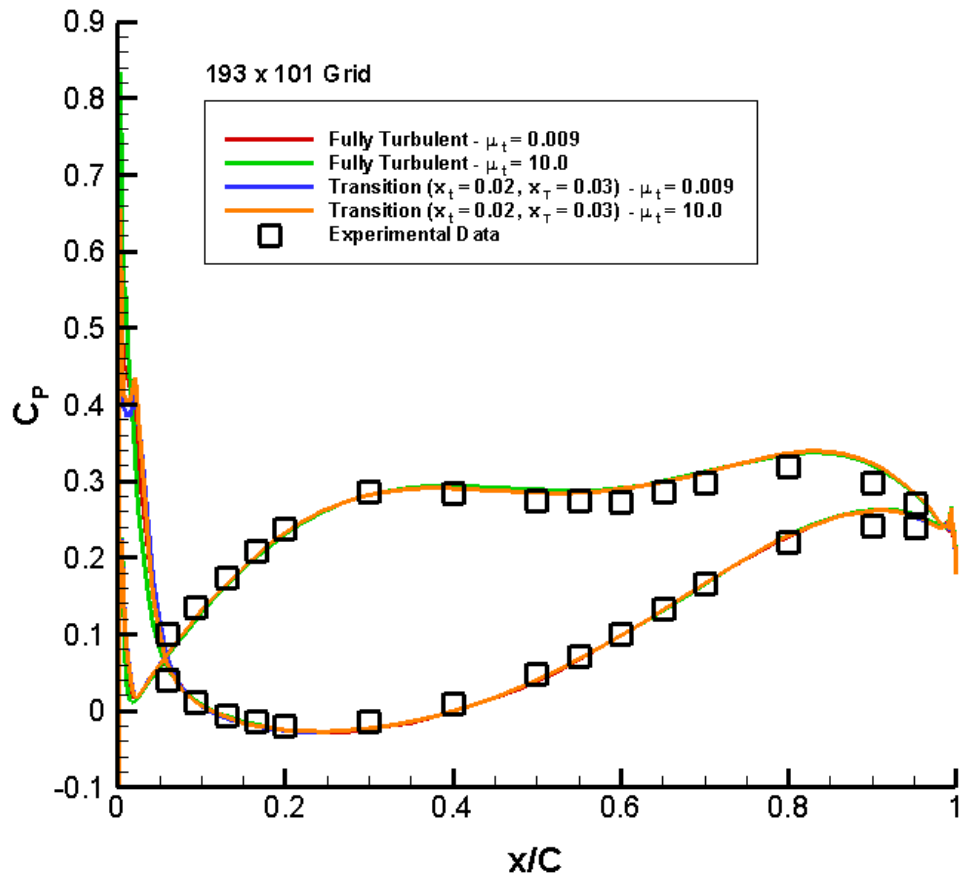


Figure 5.42: Surface pressure coefficient distribution for the NASA-PW airfoil at the low incidence angle condition for transitional flow using fixed transition onset with $x_{LT} = 0.01$ for different inlet turbulent viscosity values

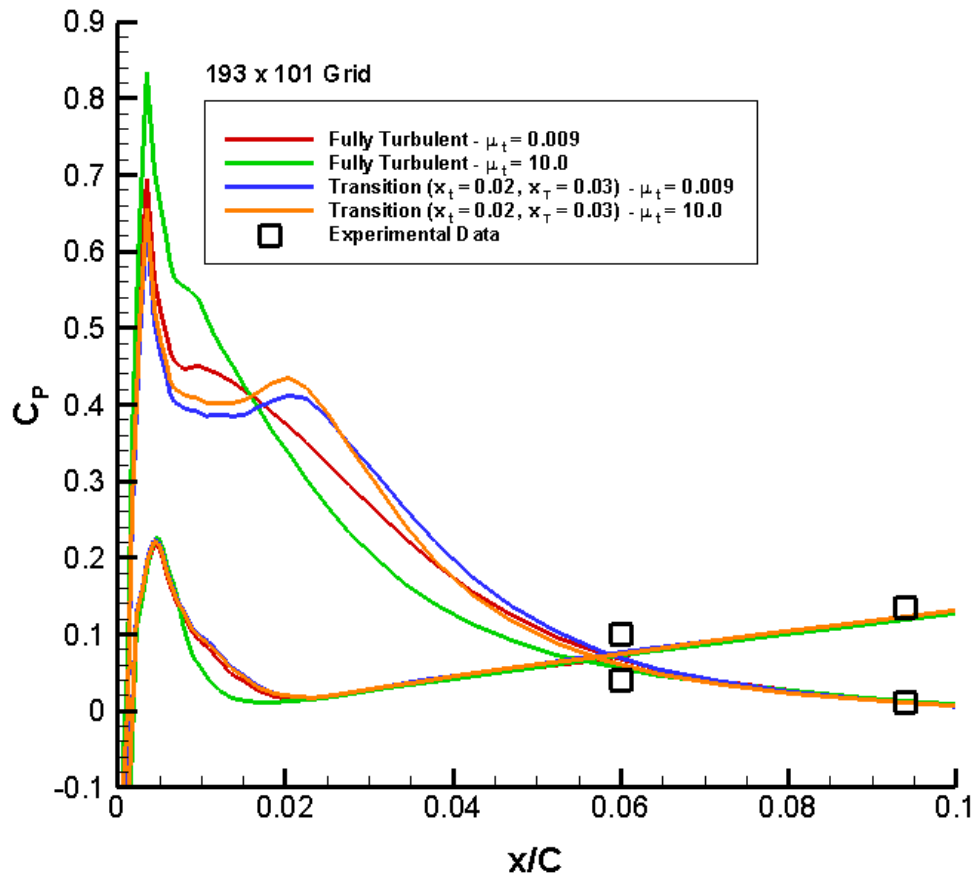
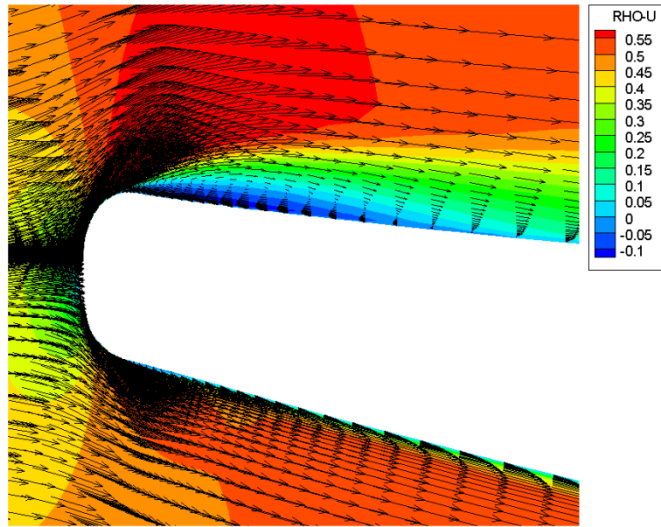
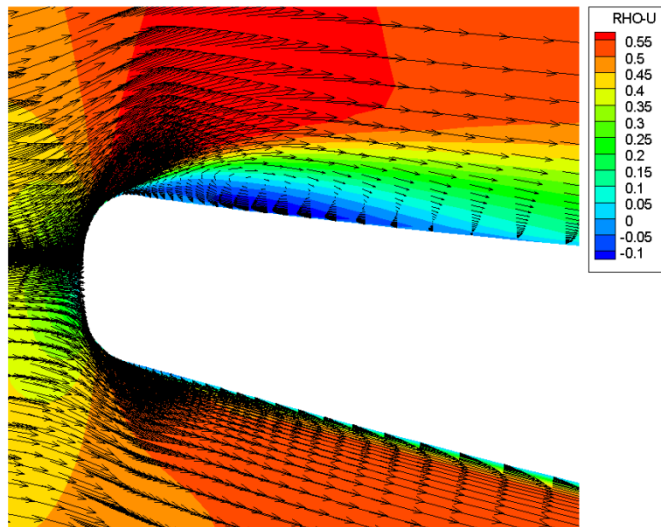


Figure 5.43: Leading edge surface pressure coefficient distribution for the NASA-PW airfoil at the low incidence angle condition for transitional flow using fixed transition onset with $x_{LT} = 0.01$ for different inlet turbulent viscosity values

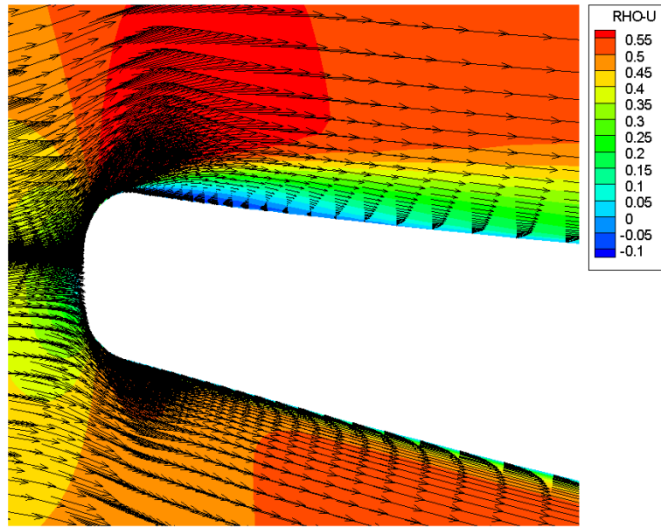


(a)

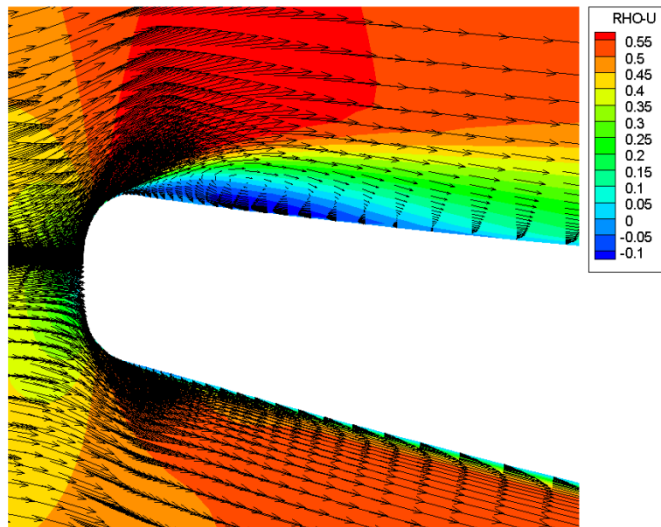


(b)

Figure 5.44: Velocity vectors with ρu contours in the leading edge region of the NASA-PW airfoil (193 x 101 Grid) at the low incidence angle condition for the inlet turbulent viscosity value of 0.009 for (a) fully turbulent flow, and (b) transitional flow using fixed transition onset with $x_{LT} = 0.01$



(a)



(b)

Figure 5.45: Velocity vectors with ρu contours in the leading edge region of the NASA-PW airfoil (193 x 101 Grid) at the low incidence angle condition for the inlet turbulent viscosity value of 10.0 for (a) fully turbulent flow, and (b) transitional flow using fixed transition onset with $x_{LT} = 0.01$

High Incidence Angle Condition

The high incidence angle case will now be considered. At this condition, a large separation bubble formed on the suction surface of the airfoil. Flow visualization was done when the experiments were conducted, which indicated that the flow separated immediately downstream of the airfoil leading edge and extended up to approximately 40% chord. As mentioned earlier, in the experiments chordal incidence angle was not measured and was inferred to be 10° from the cascade geometry. Therefore, in the simulations the chordal incidence angle was methodically adjusted until the best match was obtained with the experimental pressure distribution. This resulted in the cascade inlet flow angle of 7.5° for the high incidence angle case, which was used for all calculations presented below.

Fully Turbulent Flow

Fully turbulent calculations starting right from the leading edge up to the trailing edge of the airfoil were performed using the SA turbulence model. Figure 5.46 presents an example of the lift coefficient for fully turbulent flow over the NASA-PW airfoil at the high incidence angle condition. The solutions were deemed converged when the lift coefficient converged to a steady value. It is seen that the high incidence angle condition generates a positive lift on the airfoil, whereas, the low incidence angle condition generated a negative lift on the airfoil. Figure 5.47 presents an example of the absolute value of the average density residual. The absolute value of the average density residual reached a value greater than 9 indicating that the amount by which the solution was changing was very small. Both indicators show the solution has converged.

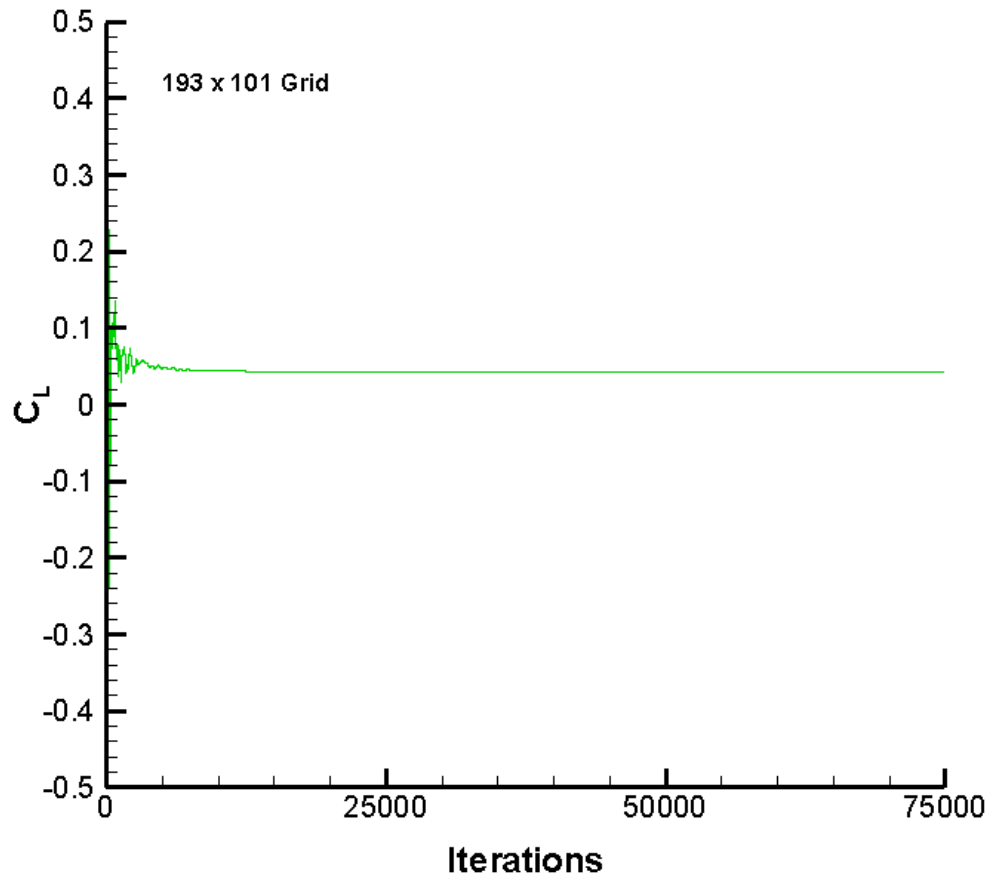


Figure 5.46: Example of NASA-PW airfoil lift coefficient convergence history at the high incidence angle condition for fully turbulent flow

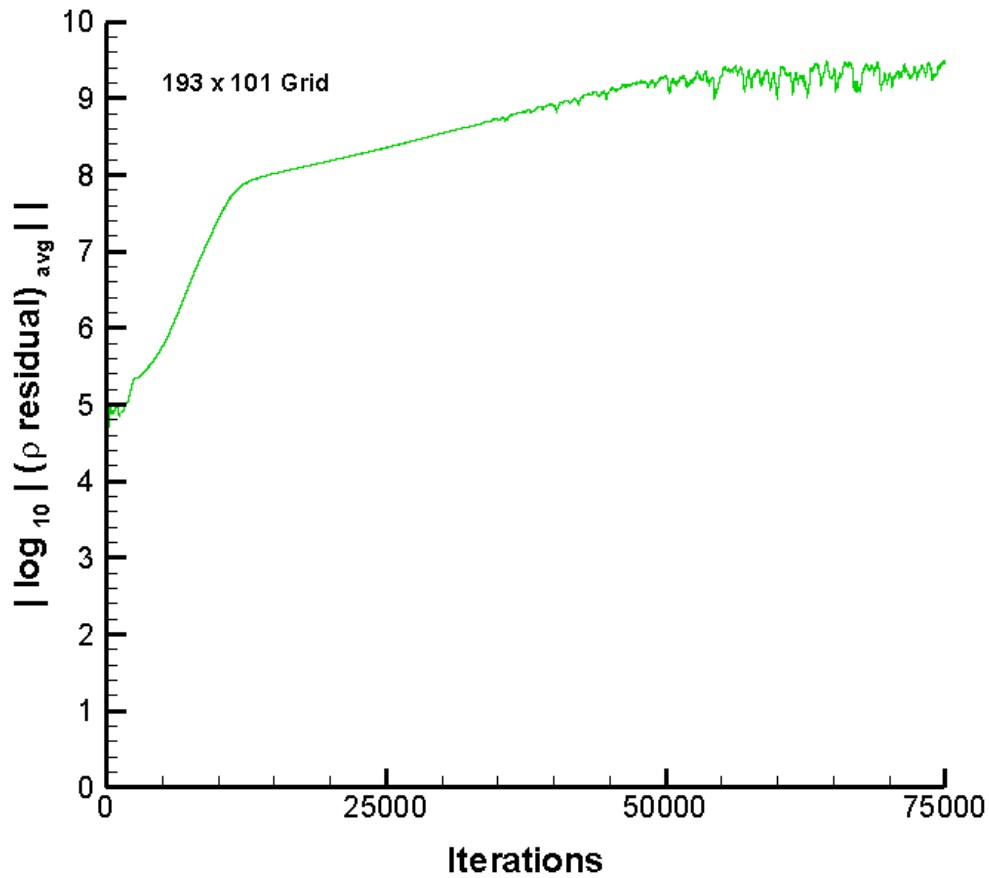


Figure 5.47: Example of the absolute value of the average density residual convergence history for the NASA-PW airfoil at the high incidence angle condition for fully turbulent flow

The steady surface pressure coefficient distribution for the NASA-PW airfoil at the high incidence angle condition is presented in Figure 5.48 for fully turbulent flow. Computations were done using the coarse grid of size 193 x 101 and the dense grid of size 363 x 201 to demonstrate grid independence of the solution. The solutions indicate good correlation between the predicted fully turbulent results and the experimental data. Moreover, the solutions from both the coarse and the dense grids are precisely the same over the entire airfoil surface except for minor differences in the leading edge region of

the suction surface where the flow is separated. Since a large separation bubble exists on the suction surface leading edge region, getting good agreement between the fully turbulent solutions of the coarse and the dense grids in this region was important to generate grid independent solutions for the transitional flow calculations. This was achieved as can be more clearly seen in Figure 5.49. It is observed that the fully turbulent calculations did not capture the pressure plateau exhibited by the experimental data in the leading edge region of the suction surface. These fully turbulent solutions were generated by fixing the inlet turbulent viscosity to 0.009, vorticity based production formulation was used in the SA model, and the streamline curvature correction was not used.

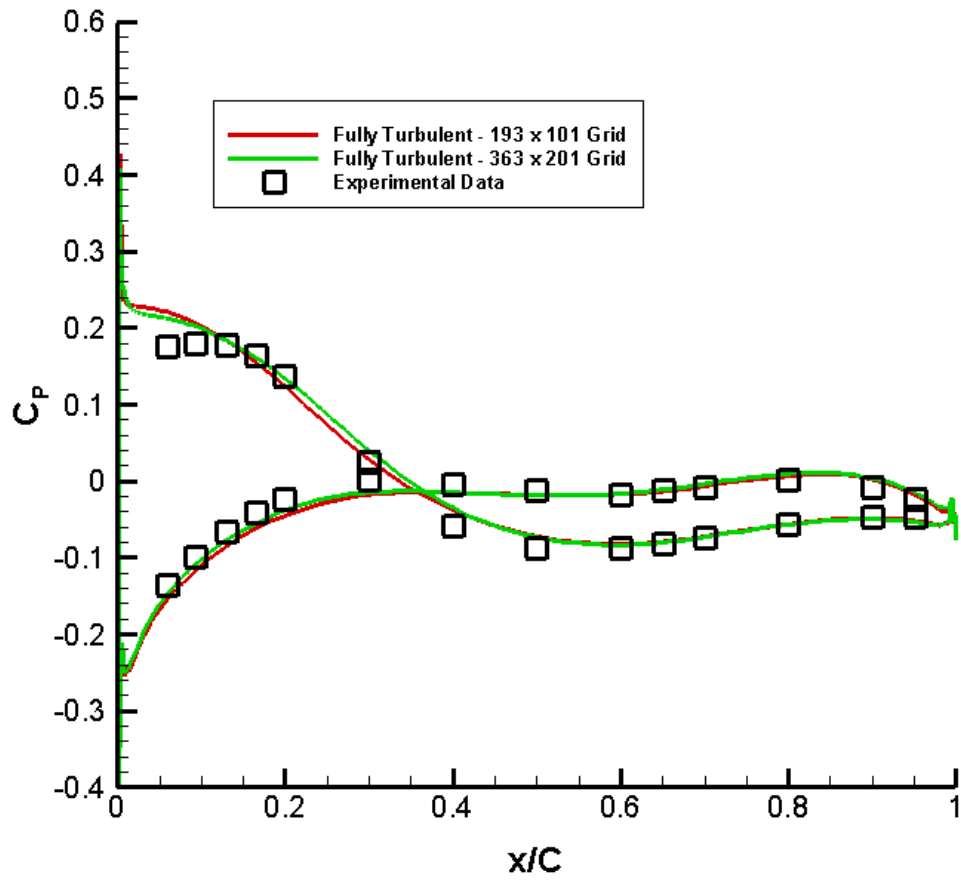


Figure 5.48: Surface pressure coefficient distribution for the NASA-PW airfoil at the high incidence angle condition for fully turbulent flow

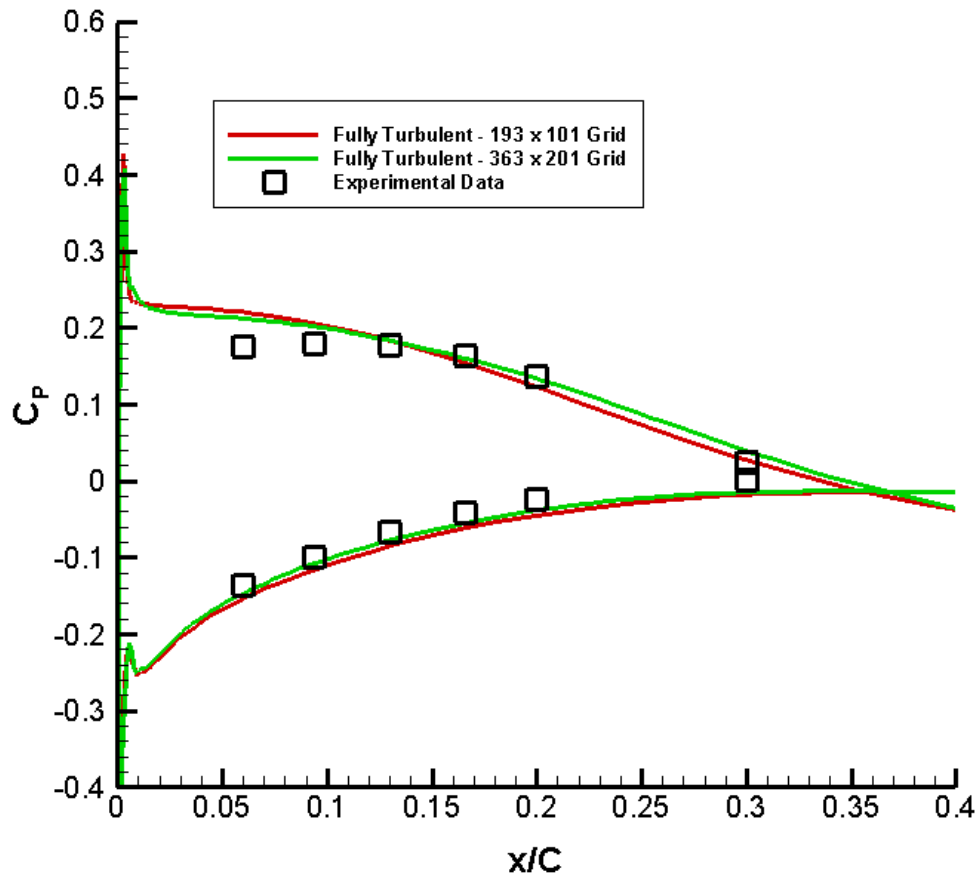


Figure 5.49: Leading edge surface pressure coefficient distribution for the NASA-PW airfoil at the high incidence angle condition for fully turbulent flow

Baldwin-Lomax and Spalart-Allmaras Model

In order to generate solutions more quickly, the BL model and then SA model were used in sequence. The eddy viscosity obtained from the BL model was used as an initial condition for the SA model after conversion to the modified turbulent viscosity, $\tilde{\nu}$. This methodology provided the SA model with realistic initial condition values to start the solution process. It was observed that solution convergence occurred much faster than the traditional approach of using SA model alone. Figure 5.50 shows the lift coefficient

convergence history for the SA model restarted from the initial conditions provided by the BL model. The coarse grid of size 193 x 101 was used for this study. The lift coefficients obtained using the SA model alone and using the combination of BL and SA models were the same, as expected. Figure 5.51 presents the chordwise surface pressure coefficient distribution and Figure 5.52 shows the pressure coefficient distribution in the leading edge region of the airfoil. Both the methodologies gave the exact same pressure distributions. Furthermore, the results are even more encouraging in terms of the solution being the same for the leading edge region due to flow separation occurring on the suction surface and also in terms of time expended in computation with the blended approach. The computations were carried out with inlet turbulent viscosity set to 0.009, vorticity based production formulation used in the SA model, and streamline curvature correction deactivated.

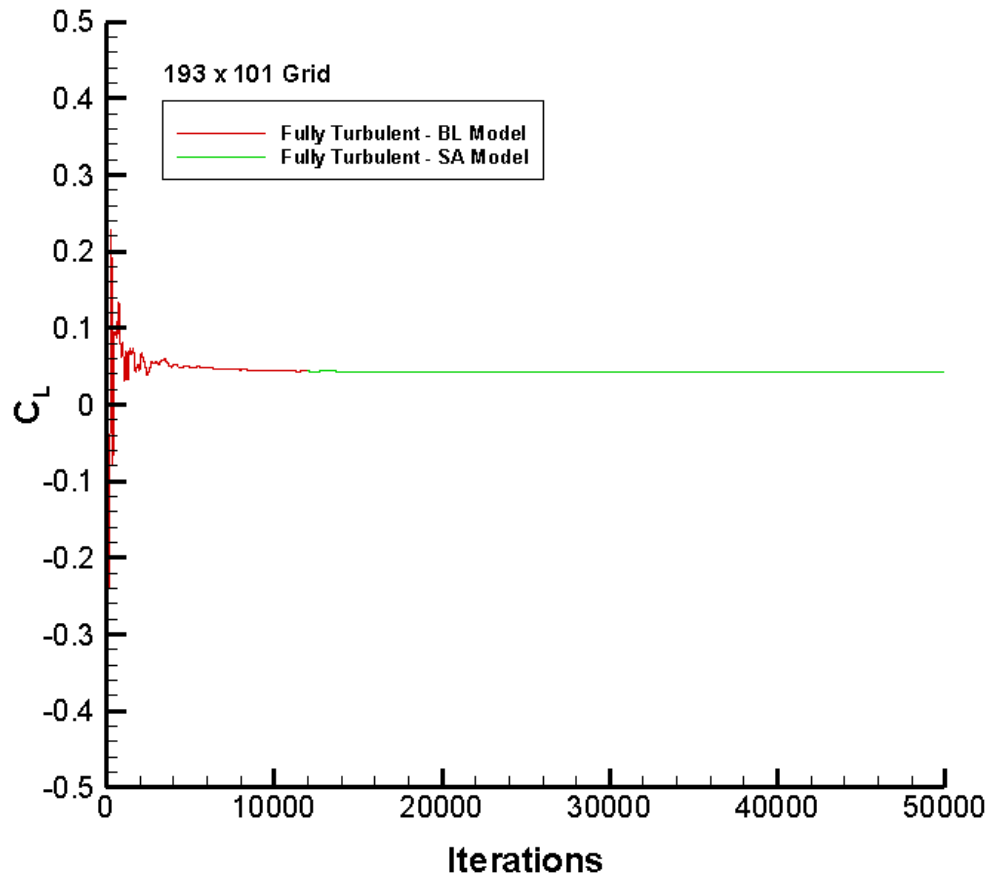


Figure 5.50: NASA-PW airfoil lift coefficient convergence history at the high incidence angle condition for fully turbulent flow with the BL model providing the initial conditions for the SA model

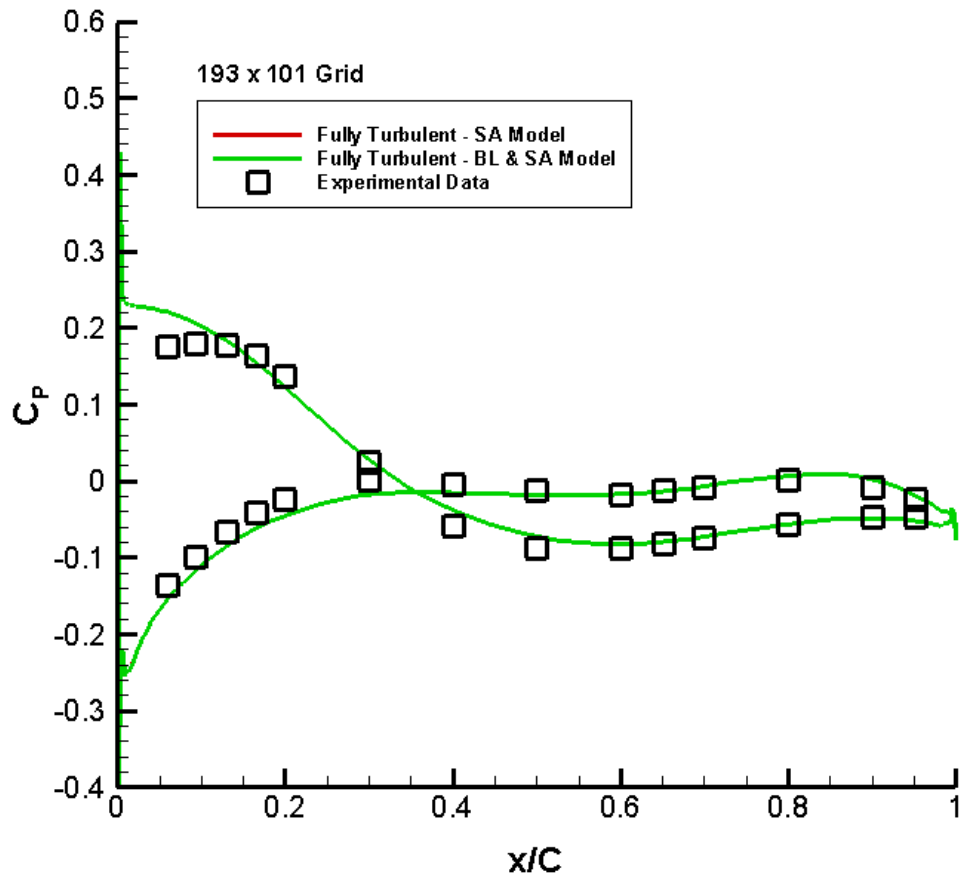


Figure 5.51: Surface pressure coefficient distribution for the NASA-PW airfoil at the high incidence angle condition for fully turbulent flow with the BL model providing the initial conditions for the SA model

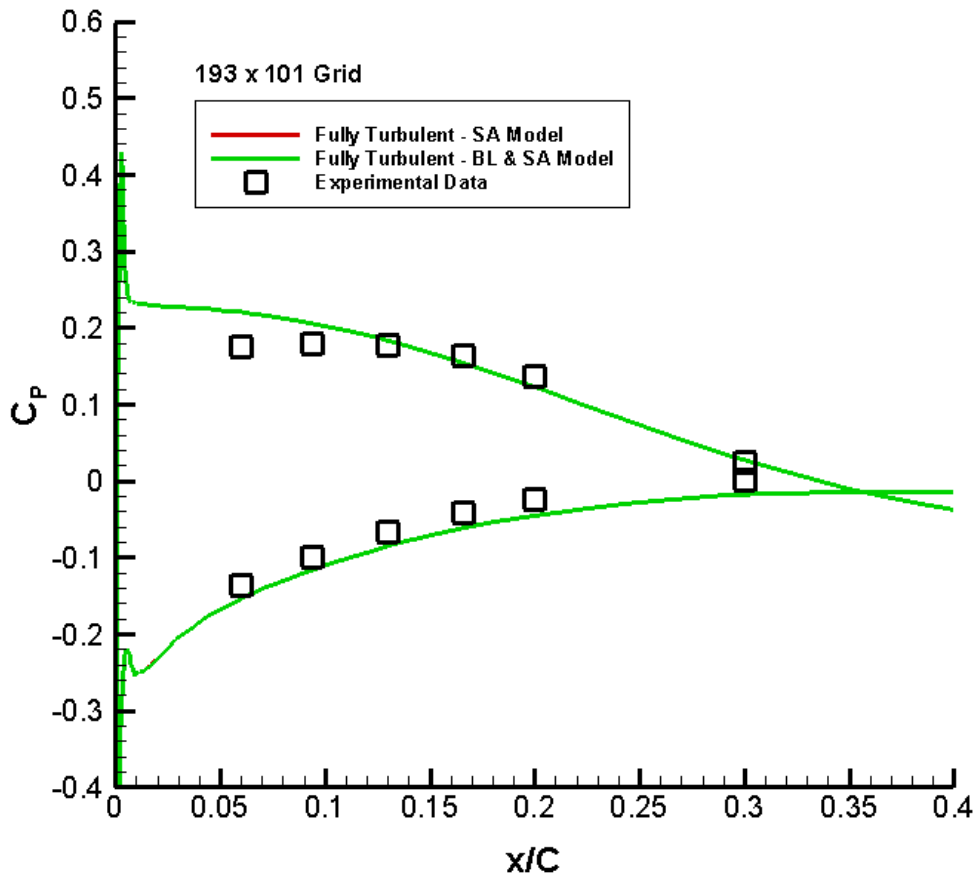


Figure 5.52: Leading edge surface pressure coefficient distribution for the NASA-PW airfoil at the high incidence angle condition for fully turbulent flow with the BL model providing the initial conditions for the SA model

Inlet Turbulent Viscosity Study

The capability added to the code to prescribe different values of turbulent viscosity at the inlet boundary is studied for two largely different values. The coarse grid of size 193 x 101, and inlet turbulent viscosity values of 0.009 and 10.0 were utilized in this investigation. The surface pressure coefficient distribution over the entire airfoil is presented in Figure 5.53 for fully turbulent flow with the different inlet turbulent viscosity values considered. The computations shown used the vorticity based production

formulation in the SA model, and streamline curvature correction was not used. The results for the pressure distribution were nearly identical for both the values of inlet turbulent viscosity except for a small change in the leading edge region of the suction surface where the flow separation starts. Overall, the predicted fully turbulent results have a good correlation with the experimental data. The leading edge region pressure distribution is shown in Figure 5.54. Also, the suction peak pressure coefficient for the inlet turbulent viscosity of 10.0 is slightly higher than that of the inlet turbulent viscosity of 0.009. The pressure distribution in the leading edge region of the suction surface for the high incidence angle condition is in sharp contrast when compared to the low incidence angle case where a huge change was observed in the pressure distribution. The pressure surface pressure coefficient did not have any change due to changes in the turbulent viscosity values at the inlet boundary.

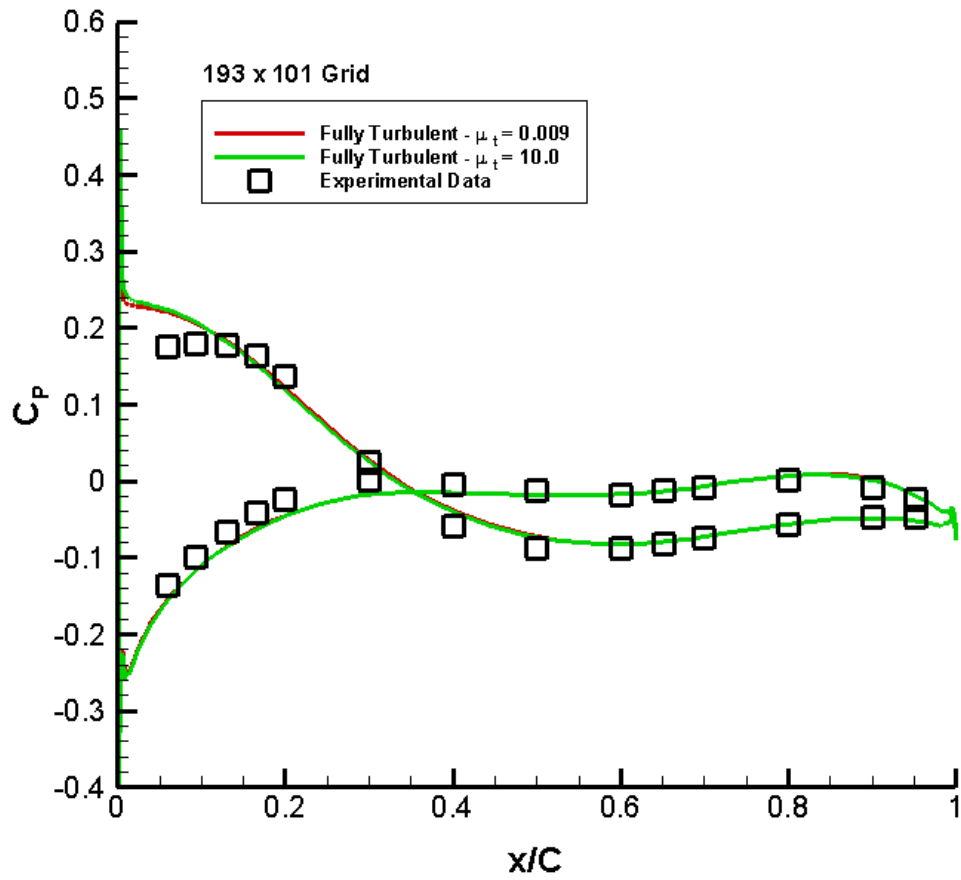


Figure 5.53: Surface pressure coefficient distribution for the NASA-PW airfoil at the high incidence angle condition for fully turbulent flow with different inlet turbulent viscosities

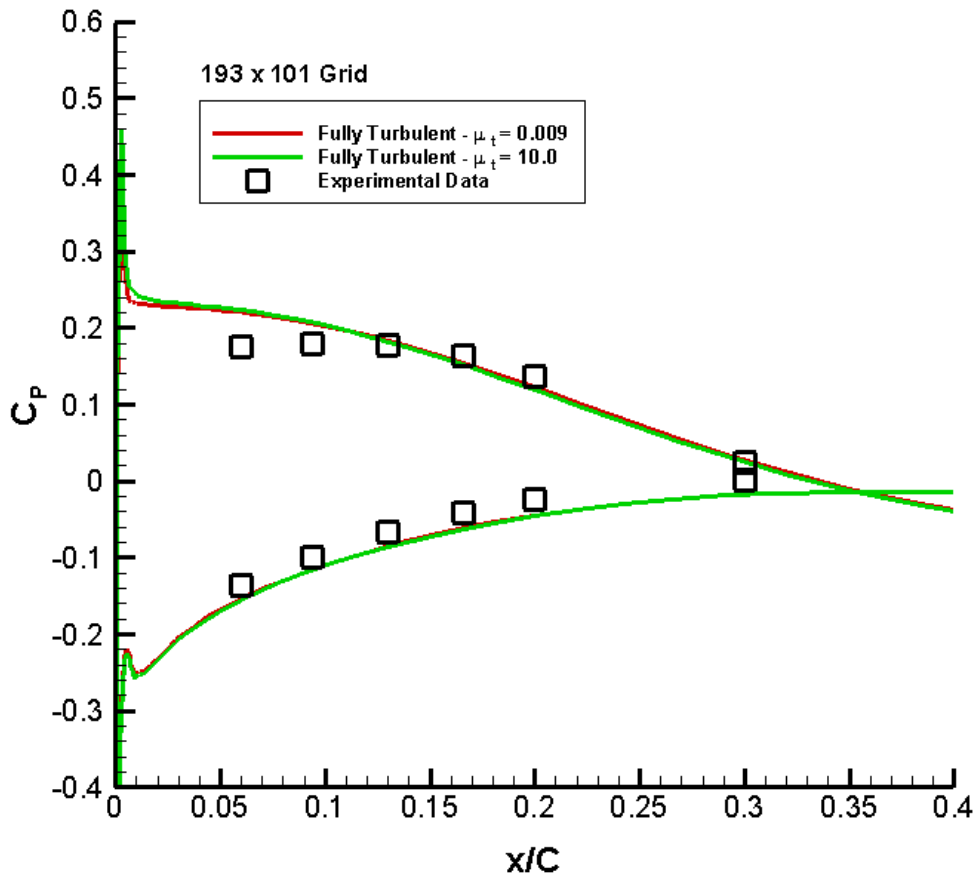


Figure 5.54: Leading edge surface pressure coefficient distribution for the NASA-PW airfoil at the high incidence angle condition for fully turbulent flow with different inlet turbulent viscosities

Production Term Formulation Study in the Spalart-Allmaras Model

The effect of formulating the turbulent production term in the SA model based on the vorticity tensor, and a combination of vorticity and strain tensors is studied for the high incidence angle case. The computations were performed on the coarse grid of size 193 x 101. The chordwise surface pressure distribution is presented below in Figure 5.55. For these computer simulations, the turbulent viscosity at the inlet boundary was set to 0.009, and the streamline curvature correction was not used. As expected, the solution

changed in the leading edge region of the suction surface where the flow is separated, which can be more clearly seen in Figure 5.56. The blended strain-vorticity based production formulation has a higher pressure coefficient for the suction peak pressure and near where the flow separation starts on the suction surface. It is noted that the change in the solution when the strain-vorticity formulation is used is small when compared with the solution using vorticity based formulation and probably the strain-vorticity formulation as recommended in Dacles-Mariani et al. (1995) is more appropriate for vortically intense flows such as in a wingtip vortex.

The flow reattaches after approximately 40% chord on the suction surface. The pressure distribution remains the same in the attached flow region for both the production term formulation methods considered.

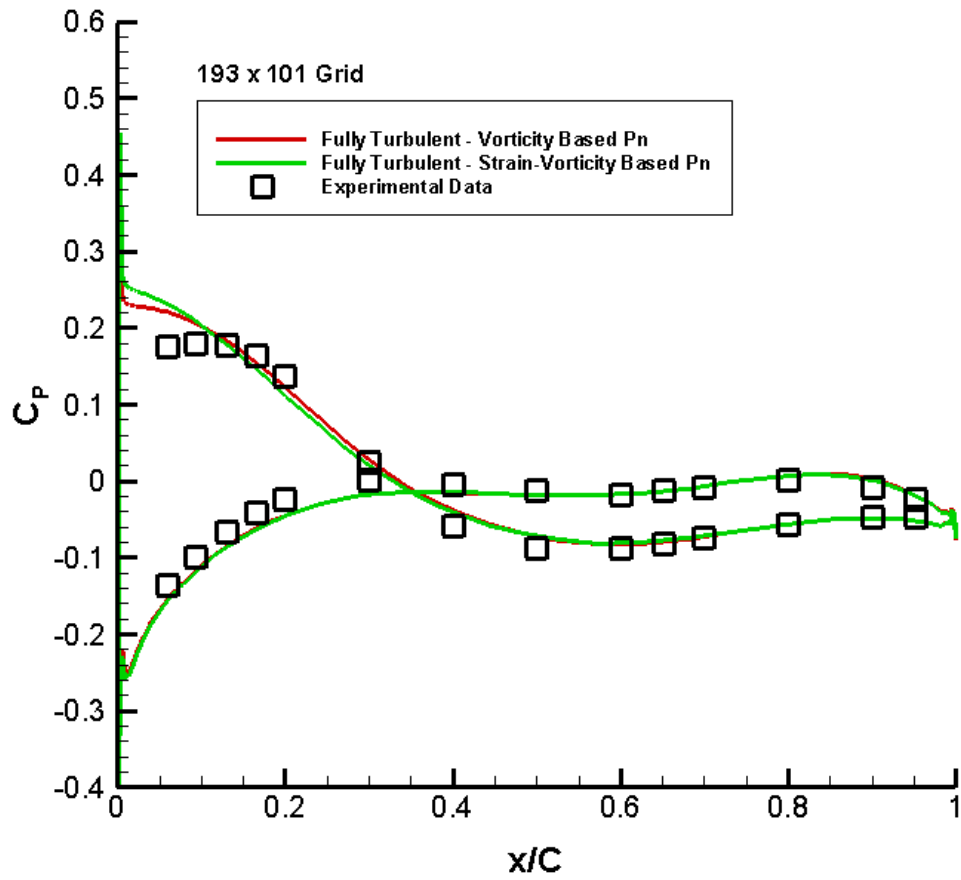


Figure 5.55: Surface pressure coefficient distribution for the NASA-PW airfoil at the high incidence angle condition for fully turbulent flow using different production term formulations in the SA model

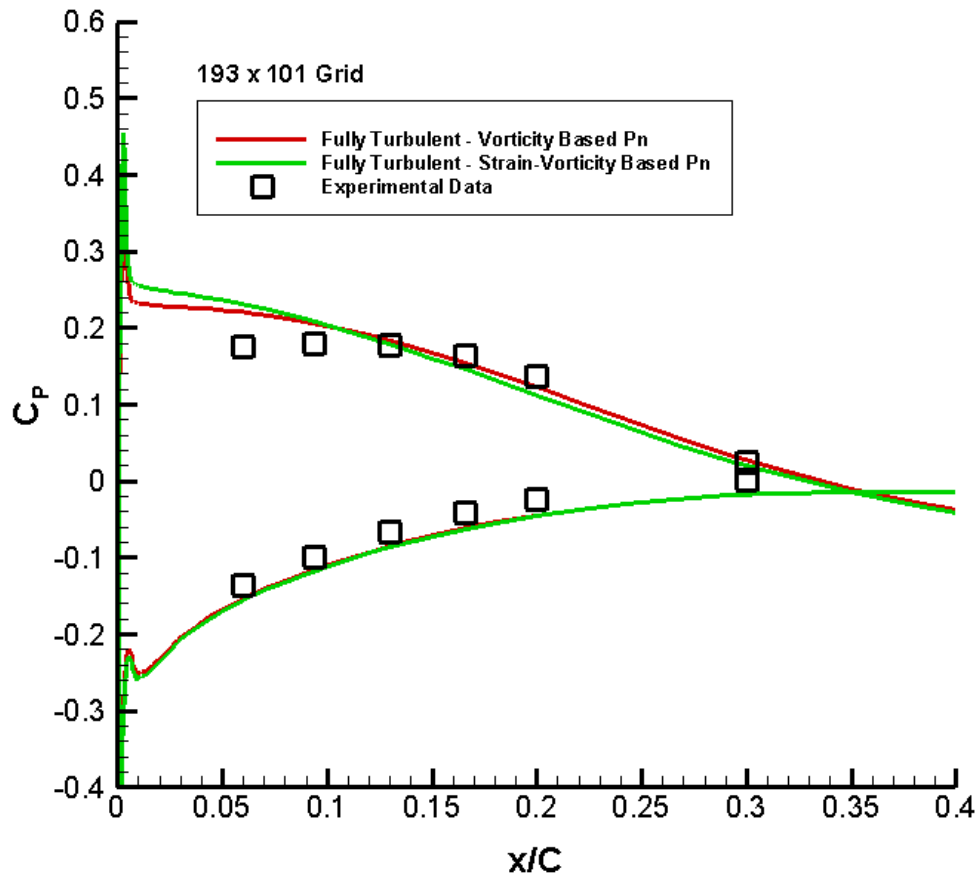


Figure 5.56: Leading edge surface pressure coefficient distribution for the NASA-PW airfoil at the high incidence angle condition for fully turbulent flow using different production term formulations in the SA model

Streamline Curvature Correction Study

The effect of including the streamline curvature correction in the SA model is studied for the high incidence angle case using the coarse grid of size 193 x 101. The pressure distribution over the airfoil surface remained the same in the regions where the flow was attached when compared to the solution where streamline curvature correction was not used as illustrated in Figure 5.57. Change was observed in the leading edge region of the suction surface pressure coefficient distribution where a large separation

bubble exists. The pressure coefficient value decreased with a corresponding decrease in pressure coefficient for the suction peak as shown in Figure 5.58. The same behavior was seen for the low incidence angle condition too. Using streamline curvature correction improved the correlation between the computed solution and the experimental data for the leading edge region. The change is ascribed to the circular leading edge and to the flow having separated from the airfoil surface. However, the change in the solution achieved by including the streamline curvature correction is small. The low incidence angle condition too, did not have a big difference in the results by including the streamline curvature correction. The computations were performed with the inlet turbulent viscosity fixed at 0.009, and vorticity based production formulation was used in the SA model.

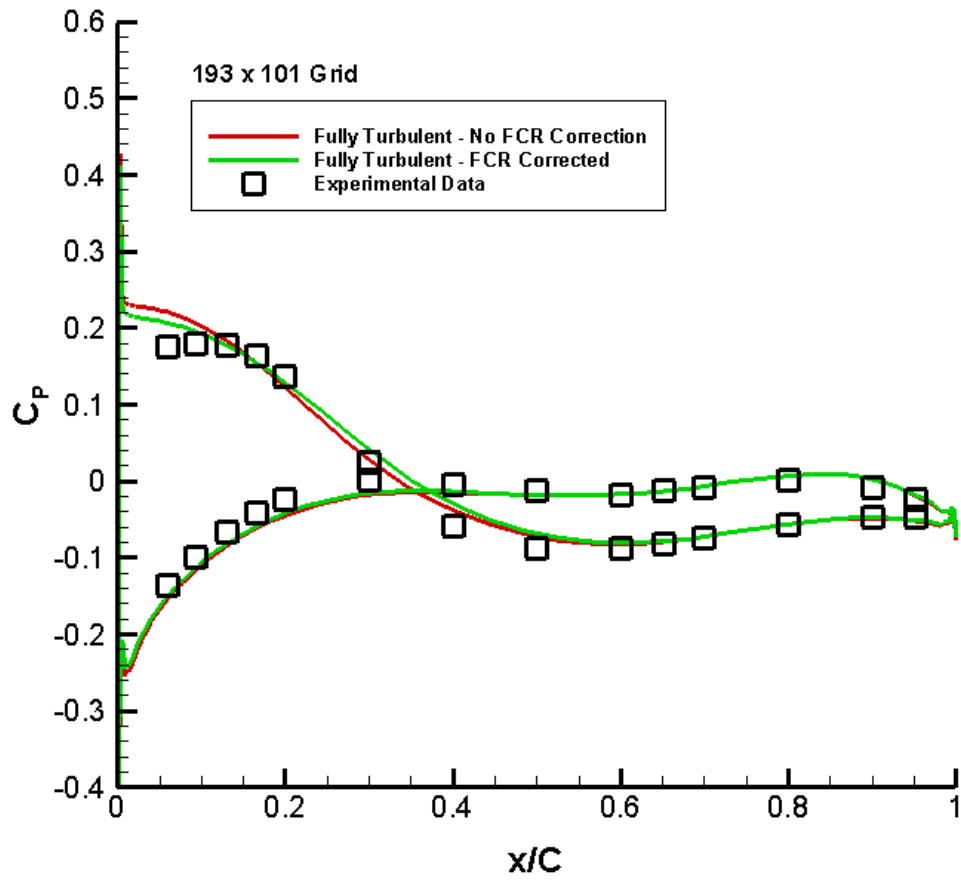


Figure 5.57: Surface pressure coefficient distribution for the NASA-PW airfoil at the high incidence angle condition for fully turbulent flow with and without streamline curvature correction

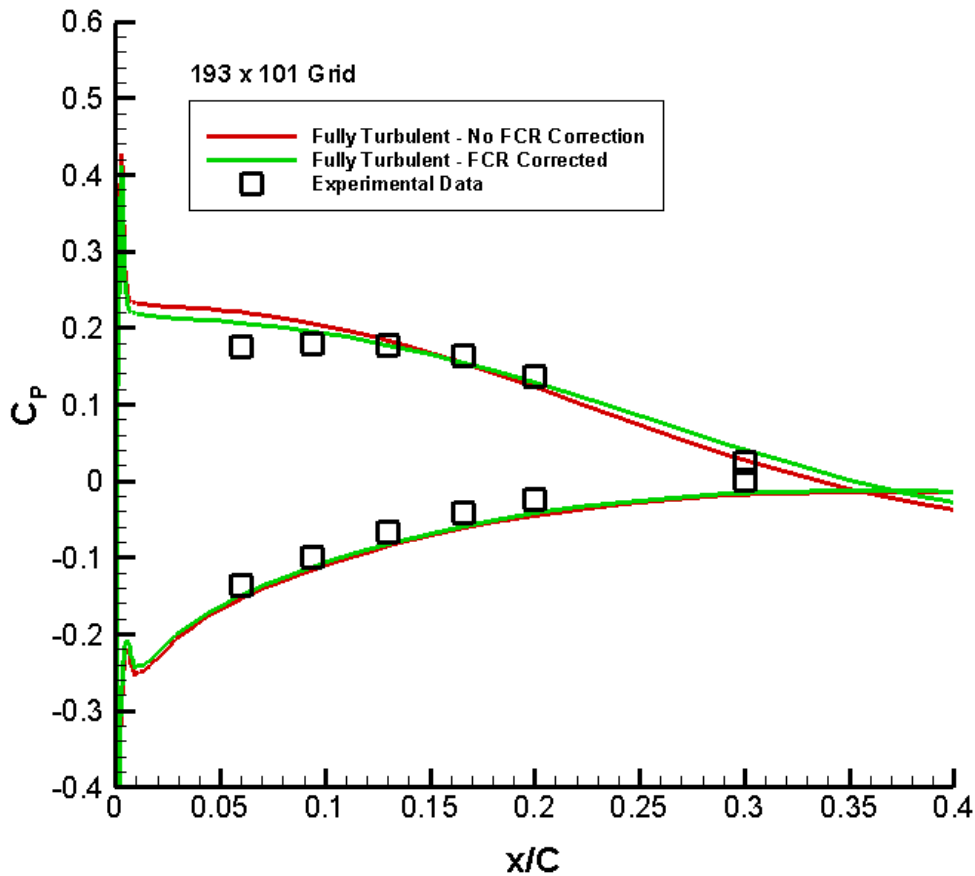


Figure 5.58: Leading edge surface pressure coefficient distribution for the NASA-PW airfoil at the high incidence angle condition for fully turbulent flow with and without streamline curvature correction

Transition

Transitional flow calculations were performed for the high incidence angle case by restarting the fully turbulent solutions. The simulations were done using the coarse and the dense grids. The DN model was activated to compute separated flow transition. Figure 5.59 shows an example of the lift coefficient convergence history for transitional flow calculations restarted from the fully turbulent solution. The lift coefficient for the transition calculations reaches a steady state after the initial transients due to the

activation of the transition model have damped out. The average density residual convergence history is presented in Figure 5.60 for the fully turbulent flow and the transitional flow. It is observed that the absolute value of the average density residual for the transition calculations and the fully turbulent calculations are of the same order, and are above 9. The non-oscillatory, steady C_L , and the absolute value of the average density residual being greater than 9 both indicate the solution are converged.

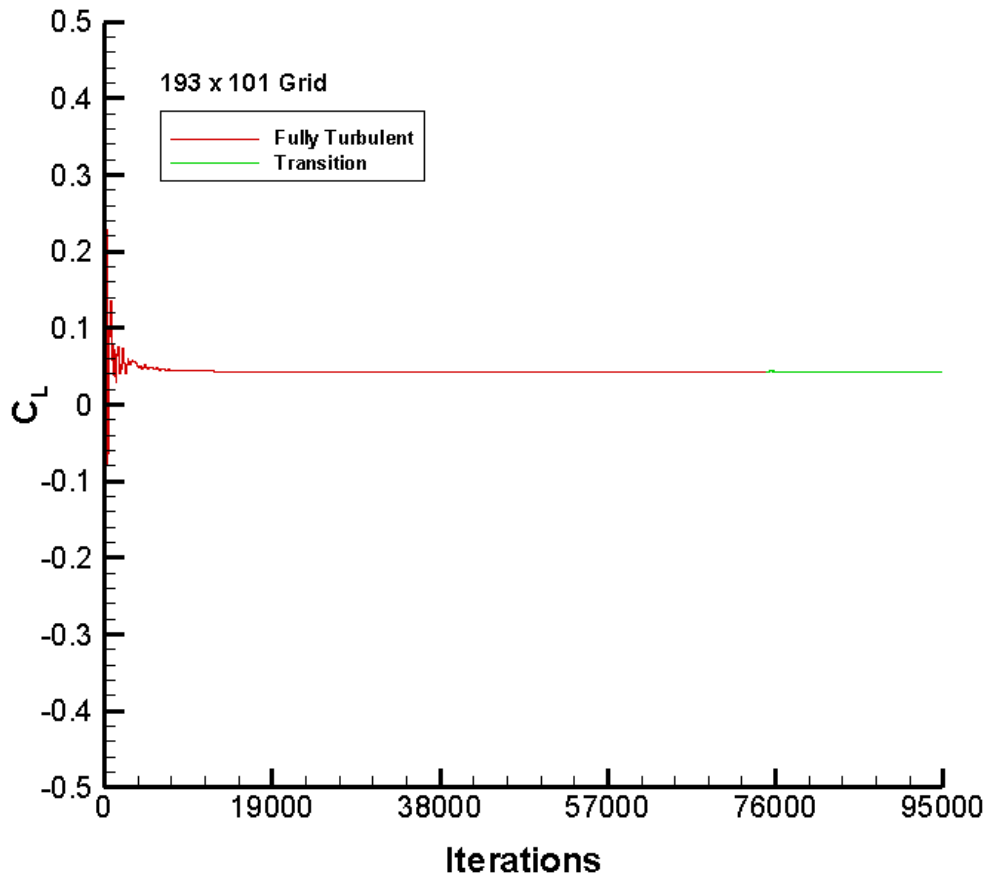


Figure 5.59: Example of NASA-PW airfoil lift coefficient convergence history at the high incidence angle condition for turbulent flow with transition

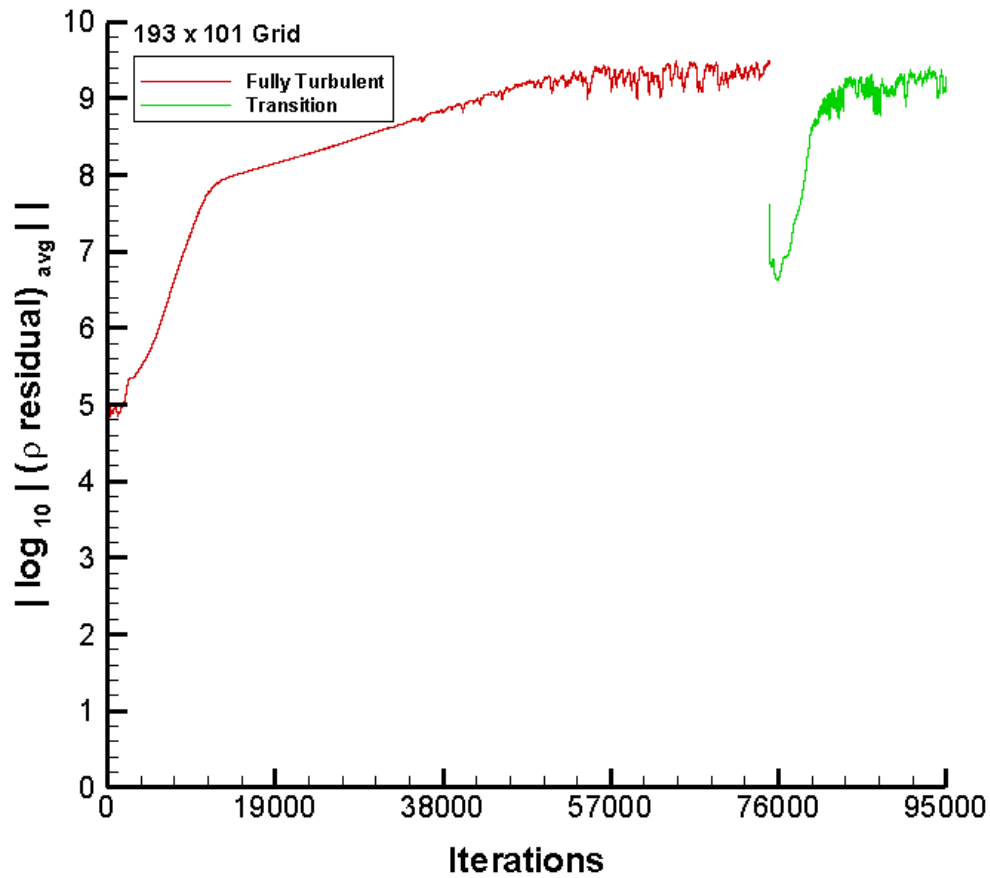


Figure 5.60: Example of the absolute value of the average density residual convergence history for the NASA-PW airfoil at the high incidence angle condition for turbulent flow with transition

Experiments at the high incidence angle condition for the NASA-PW airfoil showed that there was a large separation bubble in the leading edge region of the suction surface. The separated flow region can be seen clearly with the help of ρu contours, which is presented in Figure 5.61. The suction surface of the airfoil shows a large area of negative momentum because of the flow separation. It also indicates the highly complicated flow physics in this region, which must be captured by the turbulence and transition models. Moreover, a large gradient in momentum takes place above the suction

surface leading edge region. The pressure surface does not show any significant flow feature except in the leading edge region where a large momentum gradient is seen due to flow stagnation.

The phenomenon of flow separation and recirculation, which is the subject of study in this research, is illustrated more clearly in Figure 5.62, which shows the leading edge contours of ρu . The flow undergoes a drastic change in the streamwise momentum as it comes in contact with the leading edge. The separation bubble is seen as the blue region where the ρu contours have negative values, and covers a significant part of the airfoil suction surface. Strong recirculating flow occurs inside the large separation bubble that forms in the leading edge region of the suction surface for the high incidence angle case, which can be observed through the velocity vectors in Figure 5.63. In this figure, velocity vectors with ρu contours are shown for the leading edge region for fully turbulent and transitional flow computations. The changes that occur when transitional flow is computed are very small and are concentrated very close to the suction surface leading edge region, and it is difficult to distinguish between the ρu contours and vectors of fully turbulent and transitional flow from Figure 5.63. Also, in the wake of the airfoil a small separation region is formed, which is seen as the blue region with negative values of ρu contours, as the flow transitions from being wall bounded to the free-shear layer behind the airfoil trailing edge.

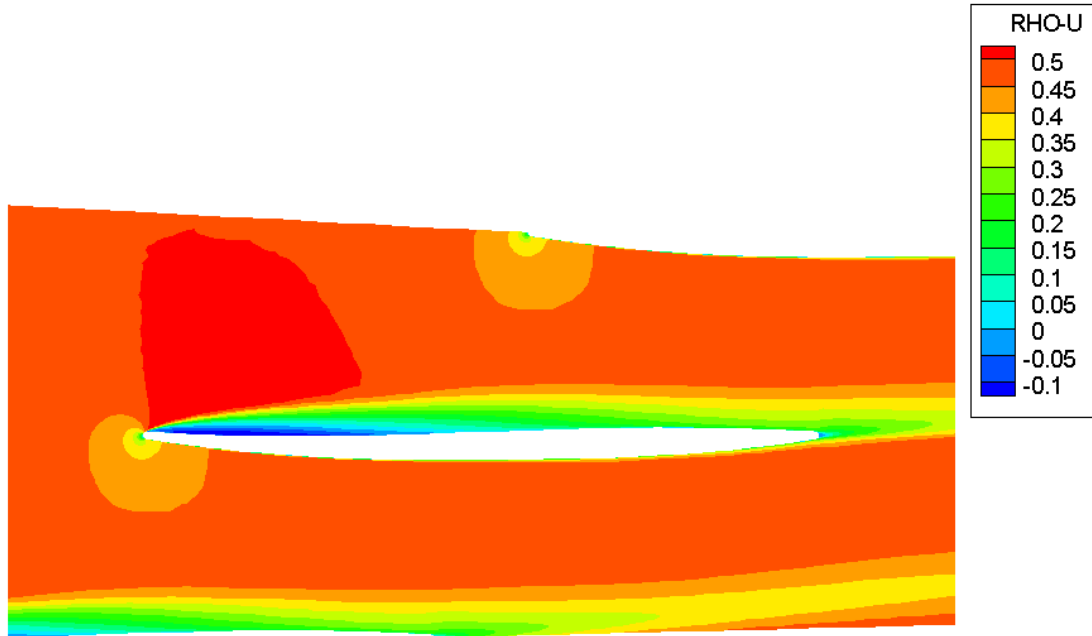


Figure 5.61: Example of ρu contours for the NASA-PW airfoil (193 x 101 Grid) at the high incidence angle condition for transitional flow using fixed transition onset with $x_{LT} = 0.08$

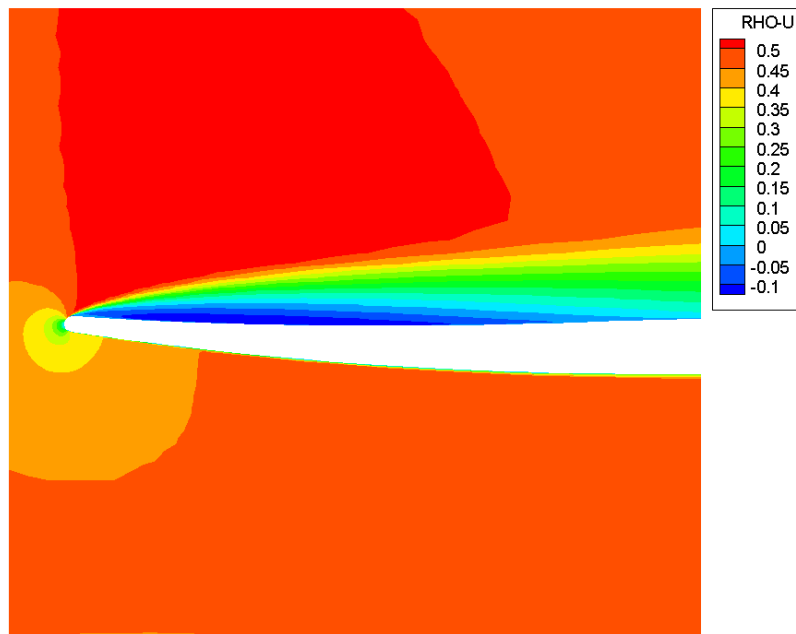
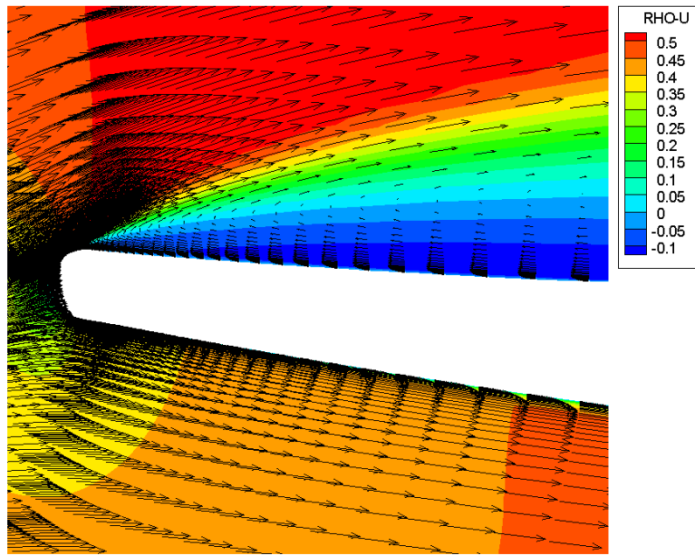
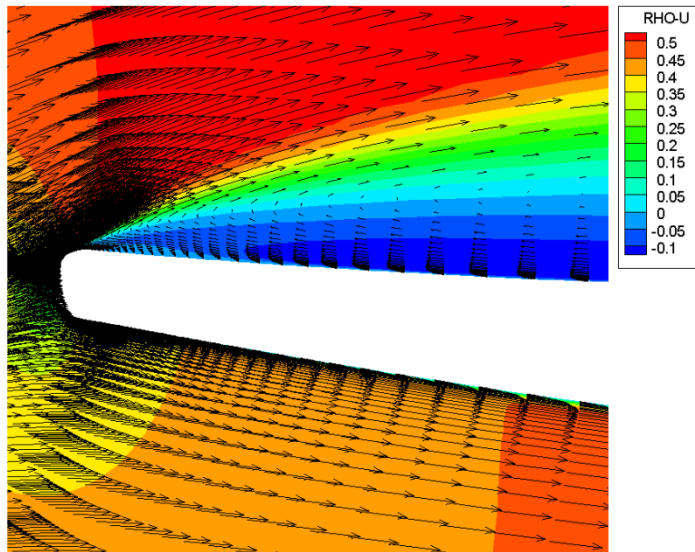


Figure 5.62: Example of ρu contours in the leading edge region of the NASA-PW airfoil (193 x 101 Grid) at the high incidence angle condition for transitional flow using fixed transition onset with $x_{LT} = 0.08$



(a)



(b)

Figure 5.63: Example of velocity vectors with ρu contours in the leading edge region of the NASA-PW airfoil (193 x 101 Grid) at the high incidence angle condition for (a) fully turbulent flow, and (b) transitional flow using fixed transition onset with $x_{LT} = 0.08$

The surface pressure coefficient distribution for turbulent and transitional flow computed on the coarse grid of size 193 x 101 and the dense grid of size 363 x 201 are presented in Figure 5.64. Again, the intermittency correlation of the DN model was used on the suction surface for computing transition. For these transition calculations, the inlet turbulent viscosity was set to 0.009, vorticity based production formulation was used in the SA model, and streamline curvature correction was not used. The variation of the reattachment location for the two grids is presented in Table 5.3 along with the separation point, and the streamwise transition onset and transition termination locations. A fixed transition length of $x_{LT} = 0.08$ was used in the transition calculations. Figure 5.64 shows that the transition calculations performed with the two grids have only small differences in the suction surface leading edge region and demonstrate the grid independence of the solutions. Moreover, it is observed that the correlation of the fully turbulent predictions with the experimental data is not as good as for the low incidence angle condition. In the leading edge region of the suction surface large deviations between the experimental data and turbulent predictions occur where the flow is separated. Fixed point transition calculations were performed by choosing the transition onset location immediately downstream of the point of flow separation. The transition end point was varied in order to get good correlation with the experimental data points in the leading edge region. It was found that for a fixed transition onset point, the pressure plateau increased in size as the transition length became longer, and simultaneously the pressure coefficient value decreased. The formation of a pressure plateau in the leading edge region of the suction surface can be seen more clearly in Figure 5.65 for $x_{LT} = 0.08$, which gives the best correlation that could be obtained with the experimental data in the leading edge region.

However, the pressure plateau length is less than the pressure plateau length exhibited by the experimental data. The pressure plateau is also slightly above the experimental data. Moreover, the suction peak pressure coefficient value is the lowest for this transition length. The transition length could not be increased more than $x_{LT} = 0.08$. Longer transition lengths generated oscillatory solutions on the dense grid. Unlike the low incidence angle case, for the high incidence angle condition, Mayle's transition length model resulted in an oscillatory flow field. This was because the transition onset point predicted by the Mayle model was too far into the separation region.

The size of the separation bubble predicted on the dense grid was slightly bigger than that predicted on the coarse grid. On the coarse grid, the separation bubble size in Cartesian coordinates was 0.4416C, or in streamwise coordinates was 0.4802, and on the dense grid, the separation bubble size in Cartesian coordinates was 0.4574C, or in streamwise coordinates was 0.4819. The predicted reattachment points were slightly farther downstream than the experimental value. The experimentally determined reattachment point was 0.4C. The predicted separation and reattachment points were the same for the fully turbulent and transitional predictions for the individual coarse and the dense grids with only minor differences in the values between the two grids, which are given in Table 5.3. It is observed that the transition calculations blend back into the fully turbulent calculations of the respective grids around where the bubble reattaches on the suction surface.

As for the low incidence angle case, no changes in the pressure coefficient were found on the pressure surface for changes in the suction surface transition onset point or transition lengths. Additionally, little change was found between the fully turbulent

pressure coefficient and the transitional flow pressure coefficient. The pressure surface transition onset point was specified as 0.1711C for use with the transition model of Solomon et al. (1996).

Table 5.3: Transitional flow parameters for the NASA-PW airfoil at the high incidence angle condition

Grid Size	Transition Model	x_s	x_r	S_s	S_r	x_t	x_T	x_{LT}
193 x 101	None, Fully Turbulent	0.0035	0.4451	0.0093	0.4895	NA	NA	NA
	Fixed	0.0035	0.4451	0.0093	0.4895	0.01	0.09	0.08
363 x 201	None, Fully Turbulent	0.0038	0.4612	0.0097	0.4916	NA	NA	NA
	Fixed	0.0038	0.4612	0.0097	0.4916	0.01	0.09	0.08

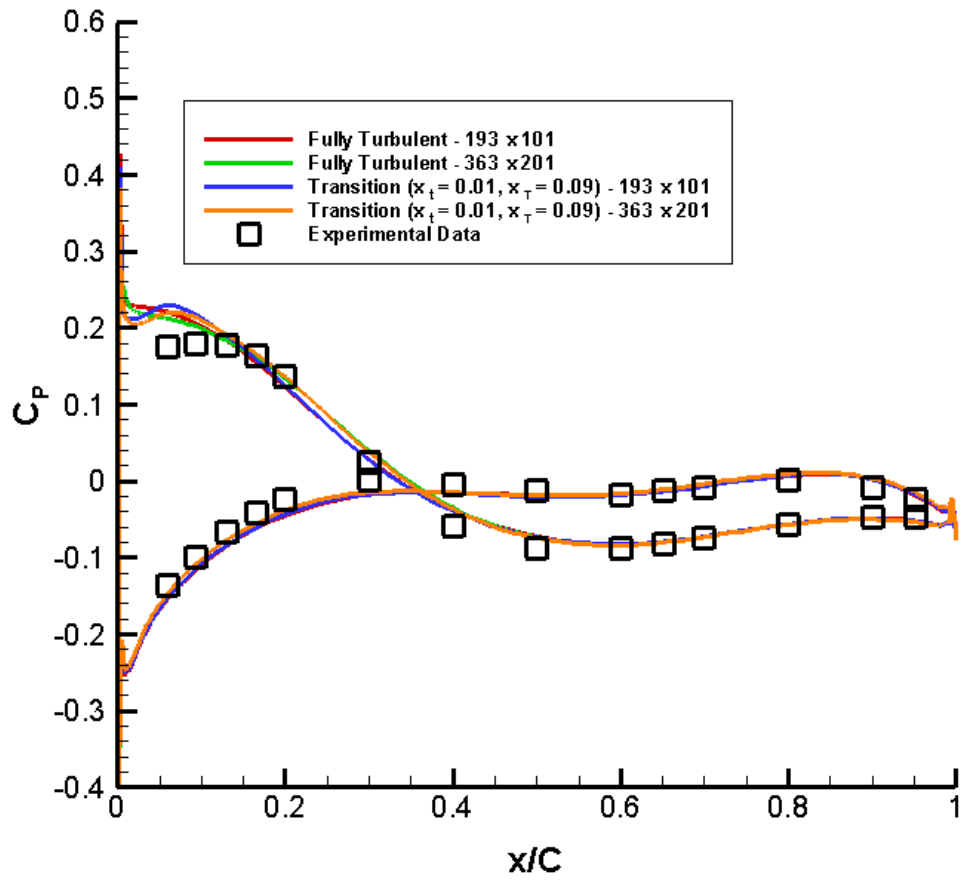


Figure 5.64: Surface pressure coefficient distribution for the NASA-PW airfoil at the high incidence angle condition for turbulent flow and transitional flow with fixed transition onset

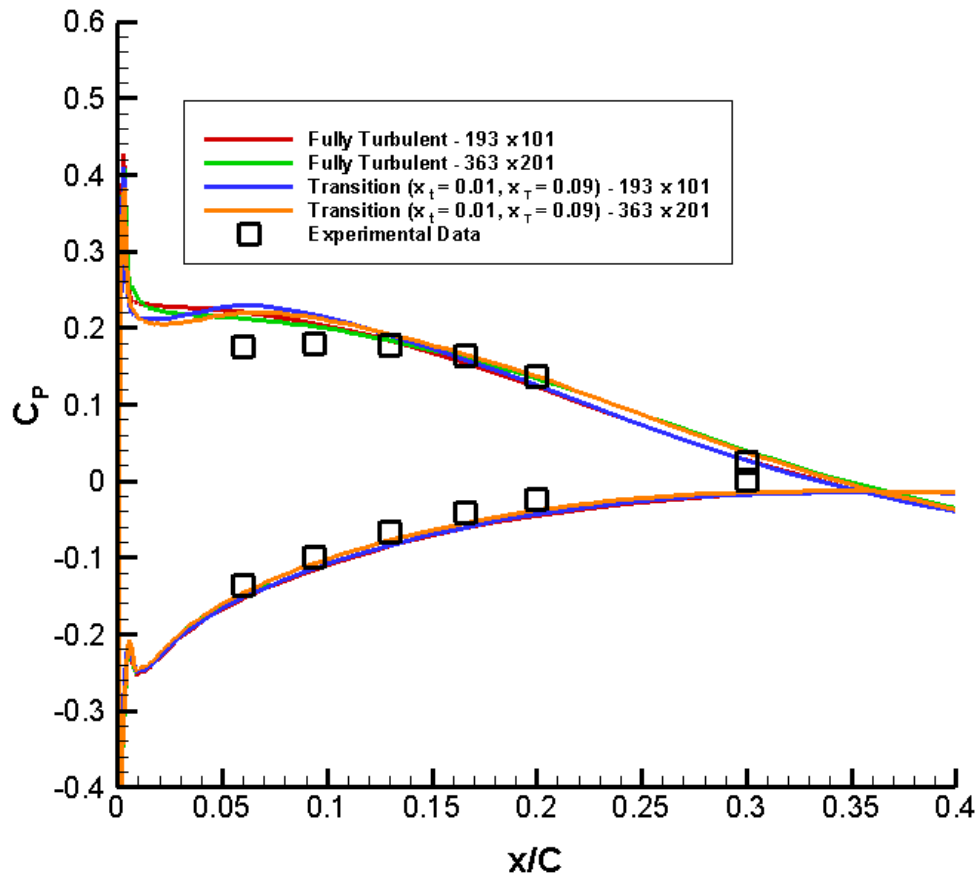


Figure 5.65: Leading edge surface pressure coefficient distribution for the NASA-PW airfoil at the high incidence angle condition for turbulent flow and transitional flow with fixed transition onset

Inlet Turbulent Viscosity Study

The effect of inlet turbulent viscosity was investigated on transitional flow for the high incidence angle case. The coarse grid of size 193 x 101, and inlet turbulent viscosity values of 0.009 and 10.0 were used in this study. The chordwise surface pressure coefficient distribution for the fixed transition length model of $x_{LT} = 0.08$ is presented in Figure 5.66. The computations shown were carried out using the vorticity based production formulation in the SA model, and streamline curvature correction

deactivated. A pressure plateau formed for both the values of inlet turbulent viscosity in the leading edge region of the suction surface where the flow is separated. However, unlike the low incidence angle case, using a higher value of inlet turbulent viscosity for the high incidence angle condition did not have a significant influence on the suction surface leading edge pressure distribution. The pressure plateau size remained the same for both the values of inlet turbulent viscosities considered. The leading edge pressure distribution is shown in Figure 5.67. The separation point and the reattachment point are the same for the fully turbulent and transition calculations and also for the two values of the inlet turbulent viscosity as shown in Table 5.4 along with the points of transition onset and transition termination. The pressure surface transition onset point is the same as the previous case described above.

The pressure surface pressure coefficient showed no change in the solution when transition was computed compared to the fully turbulent solution. Moreover, the fully turbulent and transition solutions for both the values of inlet turbulent viscosity are the same.

Table 5.4: Transitional flow parameters for the NASA-PW airfoil at the high incidence angle condition for different values of inlet turbulent viscosity

μ_t	Transition Model	x_s	x_r	S_s	S_r	x_t	x_T	x_{LT}
0.009	None, Fully Turbulent	0.0035	0.4451	0.0093	0.4895	NA	NA	NA
	Fixed	0.0035	0.4451	0.0093	0.4895	0.01	0.09	0.08
10.0	None, Fully Turbulent	0.0035	0.4451	0.0093	0.4895	NA	NA	NA
	Fixed	0.0035	0.4451	0.0093	0.4895	0.01	0.09	0.08

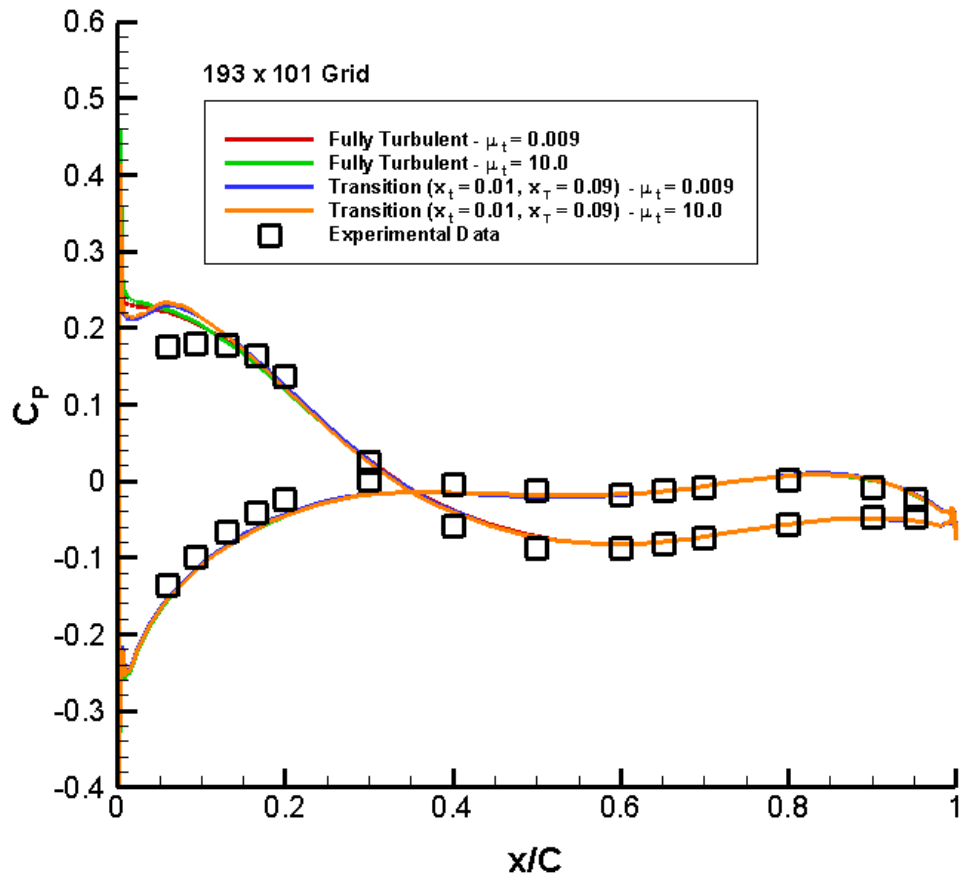


Figure 5.66: Surface pressure coefficient distribution for the NASA-PW airfoil at the high incidence angle condition for turbulent flow and transitional flow with fixed transition onset for different inlet turbulent viscosities

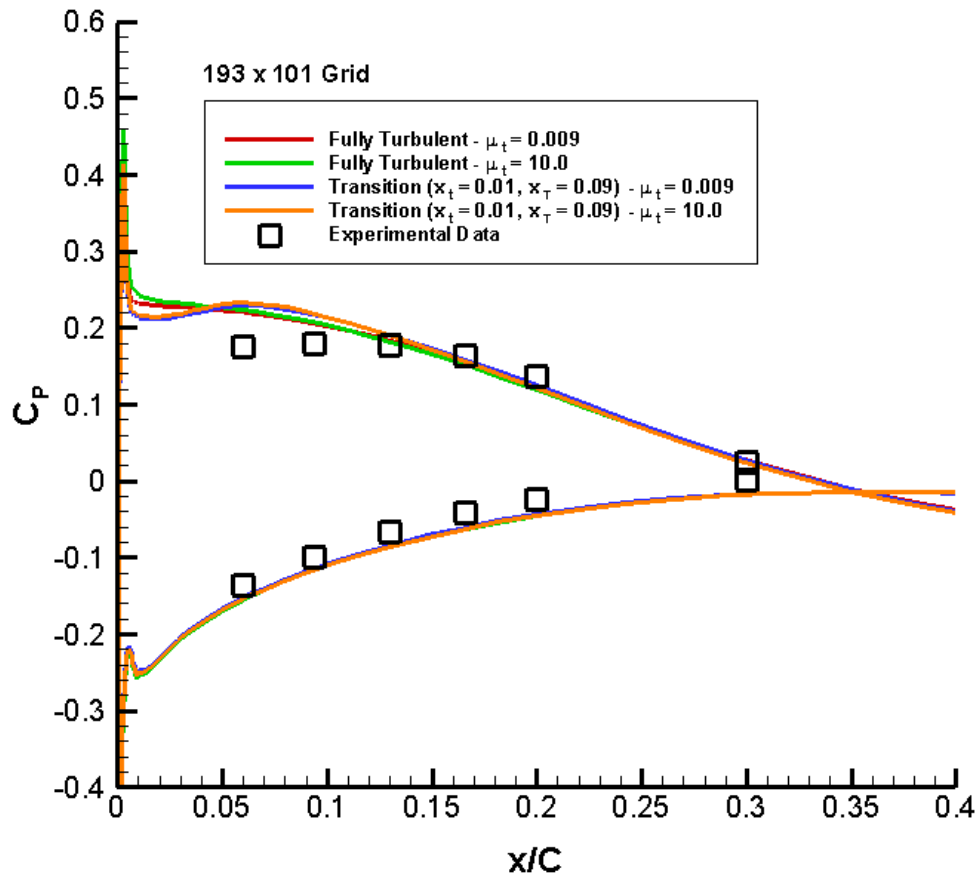


Figure 5.67: Leading edge surface pressure coefficient distribution for the NASA-PW airfoil at the high incidence angle condition for turbulent flow and transitional flow with fixed transition onset for different inlet turbulent viscosities

Production Term Formulation Study in the Spalart-Allmaras Model

The effect of formulating the production term based on only vorticity, and blended strain-vorticity is investigated for transitional flow over the NASA-PW airfoil at the high incidence angle condition. The computations were carried out using the coarse grid of size 193 x 101. Figure 5.68 shows the comparison of fully turbulent and transitional flow pressure coefficient distribution over the entire airfoil surface with the experimental data. Overall, the solutions for both the production formulations have a

good correlation with the experimental data except in the transition zone, which is near the leading edge region of the suction surface where deviations still exist between the computed transition solutions and the experimental data. The transitional flow computations for the fixed transition length model of $x_{LT} = 0.08$ were carried out with inlet turbulent viscosity set to 0.009, and streamline curvature correction was not used. The pressure plateau formed with the classical vorticity based production formulation gives only slightly better agreement in the leading edge region of the suction surface where the flow separation occurs than the blended strain-vorticity based production formulation. This can be seen more clearly in Figure 5.69. This points out that the blended strain-vorticity formulation as recommended in Dacles-Mariani et al. (1995) is more appropriate for more vortical flows. The length of the pressure plateau remained the same for both the production formulations. The strain-vorticity based production formulation predicted a slightly higher value for the peak pressure coefficient on the suction surface for both the fully turbulent as well as the transition calculations.

There was no change in the separation and reattachment points for the fully turbulent and transition predictions and also for the two production formulations used, which are presented in Table 5.5 along with the transition onset and transition termination points in the streamwise coordinates, and the streamwise length of transition. The size of the separation bubble in streamwise coordinates was 0.4802. In Cartesian coordinates, the separation bubble size was 0.4416C. The transition solutions blend into the fully turbulent solutions approximately near the reattachment zone.

For the flow to transition from laminar to turbulent on the pressure surface, the transition onset point was specified as 0.1711C for use with the transition model of

Solomon et al. (1996). Again, there was no influence on the pressure distribution of the pressure surface due to transition for both the production formulations. Moreover, no change in the solution was observed between the fully turbulent and transition calculations.

Table 5.5: Transitional flow parameters for the NASA-PW airfoil at the high incidence angle condition for different production term formulations in the SA model

Pn Term	Transition Model	x_s	x_r	S_s	S_r	x_t	x_T	x_{LT}
Vorticity	None, Fully Turbulent	0.0035	0.4451	0.0093	0.4895	NA	NA	NA
	Fixed	0.0035	0.4451	0.0093	0.4895	0.01	0.09	0.08
Strain-Vorticity	None, Fully Turbulent	0.0035	0.4451	0.0093	0.4895	NA	NA	NA
	Fixed	0.0035	0.4451	0.0093	0.4895	0.01	0.09	0.08

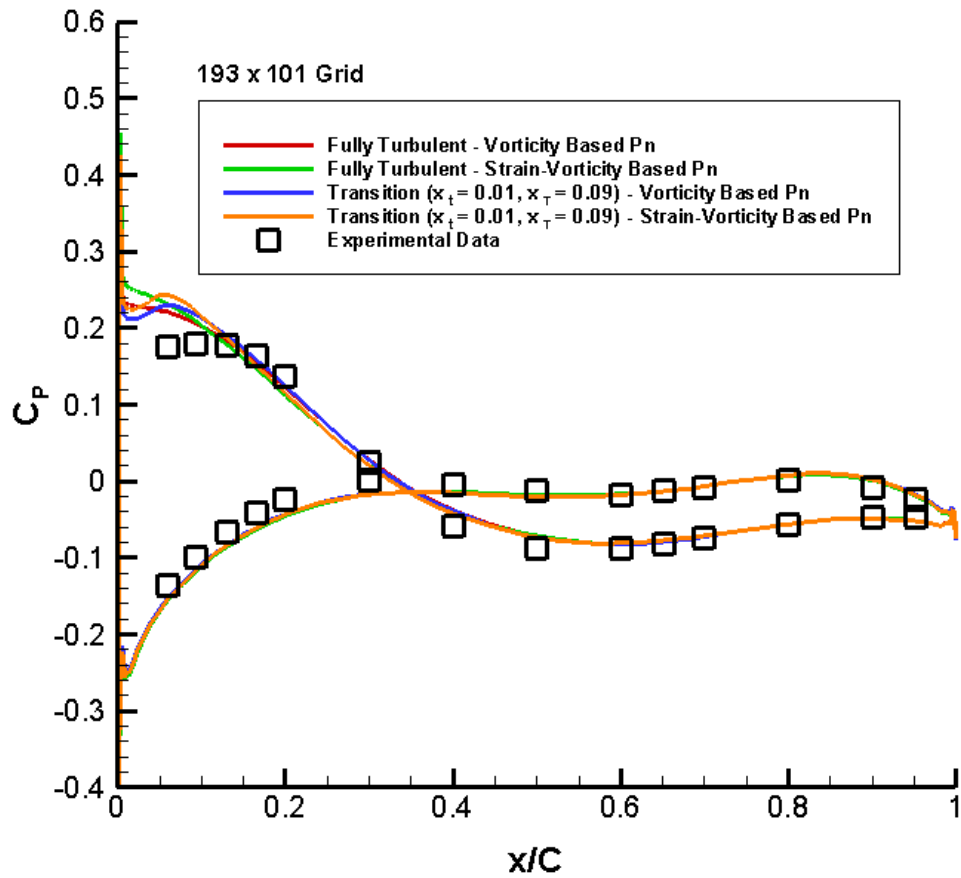


Figure 5.68: Surface pressure coefficient distribution for the NASA-PW airfoil at the high incidence angle condition for turbulent flow and transitional flow with fixed transition onset using different production term formulations in the SA model

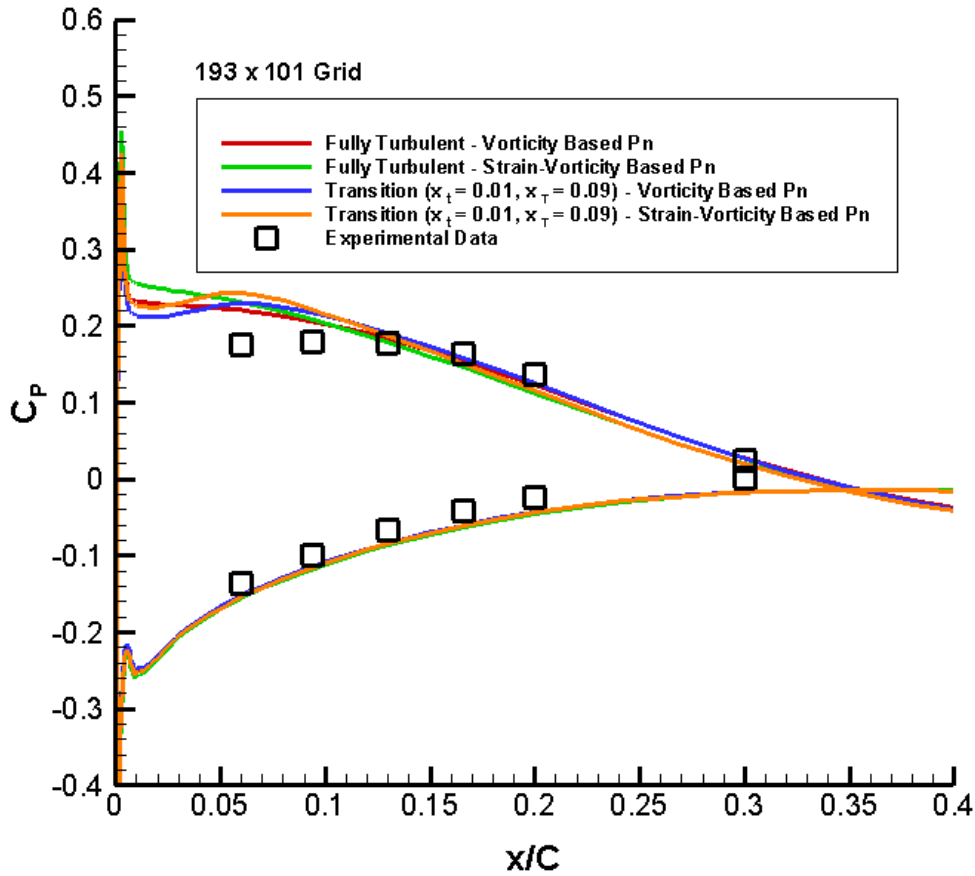


Figure 5.69: Leading edge surface pressure coefficient distribution for the NASA-PW airfoil at the high incidence angle condition for turbulent flow and transitional flow with fixed transition onset using different production term formulations in the SA model

Streamline Curvature Correction Study

In this part of the investigation, the effect due to streamline curvature correction is studied for flow transition over the NASA-PW airfoil at the high incidence angle condition. For this purpose the coarse grid of size 193 x 101 was used. The simulations were carried out by setting the value of inlet turbulent viscosity to 0.009, and vorticity based production formulation was employed in the SA model. The chordwise steady surface pressure distribution is shown in Figure 5.70 where the transition solution

for the fixed transition length model with $x_{LT} = 0.08$ is obtained with streamline curvature correction, and is compared with the transition solution obtained without including the effect of streamline curvature. Also, the fully turbulent solutions are shown to emphasize the effect transitional flow has on the steady pressure distribution. Including the streamline curvature correction, while computing transition, modified the pressure distribution in the leading edge region of the suction surface, and the pressure plateau formed had lower pressure coefficient value than the pressure plateau obtained without including the streamline curvature correction. Moreover, the pressure coefficient for the suction peak also decreased when streamline curvature correction was used with the transition calculation. The leading edge pressure distribution can be seen in Figure 5.71. Including the streamline curvature correction slightly improved the correlation of the transition calculation with the experimental data in the leading edge region.

The variation of the separation and reattachment points with streamline curvature correction is presented in Table 5.6 along with the streamwise distances for the transition onset point, transition termination point, and the transition length. Including the streamline curvature correction resulted in moving the separation and reattachment points downstream along the surface of the airfoil. Moreover, the separation bubble size also increased. Computations without the streamline curvature correction predicted the size of the separation bubble as $0.4416C$ in Cartesian coordinates, and 0.4802 in streamwise coordinates. However, computations with streamline curvature correction predicted the size of the separation bubble as $0.479C$ in Cartesian coordinates, and 0.5219 in the streamwise coordinates. The predicted separation and reattachment points were the same

for the fully turbulent and transitional predictions for the individual cases of with and without streamline curvature correction.

Again, the pressure surface pressure coefficient did not have any noticeable change on account of streamline curvature correction for both the fully turbulent and transition calculations. The transition onset point on the pressure surface was 0.1711C. The transition solutions for the suction surface again blend back into their respective fully turbulent solutions.

Figure 5.72 displays the streamlines in the leading edge region for the high incidence angle case with streamline curvature effects included in the computation of fully turbulent and transitional flows. It can be seen that the streamlines inside the separation bubble form closed loops indicating flow recirculation inside the separated flow region. No major changes in the streamlines occur between the fully turbulent and transitional flow predictions. The pressure surface streamlines indicate that the flow is attached.

Table 5.6: Transitional flow parameters for the NASA-PW airfoil at the high incidence angle condition with and without streamline curvature correction

FCR	Transition Model	x_s	x_r	S_s	S_r	x_t	x_T	x_{LT}
No Correction	None, Fully Turbulent	0.0035	0.4451	0.0093	0.4895	NA	NA	NA
	Fixed	0.0035	0.4451	0.0093	0.4895	0.01	0.09	0.08
Corrected	None, Fully Turbulent	0.0043	0.4833	0.0101	0.5321	NA	NA	NA
	Fixed	0.0043	0.4833	0.0101	0.5320	0.01	0.09	0.08

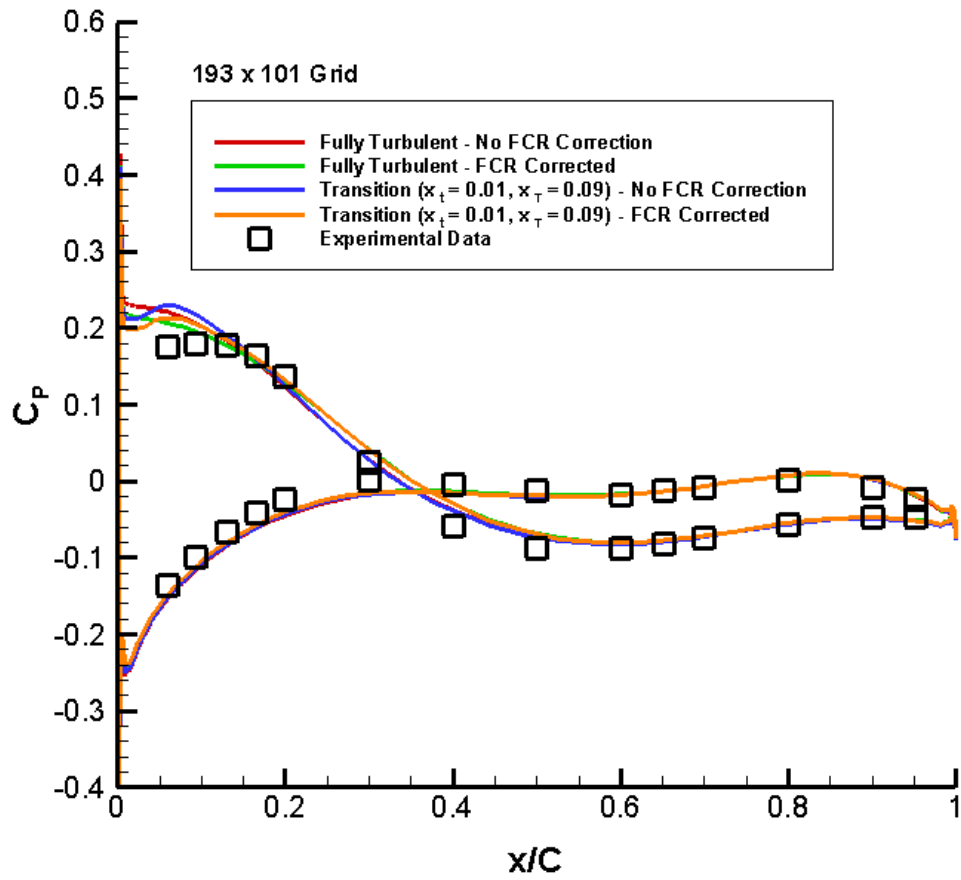


Figure 5.70: Surface pressure coefficient distribution for the NASA-PW airfoil at the high incidence angle condition for turbulent flow and transitional flow with fixed transition onset with and without streamline curvature correction

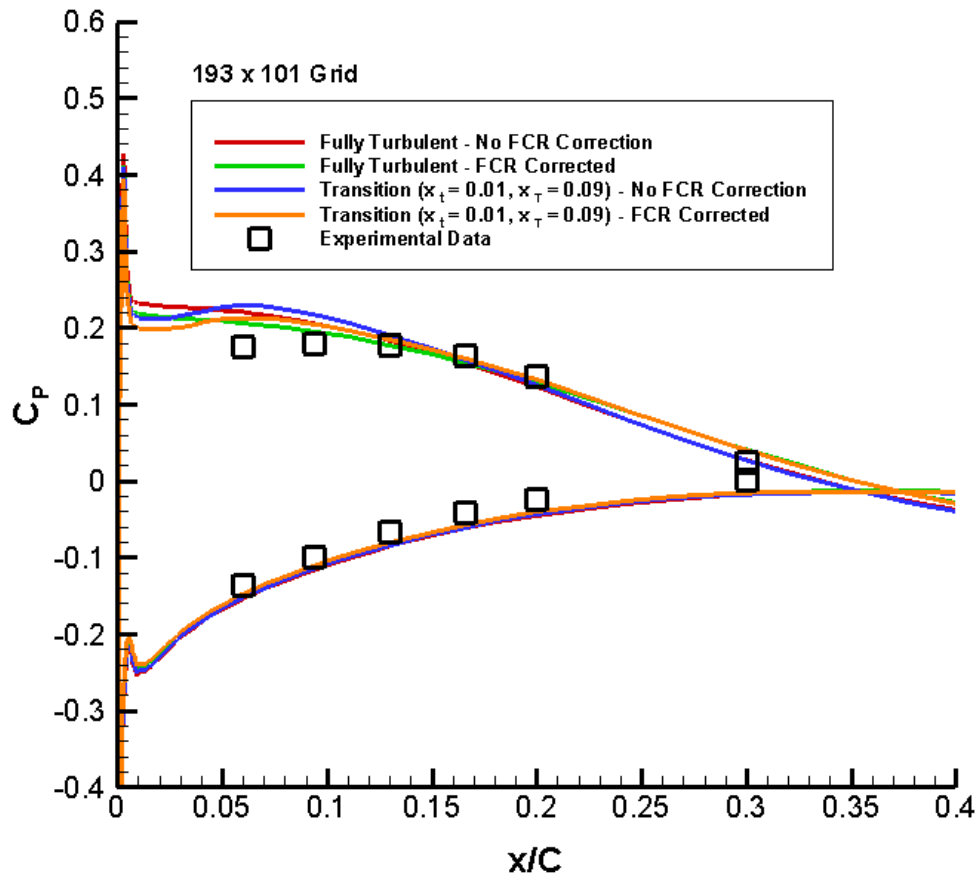
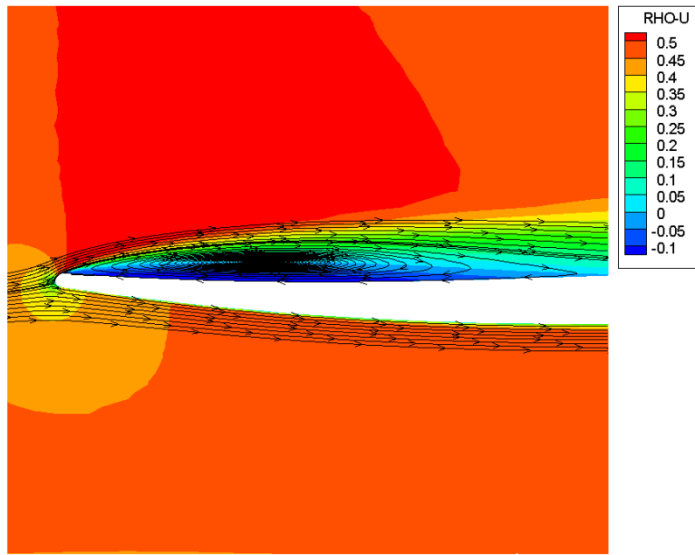
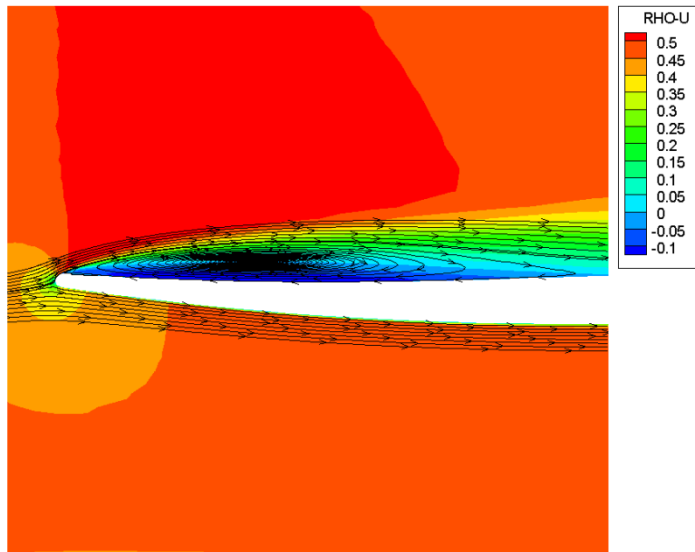


Figure 5.71: Leading edge surface pressure coefficient distribution for the NASA-PW airfoil at the high incidence angle condition for turbulent flow and transitional flow with fixed transition onset with and without streamline curvature correction



(a)



(b)

Figure 5.72: Streamlines in the leading edge region of the NASA-PW airfoil (193 x 101 Grid) at the high incidence angle condition with streamline curvature correction for (a) fully turbulent flow, and (b) transitional flow using fixed transition onset with $x_{LT} = 0.08$

A Study of Inlet Turbulent Viscosity with Streamline Curvature

Correction

In this section, the combined effect of inlet turbulent viscosity and including the streamline curvature correction for computing transition is studied for the high incidence angle case. The coarse grid of size 193 x 101 was utilized, and turbulent viscosity values of 0.009 and 10.0 were used at the inlet boundary. The computations employed the use of the vorticity based production formulation in the SA model. Transition calculations for the fixed transition length model with $x_{LT} = 0.08$ were performed. The computed transition solutions along with the fully turbulent solution and experimental data are presented in Figure 5.73. The transition solution for the inlet turbulent viscosity value of 0.009 was obtained by simply restarting the converged fully turbulent solution that was computed with the inlet turbulent viscosity value of 0.009 with streamline curvature correction activated. For the transition solution with the inlet turbulent viscosity value of 10.0, the converged fully turbulent solution that was computed with the inlet turbulent viscosity value of 0.009, streamline curvature correction activated was restarted and the turbulent viscosity value at the inlet boundary was changed to 10.0 in the computer code. As already seen in the section “Streamline Curvature Correction Study” above, including the effect due to streamline curvature slightly improved the correlation of the computed transition solution with the experimental data in the leading edge region of the suction surface. Also, it was seen in the section “Inlet Turbulent Viscosity Study” above that changing the inlet turbulent viscosity did not have a major influence on the pressure plateau formed inside the separation bubble near the leading edge region. The same effect is again seen in the

pressure distributions shown in the figure. A more detailed view of the leading edge pressure distribution is shown in Figure 5.74. No significant change was observed in the suction peak pressure coefficient for the two values of the inlet turbulent viscosity used in the transition calculations.

The variation of the reattachment location with change in the inlet turbulent viscosity value when streamline curvature correction is also included is presented in Table 5.7 along with the point of flow separation, streamwise transition onset and termination points, and the transition length in streamwise coordinates. Including the effect of streamline curvature while increasing the value of inlet turbulent viscosity to 10.0 resulted in the flow to reattach ahead of the reattachment point predicted by the inlet turbulent viscosity value of 0.009. Moreover, accounting for the streamline curvature correction in the calculations resulted in the separation point moving downstream of that predicted by not accounting for the streamline curvature effects. This has been shown in Table 5.6 above. The net effect of using a higher value of inlet turbulent viscosity with streamline curvature correction is a minor reduction in the predicted size of the separation bubble. In addition, the reattachment point returned to the value originally predicted by not including the streamline curvature correction. Computations with inlet turbulent viscosity value of 0.009 and including streamline curvature correction predicted the size of the separation bubble as 0.479C in Cartesian coordinates, or 0.5219 in streamwise coordinates. However, computations with inlet turbulent viscosity value of 10.0 and including streamline curvature correction predicted the size of the separation bubble as 0.4408C in Cartesian coordinates, or 0.4793 in streamwise coordinates.

There was no change in the results for the pressure surface, neither on account of the streamline curvature correction, nor due to changes in the values of inlet turbulent viscosity. The transition onset point on the pressure surface was specified to be 0.1711C. Moreover, no changes were observed between the fully turbulent and transition solutions for the pressure surface.

Table 5.7: Transitional flow parameters for the NASA-PW airfoil at the high incidence angle condition for different values of inlet turbulent viscosity with streamline curvature correction

FCR	μ_t	Transition Model	x_s	x_r	S_s	S_r	x_t	x_T	x_{LT}
Corrected	0.009	None, Fully Turbulent	0.0043	0.4833	0.0101	0.5321	NA	NA	NA
		Fixed	0.0043	0.4833	0.0101	0.5320	0.01	0.09	0.08
	10.0	Fixed	0.0043	0.4451	0.0101	0.4894	0.01	0.09	0.08

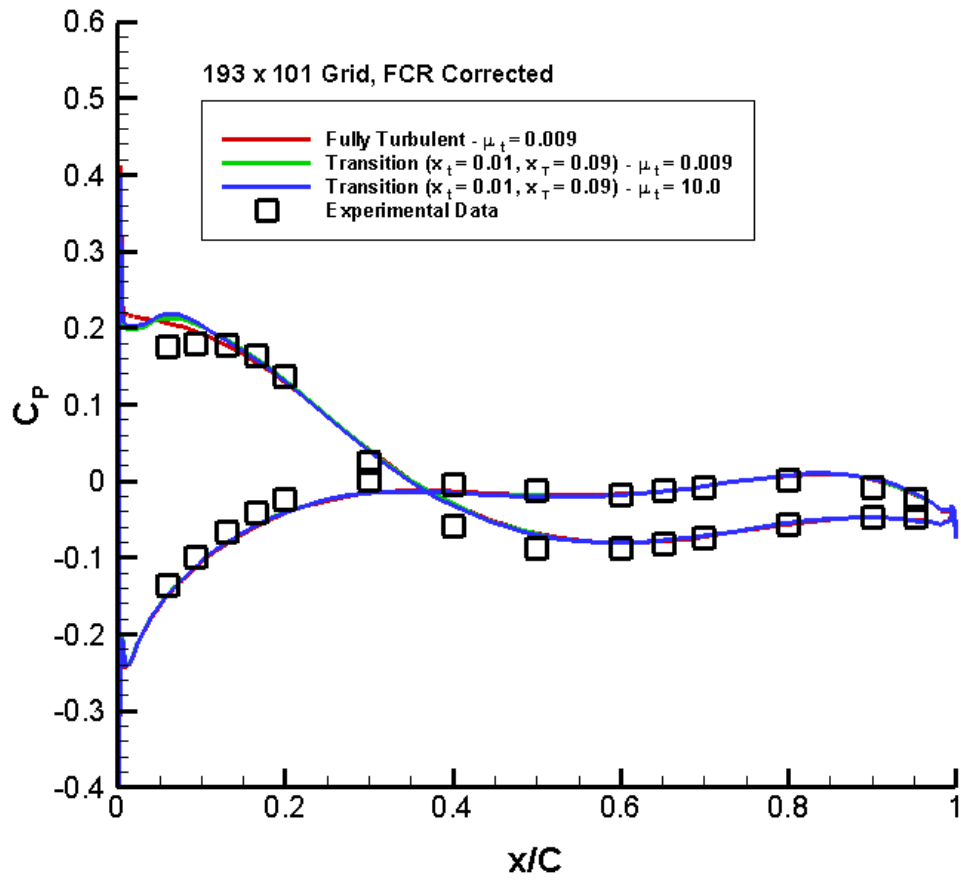


Figure 5.73: Surface pressure coefficient distribution for the NASA-PW airfoil at the high incidence angle condition for turbulent flow and transitional flow with fixed transition onset for different inlet turbulent viscosities with streamline curvature correction

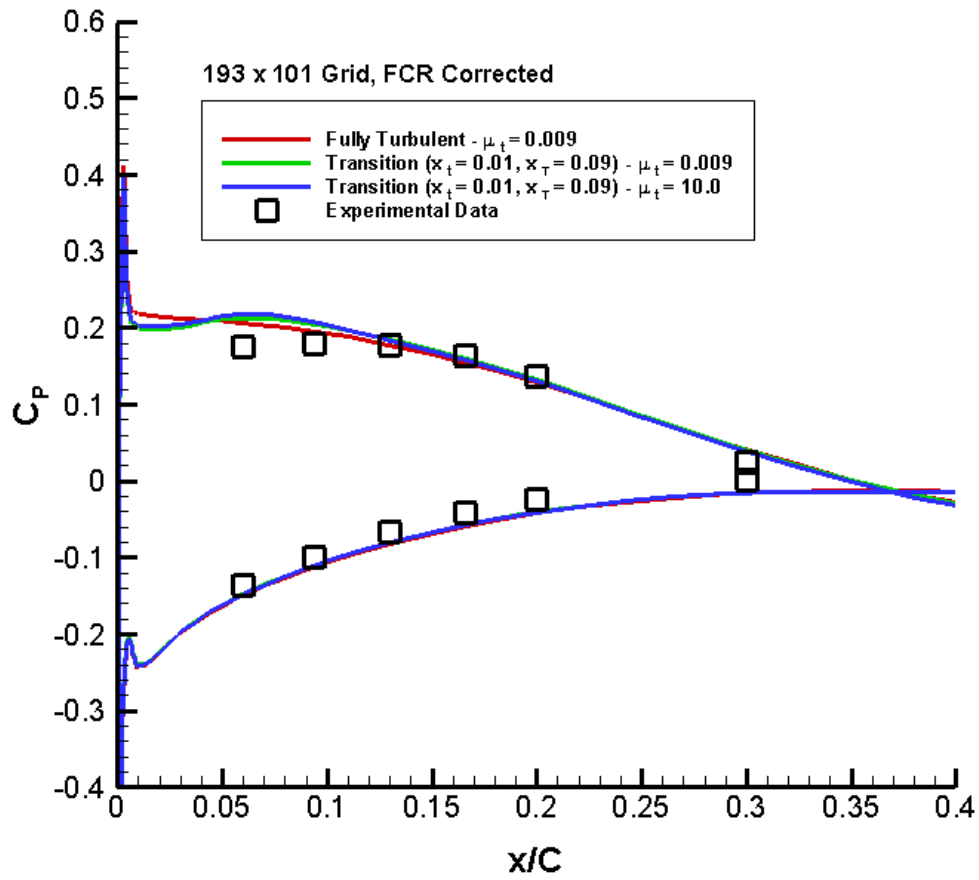


Figure 5.74: Leading edge surface pressure coefficient distribution for the NASA-PW airfoil at the high incidence angle condition for turbulent flow and transitional flow with fixed transition onset for different inlet turbulent viscosities with streamline curvature correction

Chapter Six

Summary and Conclusions

Summary

In this research work, turbulent and transitional flow computations were performed with a two-dimensional Reynolds Averaged Navier-Stokes (RANS) code on a flat plate airfoil, and the NASA-PW Transonic Flutter Cascade (TFC) airfoil. As part of the computations and to ensure completeness, laminar flow calculations were also done for the flat plate airfoil case. The flat plate airfoil is a zero thickness airfoil, and was used to validate the implementation of the numerical scheme. Since the computer code used is a turbomachinery code, the flat plates were modeled as a cascade with zero stagger angle. An inlet Mach number of 0.3 was considered for the incompressible flat plate turbulent boundary layer with zero pressure gradient.

The NASA-PW airfoil has a cross-section similar to that found in the tip region of current low aspect ratio fan blades. A subsonic Mach number of 0.5 at low and high incidence angle conditions was considered. This airfoil has the feature of reverse camber in the leading edge region.

The Spalart-Allmaras (SA) turbulence model was used to compute turbulent flows. The intermittency correlation of the Dhawan and Narasimha (DN) transition model, Mayle's transition length model, plus various fixed transition lengths were used in the transitional flow calculations. The DN transition model was developed for attached boundary layers, whereas the Mayle transition length model was developed for separated flows.

To speed up solution convergence a new approach was taken of starting out the solution process with the Baldwin-Lomax (BL) turbulence model. The solution obtained was then restarted with the SA turbulence model using as initial conditions the turbulent viscosity from the BL model.

Solutions that were independent of the grid density were obtained for both turbulent and transitional flows for the NASA-PW airfoil at the low incidence angle condition. Fully turbulent calculation at the low incidence angle condition using the combination of the BL and SA models showed that the exact same solution can be obtained in a fewer number of time steps compared to using the SA turbulence model throughout the entire solution process. Turbulent and transitional flow solutions that were grid independent were achieved for the high incidence angle condition too. The new approach of using the combination of BL and SA models proved to be successful for the high incidence angle case also.

The SA turbulence model was provided with a new capability to use a user specified turbulent viscosity and an equivalent modified turbulent kinematic viscosity at the inlet boundary. Moreover, the SA model was modified to make use of different production term formulations. In addition, the SA model was sensitized to the effects of streamline curvature. These newly added features were studied for both fully turbulent and transitional flows on the flat plate airfoil and the NASA-PW airfoil.

Conclusions

Laminar flow computations on the flat plate airfoil agreed well with the Blasius solution. Also, the laminar flow predictions have a good correlation with the T3A

experimental data compiled by Savill (1993) in the laminar flow region. The laminar flow solutions failed severely to correlate with the T3A experimental data in the transitional and turbulent flow zones of the flat plate airfoil. The vast difference in the skin-friction coefficient for the laminar and turbulent flow regimes as seen in the T3A data emphasizes the importance of predicting the transition zone.

Excellent agreement was obtained for the turbulent flow predictions over the flat plate airfoil and the experimental data of Wiegardt and Tillmann (1951). As was expected, variations in the inlet turbulent viscosity, different production term formulations in the SA model, and streamline curvature corrections did not have any effect on the turbulent flat plate solutions.

The transitional flow calculations over the flat plate airfoil with the DN transition model successfully predicted the trends seen in the T3A experimental data. The skin-friction coefficient from the computations and the T3A data show that the skin-friction reduces in the streamwise direction in the laminar and turbulent regimes of the flow, and increases in the transitional flow regime. The transition calculations could not accurately capture the flow physics near the onset of transition and the predictions deviated from the experimental data points at the bottom of the bucket. This is in general, due to the failure in predicting the transition onset point accurately, or a failure in the transition modeling of the DN model itself.

The turbulent and transition flow predictions on the flat plate showed that the SA, DN models, and the extended features for the SA model were implemented correctly in the flow solver. Grid independence of the solutions was demonstrated in all of the laminar, turbulent, and transitional flow calculations.

At the low incidence angle condition of the NASA-PW airfoil, the turbulent and transitional flow predictions had good correlation with the experimental data. A small suction surface separation bubble was predicted in the leading edge region. Unfortunately, due to instrumentation limitations, surface pressure data was not available in this area to correlate with the numerical predictions. In the separated flow region, the transition calculations deviated substantially from the turbulent calculation, and a pressure plateau was predicted in this area by the transition calculations.

Mayle's transition length model estimated the transition onset and termination points within the predicted separation bubble. The transition onset and termination points that were selected manually for the fixed transition lengths were also within the separation bubble. The transition onset point predicted by Mayle was farther downstream of the separation point compared to the fixed transition onset point manually selected, and resulted in a longer pressure plateau and a smaller pressure coefficient for the pressure plateau. Transition solutions resulted in an oscillatory flow field for longer transition lengths. As the transition length was increased or as the transition onset point moved farther inside the separation bubble, the length of the pressure plateau increased, and simultaneously the pressure coefficient value decreased for the pressure plateau.

A study of varying the values of inlet turbulent viscosity revealed a change in the turbulent flow predictions inside the separation bubble. The transition calculation with inlet turbulent viscosity of 10.0 predicted the pressure plateau slightly above that of the inlet turbulent viscosity of 0.009. Moreover, the size of the separation bubble reduced when a higher value of 10.0 was used for the inlet turbulent viscosity, but the change in the bubble size was relatively small as compared to the change in the magnitude of the

two inlet turbulent viscosities. Accounting for the streamline curvature also demonstrated that pressure distribution in the separated flow region got altered and the pressure coefficient value dropped near the point of flow separation. Again, this change in the pressure distribution in the separated flow region was relatively small.

For the high incidence angle condition a large suction surface separation bubble was measured. Turbulent flow calculations did not fully capture the pressure plateau in the leading edge region that was exhibited by the experimental data. Transition calculations with the DN transition model showed that with a transition onset point within the bubble a small pressure plateau formed close to the leading edge region. Oscillatory solutions resulted when the transition onset point was too deep within the separation bubble, as was predicted by the Mayle model. Also, longer transition lengths rendered the flow field solution to oscillate. The transition solutions obtained using the DN model predicted pressure plateaus that were smaller in length than the experimental data and had a larger pressure coefficient.

Investigations with production term formulations in the SA model showed that the classical vorticity based production formulation, generally, gave better agreement with the experimental data in the leading edge region of the suction surface, and had a pressure coefficient for the pressure plateau closer to the experimental data than that predicted by the blended strain-vorticity based production formulation. It is recognized that the strain-vorticity formulation is probably more appropriate for vortically intense flows such as in a wing tip vortex for which it was originally proposed in Dacles-Mariani et al. (1995). The size of the separation bubble remained the same for both the production formulations.

Including streamline curvature correction improved the correlation of the transitional flow predictions with the experimental data in the leading edge region. However, the reattachment point predicted was farther downstream when compared to that predicted without streamline curvature correction, and was different than the experimental value. When the turbulent viscosity value at the inlet boundary was varied, interestingly there was no major change in the pressure distribution of turbulent flow or transitional flow, and the predicted size of the separation bubble also remained the same. This was in contrast to what was found for the low incidence angle condition. Combining the streamline curvature correction with a higher value of inlet turbulent viscosity resulted in having better correlation of the computed transition solution with the experimental data in the leading edge region, and the reattachment point again returned back to the value originally predicted when streamline curvature effect was not included in the computation, which was closer to the experimentally determined value. This result was by far the best solution that was obtained in this research work. It is noted that the change in the pressure distribution in the leading edge region of the suction surface with the added features to the SA model were small and did not improve the correlation of the computations with the experimental data by a significant amount.

Overall the DN transition model performed well in determining the trends exhibited in the experimental data for the high incidence angle condition, especially since it was developed for attached flows. No effort was made to change any of the modeling coefficients within the DN model or Mayle's transition length model. However, the ability to select the transition onset point and the transition termination point for the DN model was used to investigate the influence of the onset point and the transition length on

the predicted pressure coefficient. The DN transition model also allows for using a separate empirical model to determine the transition onset point and the transition zone termination point (or length).

Future Work

In general, transition models have been developed using only a limited range of experimental data. More detailed data on the transition process particularly in separation bubbles is necessary to improve transition models. The ability of the DN transition model and other transition models to predict general flow fields particularly at off-design conditions needs to be further investigated to highlight their range of applicability and to help direct future theoretical/numerical and experimental efforts.

Appendix A Turbulent Flat Plate Experimental Data

The incompressible flat plate turbulent boundary layer with zero pressure gradient experimental data of Wieghardt and Tillmann (1951) is tabulated below and was taken from Slater (2008). Skin-friction coefficient values along the surface of the flat plate are presented in Table A.1. The turbulent velocity profile experimental data at the location where the local Reynolds number is 10.3 Million is given in Table A.2.

Table A.1: Variation of the skin-friction coefficient with the local Reynolds number for turbulent flow over the flat plate airfoil

Re_x	C_f	Re_x	C_f
193268	0.005340	4285687	0.002780
411651	0.004240	4998080	0.002690
631400	0.003860	5712235	0.002660
840636	0.003640	6351400	0.002600
1071400	0.003450	7011400	0.002600
1382961	0.003370	7620597	0.002560
1708619	0.003170	8276226	0.002530
2028112	0.003170	8931855	0.002470
2344510	0.003080	9587485	0.002470
2668039	0.003010	10274152	0.002460
3090020	0.002930	10898743	0.002430
3627602	0.002840		

Table A.2: Variation of u^+ with y^+ inside the turbulent boundary layer over a flat plate at the location on the plate where $Re_x = 10.3E6$

y^+	$\log_{10}(y^+)$	u^+
38.4	1.584	14.58
76.8	1.885	15.95
153.7	2.187	17.52
384.2	2.585	19.54
768.3	2.886	21.28
1152.5	3.062	22.45
1536.7	3.187	23.37
1920.8	3.283	24.28
2305.0	3.363	25.11
3073.3	3.488	26.45
3841.7	3.585	27.53
4610.0	3.664	28.24
5378.3	3.731	28.47
6146.7	3.789	28.53

Appendix B

Turbulent Flat Plate Simulations at a Higher Mach Number

The skin-friction variation over the flat plate airfoil is presented below in Figure B.1 for a dense grid of size 418 x 161 at Mach 0.6, chordal Reynolds number of 3 Million using the three different methods to model the production term in the SA model. For these computations the inlet turbulent viscosity was fixed at 0.009, and streamline curvature correction was not used. As was presented above for the low Mach number case, there is no significant difference between the results. The only noticeable minor difference is seen near the leading edge. This is attributed to compressibility effects for the Mach number of 0.6.

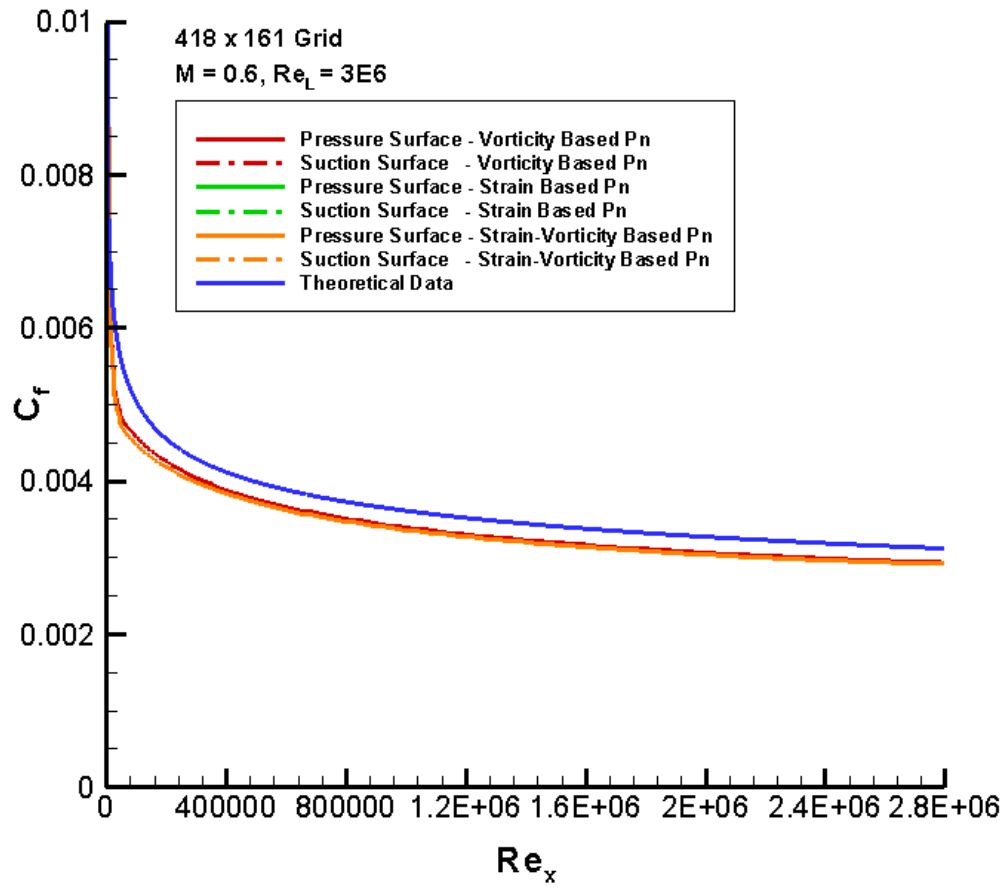


Figure B.1: Flat plate skin-friction coefficient for fully turbulent flow using different production term formulations in the SA model

The corresponding $u^+ - y^+$ variation for the dense grid of size 418 x 161 at Mach 0.6, chordal Reynolds number of 3 Million is shown in Figure B.2 for the three different methods used to model the production term in the SA model. Again, as seen above for the low Mach number case there was no significant difference between the results, and all the three methods follow each other closely.

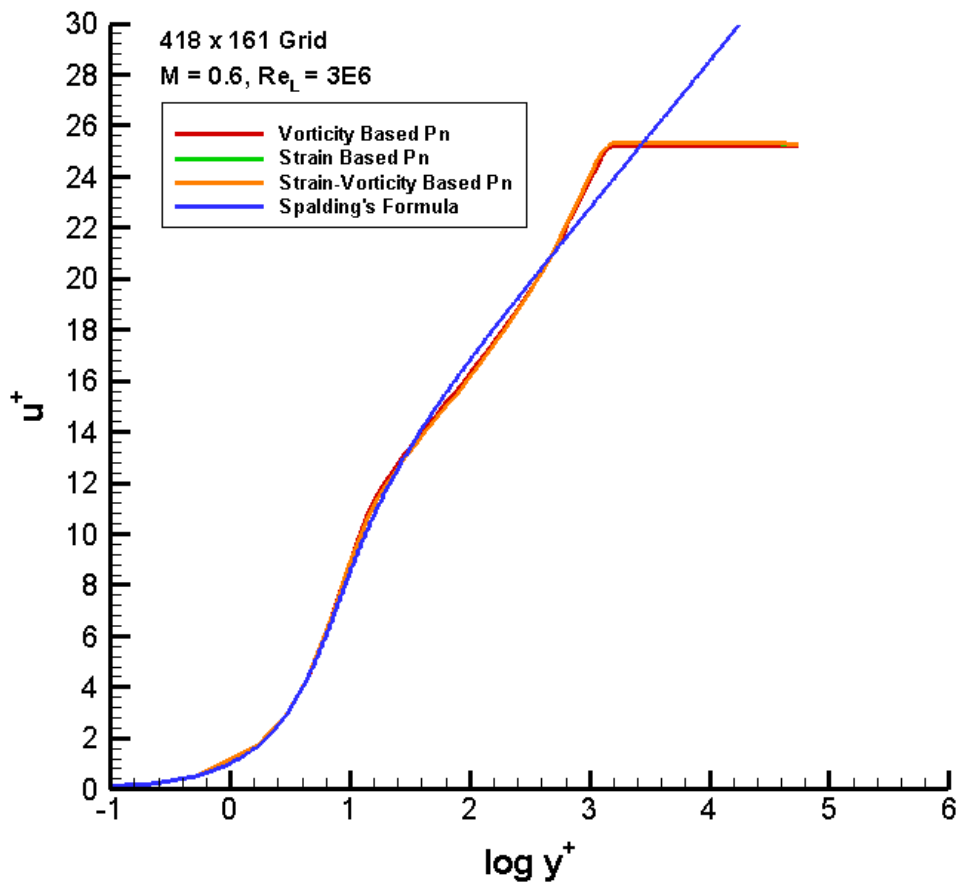


Figure B.2: Flat plate velocity distribution for fully turbulent flow using different production term formulations in the SA model

REFERENCES

- Ayer, T.C., and Verdon, J.M., 1994, "Numerical Unsteady Aerodynamic Simulation for Blade Forced Response," Report WL-TR-95-2011.
- Baldwin, B.S., and Lomax, H., 1978, "Thin Layer Approximation and Algebraic Model for Separated Turbulent Flows," AIAA Paper No. 78-257.
- Baldwin-Lomax model, 12 June 2007, Retrieved from the CFD-Wiki: http://www.cfd-online.com/Wiki/Baldwin-Lomax_model.
- Blasius, H., 1908, Z. Angew. Math. Phys., Vol. 56, pp. 1-37 (Engl. trans., NACA Tech. Mem. 1256) – taken from White (1974).
- Buffum, D.H., Capece, V.R., King, A.J., and El-Aini, Y.M., 1998, "Oscillating Cascade Aerodynamics at Large Mean Incidence," ASME Journal of Turbomachinery, Vol. 120, No. 1, pp. 122-131; also NASA TM-107247.
- CFL3D User's Manual, Version 5.0, Second Edition, 1997; also NASA TM-1998-208444, 1998.
- Chen, K.K., and Thyson, N.A., 1971, "Extension of Emmons' Spot Theory to Flows on Blunt Bodies," AIAA Journal, Vol. 18, No. 3, pp. 490-498.
- Chima, R.V., Giel, P.W., and Boyle, R.J., 1993, "An Algebraic Turbulence Model for Three-Dimensional Viscous Flows," NASA TM-105931.
- Cho, J.R., and Chung, M.K., 1992, "A $k-\varepsilon-\gamma$ Equation Turbulence Model," J. Fluid Mech., 237, pp. 301-322.
- Coles, D.E., and Hirst, E.A., 1968, "Computation of Turbulent Boundary Layers-1968," AFOSR-IFP-Stanford Conference, Vol. II, Thermosciences Div., Mech. Engg. Dept., Stanford University, CA.
- Dacles-Mariani, J., Zilliac, G.G., Chow, J.S., and Bradshaw, P., 1995, "Numerical/Experimental Study of a Wingtip Vortex in the Near Field," AIAA Journal, Vol. 33, No. 9, pp. 1561-1568.
- Dhawan, S., and Narasimha, R., 1958, "Some Properties of Boundary Layer Flow during Transition from Laminar to Turbulent Motion," Journal of Fluids Engineering, Vol. 3, pp. 418-436.
- Ekaterinaris, J.A., Chandrasekhara, M.S., and Platzler, M.F., 1995, "Analysis of Low Reynolds Number Airfoil Flows," Journal of Aircraft, Vol. 32, No. 3, pp. 625-630.
- Emmons, H.W., 1951, "The Laminar-Turbulent Transition in a Boundary Layer – Part I," J. Aero. Sci., 18, pp. 490-498.
- Granville, P.S., 1990, "A Near-Wall Eddy Viscosity Formula for Turbulent Boundary Layers in Pressure Gradients Suitable for Momentum, Heat, or Mass Transfer," ASME Journal of Fluids Engineering, Vol. 112, June, pp. 240-243.
- Hellsten, A., 1998, "Some Improvements in Menter's $k-\omega$ SST Turbulence Model," AIAA Paper No. 98-2554.

Langtry, R.B., and Sjolander, S.A., 2002, "Prediction of Transition for Attached and Separated Shear Layers in Turbomachinery," AIAA Paper No. 2002-3641.

Mayle, R.E., 1991, "The Role of Laminar-Turbulent Transition in Gas Turbine Engines," ASME Journal of Turbomachinery, Vol. 113, pp. 509-537.

Menter, F.R., Esch, T., and Kubacki, S., 2002, "Transition Modeling Based on Local Variables," Engineering Turbulence Modeling and Experiments, W. Rodi, and N. Fueyo (Editors), Elsevier Science Ltd.

Menter, F.R., Langtry, R.B., Likki, S.R., Suzen, Y.B., Huang, P.G., and Voelker, S., 2006, "A Correlation-Based Transition Model Using Local Variables," ASME Journal of Turbomachinery, Vol. 128, July, pp. 413-434.

Michel, R., 1951, "Etude de la transition sur les profils d'aile; establishment d'un critere de determination de point de transition et calcul de la trainee de profile incompressible," ONERA Rep. 1/1578A.

Narasimha, R., 1985, "The Laminar-Turbulent Transition Zone in the Boundary Layer," Prog. Aerospace Sci., Vol. 22, pp. 29-80.

Praisner, T., and Clark, J., 2004, "Predicting Transition in Turbomachinery. Part I: A Review and New Model Development," ASME Paper No. IGTI-2004-54108.

Sanz, W., and Platzer, M.F., 1998, "On the Navier-Stokes Calculations of Separation Bubbles with a New Transition Model," ASME Journal of Turbomachinery, Vol. 120, pp. 36-42.

Sanz, W., and Platzer, M.F., 2002, "On the Numerical Difficulties in Calculating Laminar Separation Bubbles," ASME Paper No. GT-2002-30235.

Savill, A.M., 1993, "Some Recent Progress in the Turbulence Modeling of By-pass Transition," In: R.M.C. So, C.G. Speziale, and B.E. Launder (Editors), Near-Wall Turbulent Flows, Elsevier Science Publishers, pp. 829-848.

Slater, J.W., 2008, "NPARC Alliance CFD Verification and Validation," NASA Glenn Research Center, <http://www.grc.nasa.gov/WWW/wind/valid/fpturb/fpturb.html>.

Solomon, W.J., Walker, G.J., and Gostelow, J.P., 1996, "Transition Length Prediction for Flows with Rapidly Changing Pressure Gradients," ASME Journal of Turbomachinery, Vol. 118, pp. 744-751.

Spalart, P.R., and Allmaras, S.R., 1994, "A One Equation Turbulence Model for Aerodynamic Flows," La Recherche Aerospaciale, No. 1, pp. 5-21.

Spalding, D.B., 1961, "A Single Formula for the Law of the Wall," J. Appl. Mech., Vol. 28, pp. 455-457 – taken from White (1974).

Steelant, J., and Dick, E., 1996, "Modeling of Bypass Transition with Conditioned Navier-Stokes Equations Coupled to an Intermittency Transport Equation," Int. J. Numer. Methods Fluids, 23, pp. 193-220.

Steelant, J., and Dick, E., 2001, "Modeling of Laminar Turbulent Transition for High Free-Stream Turbulence," Journal of Fluids Engineering, Vol. 123, pp. 22-30.

Suzen, Y.B., Huang, P.G., Hultgren, L.S., and Ashpis, D.E., 2003, "Predictions of Separated and Transitional Boundary Layers Under Low-Pressure Turbine Airfoil Conditions Using an Intermittency Transport Equation," *Journal of Turbomachinery*, Vol. 125, No. 3, pp. 455-464.

Swafford, T.W., Loe, D.H., Huff, D.L., Huddleston, D.H., and Reddy, T.S.R., 1994, "The Evolution of NPHASE: Euler/Navier-Stokes Computations of Unsteady Two-Dimensional Cascade Flow Fields," AIAA Paper No. AIAA-94-1834.

Tennekes, H., and Lumley, J.L., 1972, "A First Course in Turbulence," The MIT Press.

Van Driest, E.R., and Blumer, C.B., 1963, "Boundary Layer Transition: Freestream Turbulence and Pressure Gradient Effects," *AIAA Journal*, Vol. 1, No. 6, pp. 1303-1306.

van Dyken, R.D., Ekaterinaris, J.A., Chandrasekhara, M.S., and Platzer, M.F., 1996, "Analysis of Compressible Light Dynamic Stall Flow at Transitional Reynolds Numbers," *AIAA Journal*, Vol. 34, No. 7, pp. 1420-1427.

White, F.M., 1974, "Viscous Fluid Flow," McGraw-Hill, Inc.

Whitlow, D., Capece, V.R., Jones, K.D., Platzer, M.F., 2006, "Navier-Stokes Computations of the Flow through the NASA GRC Transonic Flutter Cascade," AIAA Paper No. 2006-4455.

Wieghardt, K., and Tillmann, W., 1951, "On the Turbulent Friction Layer for Rising Pressure," NACA TM-1314.

Wilcox, D.C., 1994, "Turbulence Modeling for CFD," Second Edition, DCW Industries, Inc.

Wong, H.Y., 1999, "One-Equation Turbulence Model of Spalart and Allmaras in Supersonic Separated Flows," *AIAA Journal*, Vol. 37, No. 3, pp. 391-393.

Yaras, M.I., and Grosvenor, A.D., 2003, "Evaluation of One- and Two-Equation Low-Re Turbulence Models. Part I – Axisymmetric Separating and Swirling Flows," *International Journal for Numerical Methods in Fluids*, Vol. 42, No. 12, pp. 1293-1319.

VITA

Date and Place of Birth

18th May 1983, New Delhi, India

Educational Institutions Attended and Degrees Awarded

1. Bachelor of Engineering, Mechanical Engineering, 2001 – 2005
Anna University, Chennai, India
S.R.M. Engineering College, Chennai, India

Professional Positions Held

1. Tata Chemicals Limited, Mithapur, Gujarat, India, Jul 2005 – Jul 2007
Assistant Manager – Power Plant

Scholastic and Professional Honors

1. Research Assistant (Mechanical Engg. Dept., University of Kentucky)
2. Graduate Certificate in Computational Fluid Dynamics

Professional Publications

1. Zhang, Q., Hariharan, V., and Capece, V.R., 2008, “Computational Investigation of a Transonic Flutter Cascade,” AIAA Paper No. AIAA-2008-4701.
2. Hariharan, V., and Capece, V.R., 2008, “Computation of Separated Flow Transition of a Compressor Airfoil,” Abstract, 33rd Annual Dayton-Cincinnati Aerospace Science Symposium, Dayton, OH.

Vivek Hariharan